Multiphase Flow Dynamics: Insights from Single Microchannels to Porous Media with Uniform and Hierarchical Microchannel Networks

Yang, Shuo

2024

Document Version:
Publisher's PDF, also known as Version of record

Link to publication

Citation for published version (APA):
Yang, S. (2024). *Multiphase Flow Dynamics: Insights from Single Microchannels to Porous Media with Uniform and Hierarchical Microchannel Networks*. Institutionen för Energivetenskaper Lunds Universitet - Lunds Tekniska Högskola.

Total number of authors:
1

Multiphase Flow Dynamics: Insights from Single Microchannels to Porous Media with Uniform and Hierarchical Microchannel Networks

SHUO YANG
DEPARTMENT OF ENERGY SCIENCES | FACULTY OF ENGINEERING | LUND UNIVERSITY

Multiphase Flow Dynamics: Insights from Single Microchannels to Porous Media with Uniform and Hierarchical Microchannel Networks

Multiphase Flow Dynamics: Insights from Single Microchannels to Porous Media with Uniform and Hierarchical Microchannel Networks

Shuo Yang

LUNDS UNIVERSITET
Lunds Tekniska Högskola

DOCTORAL DISSERTATION

With permission of the Faculty of Engineering (LTH), Lund University, Sweden. To be defended on Wednesday 11 September 2024, at 09:00 AM in Lecture Hall M:B in the M-huset, Ole Römers väg 1, Lund, Sweden.

Thesis supervisor: Professor Johan Revstedt, Dr. Lei Wang

Faculty opponent:

Professor Carl Fredrik Berg,

Department of Geoscience and Petroleum,

Norwegian University of Science and Technology (NTNU), Trondheim, Norway.

Organization LUND UNIVERSITY	Document name DOCTORAL DISSERTATION
Department of Energy Sciences	Date of issue September 11, 2024
Author(s) Shuo Yang	Sponsoring organization China Scholarship Council

Title and subtitle

Multiphase Flow Dynamics: Insights from Single Microchannels to Porous Media with Uniform and Hierarchical Microchannel Networks

Abstract

In this thesis, a microfluidics platform with high-speed imaging system was built to investigate gas-liquid flow in single microchannel as a simple model and interfacial instability in porous media with microchannel network: The mass transfer of slug flow in the rectangular and square microchannels was experimentally studied. By using digital image processing, the bubble volume especially that of deformed bubbles was calculated based on 2D projection and 3D slicing. Mass transfer coefficients were calculated based on bubble volume. To be universality, a semi-theoretical model considering length ratio of liquid and gas phases was developed to predict measured mass transfer coefficients in square microchannel precisely.

Next, I began to switch my perspective from single microchannel to porous media with microchannel networks. In the first step, the gas-liquid displacement in porous media after breakthrough was investigated. Fingering dynamical behaviors in different flow pattern was investigated. Time evolution of fingering displacement demonstrated an unobserved circle, consisting of new finger generation, cap invasion, breakthrough and finger disappearance. The circle repeats until steady state.

Then, I expanded the two-phase displacement to viscous-dependent three-phase displacement. By varying gas (G) invasion scenarios of a high viscous defending liquid (HL), low viscous liquid (LL), and their co-existing multi-fluid system, the influence of fluid viscosity was investigated. A novel yarn-like gas pattern was observed during G→(LL→HL) displacement, in which gas invading speech is ultra-fast.

Finally, I further extend our research to cyclic gas-liquid invasion. To model the actual underground porous structure, a hierarchical porous media featuring multiple-level of pore sizes was designed and fabricated by 3D printing. The impact of hierarchical structure on gas-liquid cyclic injection was investigated. The Land model confirms that the saturation hysteresis effect is weaker in hierarchical structures compared to uniform structures. The discoveries in this thesis contribute to an improved comprehension of the interaction dynamics of multiphase flow at the microscale, particularly concerning the optimization of strategies for subsurface resource storage and extraction applications.

Key words:

mass transfer, bubble flow, porous media, invading dynamics, hierarchical structure, underground gas storage

Classification system and/or index terms (if any)

Supplementary bibliographical information		Language English
ISSN and key title ISSN 0282-1990 ISRN LUTMDN/TMHP-24/1176		ISBN 978-91-8104-096-8 (print) 978-91-8104-097-5 (electronic)
Recipient's notes	Number of pages 93	Price
	Security classification	

Signature Date July 15, 2024

Multiphase Flow Dynamics: Insights from Single Microchannels to Porous Media with Uniform and Hierarchical Microchannel Networks

Shuo Yang

LUNDS UNIVERSITET
Lunds Tekniska Högskola

Department of Energy Sciences

Faculty of Engineering (LTH)

Lund University, Lund, Sweden

www.energy.lth.se

Thesis for the degree of Doctor of Philosophy in Engineering.

Division of Heat Transfer
Department of Energy Sciences
Faculty of Engineering (LTH)
Lund University
Box 118
SE-221 00 LUND
SWEDEN

978-91-8104-096-8 (print)
978-91-8104-097-5 (electronic)
ISRN LUTMDN/TMHP-24/1176
ISSN 0282-1990

Printed in Sweden by Media-Tryck, Lund University
Lund 2024

Popular Science

Porous media, as solid objects with interconnected pores, are prevalent in our lives and in nature, such as soils and geological sedimentary rocks. In particular, a large amount of pore space exists between underground rock fractures. It was found that the porous space underground could be used to store carbon dioxide and hydrogen, which can solve the problems of greenhouse effect and hydrogen energy storage, respectively. However, multiphase transport in porous media is complex such as mass transfer from gas phase to liquid phase due to dissolution of carbon dioxide and the gas-liquid interface becomes unstable due to the action of various forces. They have an important influence on storage/extraction effectiveness and leakage risk. Therefore, it is essential to reveal the pore-scale mechanism of multiphase displacement in porous media.

In the first part, since the porous medium can be considered as a network of microchannels, the study starts with the single straight microchannels as a simple model. Dynamics and mass transfer of gas-liquid flow in single straight microchannels were studied. A microfluidics platform was built to study the gas-liquid flow in single straight rectangular and square microchannels by using water as liquid phase and N_2 and CO_2 as gas phase. Flow pattern was captured by a high-speed imaging system and the recorded images were processed by digital image technology. Bubble volume especially that of deformed bubbles was measured by 2D projection and 3D slicing methods. The relationships between various important parameters in microreactor application were built to provide the guidance of microchannel design. Based on bubble volume, mass transfer coefficient was calculated. The effect of flow rate on mass transfer was investigated. Empirical correlations and semi-theoretical model were derived to predict mass transfer coefficient. These predicting models can be used to optimize the performance of microreactor.

In the second part, the insight was shifted back to the multiphase displacement in porous media. First, gas-liquid two-phase displacement was investigated in porous media. Visualization of fingering morphology shows that capillary fingering stops displacing after breakthrough, whereas viscous fingering can continue until almost all the liquid phase is displaced. Important quantitative studies were carried out using digital image processing to analyze invading velocity, invaded area and finger complexity. It was observed that the displaced area was significantly enlarged after breakthrough of the viscous fingering area. After breakthrough, a previously unobserved invading cycle was discovered, involving new finger generation, cap invading, breakthrough and finger vanishing. This process will repeat until steady state.

Then the research was expanded to viscous-dependent three-phase displacement, where gas invasion into a high viscous liquid, low viscous liquid, and their co-existing multi-fluid system. The result shows that displacement efficiency in three-phase displacement is improved compared with two-phase displacement. The enhancement in displacement

efficiency leads to energy savings, which are attained exclusively through the introduction of a third phase, without incurring the expenses associated with increased pumping power. For the first time, the previously unobserved yarn-like gas invading pattern was reported and two distinct categories of residue gas movement and connection were discovered. These discoveries significantly enhance the innovation of subsurface gas storage strategies by enriching multi-fluids injection scenarios.

Last, a heterogeneous porous media with hierarchical structure was designed to closely mirror the actual underground structure compared to homogeneous porous media. This hierarchical porous media with multiple levels of pore sizes was fabricated by 3D printing. Hysteresis during gas-liquid cyclic injection was investigated, and it was found that the hierarchical structure could suppress the hysteresis effect in the cyclic injection process. Through the analysis of local invasion behavior, the unique invasion method in hierarchical structure is considered as the key factor behind this suppression. Finally, the topology connectivity and permeability were quantified to further investigate the influence of hierarchical structure. These findings provide valuable insights that can improve the efficiency of underground hydrogen storage and extraction applications.

Abstract

Multiphase flow in porous media are widespread in emerging subsurface application including geological carbon sequestration and underground hydrogen storage. Multiple fluid interactions introduce more complexity compared to single phase flow. On the gas-liquid interface, mass transfer and interfacial instability may arise. The study of multi-phase interaction behaviour allows the insights gained to be applied to underground storage and recovery applications. In this thesis, a microfluidics platform with high-speed imaging system was built to investigate gas-liquid flow in single microchannel as a simple model and interfacial instability in porous media with microchannel network:

At the beginning, to simply the model, mass transfer of deformed bubble flow in the single rectangular and square microchannels was experimentally studied by using water as liquid phase and CO_2 as gas phase. Depending on flow rates, flow patterns including slug flow, bubbly flow, and annular flow were observed in rectangular and square microchannels. Flow pattern map was proposed and compared with the maps in the literatures. By using digital image processing, the bubble volume especially that of deformed bubbles in rectangular and square microchannels was calculated based on 2D projection and 3D slicing, correspondingly. Scaling laws including important parameters of bubbles were derived to provide the guidance of microreactor design. Mass transfer coefficients were calculated based on bubble volume. The empirical correlations involving dimensionless numbers were fitted to precisely predict mass transfer coefficients. Further, to be universality, a semi-theoretical model considering length ratio of liquid and gas phases was developed to predict measured mass transfer coefficients in square microchannel precisely.

Next, I began to switch our perspective from single microchannel to porous media with microchannel networks. In the first step, the gas-liquid two-phase displacement in porous media with microchannel network was first investigated. By varying capillary numbers Ca and viscosity ratios M in a wide range, flow pattern involving viscous fingering (VF), capillary fingering (CF) and crossover zone (CZ) can be observed. Finger morphologies at breakthrough moment and steady state in three different flow regions was visualized. The main difference between VF and CF is that the gas stops invading in CF region after breakthrough, whereas in VF region gas can continue to expand until almost all the liquid phase is displaced. Invasion velocity, phase saturation and fingering complexity were quantified based on digital image processing. Fingering dynamical behaviors in different flow pattern before and after breakthrough was investigated. Time evolution of fingering displacement after breakthrough demonstrated an unobserved circle, consisting of new finger generation, cap invasion, breakthrough and finger disappearance. The circle repeats until steady state. Finally, local dynamical invasion behavior was studied and a stepwise way of gas invasion was exposed.

In numerous geological gas storage procedures, the injected gas infiltrates aquifers containing multiple fluids, such as depleted oil reservoirs nearing the completion of extraction following water or brine flooding. Therefore, in the next step, I expanded the two-phase displacement to viscous-dependent three-phase displacement. By varying gas (G) invasion scenarios of a high viscous defending liquid (HL), low viscous liquid (LL), and their co-existing multi-fluid system, the influence of fluid viscosity was investigated. The residual saturation of the initial phase suggests that the displacement efficiency follows the order G→(L→L) > L→L > G→L, regardless of the injection flow rate. The introduction of a third gas phase improves the displacement efficiency and potential energy savings without incurring higher pumping power costs. The finger patterns of gas invasion in G→(LL→HL) and G→(HL→LL) displacement are very sensitive to the order of occupation of HL and LL within the pore space. Notably, a novel yarn-like gas pattern was observed during G→(LL→HL) displacement, in which gas invading speech is ultra-fast. Analysis of the local invasive behaviour revealed the main mechanism for the formation of yarn-like fingers, i.e., the tendency of gas to invade the interconnected LL channels, whereas the dispersed HL prevented the bypass expansion of the gas. Two types of ganglia movement and connection in G→(LL→HL) displacement were discovered, i.e. ¨catch up to connect¨ and ¨expand to connect¨. Finally, the time evolution of finger topological connectivity confirms that disconnected ganglia that appear before the breakthrough will expand and reconnect again after breakthrough.

In the finally step, I further extend our research to cyclic gas-liquid invasion. To model the actual underground porous structure, a hierarchical porous media featuring multiple-level of pore sizes was designed and fabricated by 3D printing. The impact of hierarchical structure on invasion behavior was investigated during gas-liquid cyclic injection in uniform and hierarchical structures. By analyzing fingering morphology and quantifying phase saturation at each order structure, it was found that gas prefers to invade in the 1st-order structure and is trapped by capillary force in the 2nd-order structure. Then, connectivity and permeability were quantified by using the Euler number and Lattice Boltzmann method (LBM), respectively. Compared to uniform structure, the hierarchical structure exhibits higher connectivity and relative permeability. The hysteresis effect occurs during gas-liquid cycle invasion. The Land model confirms that the saturation hysteresis effect is weaker in hierarchical structures compared to uniform structures. To investigate the underlying cause, I examined ganglia mobilization behavior and analyzed local invasion behavior. In contrast to homogeneous structures, ganglion movement is limited in hierarchical structures. I found the connection-jumping invasion method is the main mechanism behind this suppression.

The discoveries in this thesis contribute to an improved comprehension of the interaction dynamics of multiphase flow at the microscale, particularly concerning the optimization of strategies for subsurface resource storage and extraction applications.

Keywords: mass transfer, bubble flow, porous media, invading dynamics, hierarchical structure, underground gas storage

Acknowledgments

Time flies. I'm almost at the end of my PhD study, a tough journey always with confusion and frustration. I hate it but enjoy and appreciate it. Firstly, I appreciate myself to have the courage to come to Sweden, far away from home, to start the PhD study. I still remember the rainy night when I got off the train in Lund C with two big suitcases. I started this journey with anticipation. PhD research was not always smooth. I often experienced setbacks and felt like giving up. Thanks to many people who helped and inspired me. I would like to express my gratitude to all of you.

First and foremost, I want to send my deepest gratitude and respect to my supervisor, Professor Johan Revstedt and former supervisor, Professor Zan Wu. Thank you, Zan, for taking the role as the supervisor for the first year and for leading me into the PhD journey and teaching me how to do scientific research. Your wisdom and attitude toward study have been inspiring me. Thank you, Johan, for taking over the responsibility of supervisor and providing guidance for my research, especially assisting me in finishing the licentiate defense step by step. You always provided effective advice and encouraged me whenever I needed help. Apart from the work, you both cared about my life kindly. Without you, I would not be able to carry out my PhD project smoothly. I appreciate having both of your guidance over the past three years. I will carry your expectations forward after graduation. Thank you very much again.

Thank you, my co-supervisors, Lei Wang and Zhen Cao. Thank you, Lei, for the useful suggestion for my research, especially the design of micromodel holder. Thank you, Zhen, also my close friend. You always gave me a hand in my life. In terms of experiments, you often suggested effective solutions and answered my questions patiently. I enjoy doing experiment with you in M-huset and working in our office of Kemicentrum building.

Especially, I would like to appreciate my former colleague, Gaopan Kong. You led me to build the microfluidics platform and develop the experimental method at the beginning of PhD. Thank you for your recommendation for an academic visit to the University of Cambridge. In addition, I would like to thank Hongxia Li who offered me a lot of help in the field of porous media. Your intelligence and work attitude are worth learning for me. Also, thank you, Professor Shervin Bagheri and Dr. Si Suo, for the collaborating project on hierarchical porous media. Thank Shervin for being my licentiate opponent and providing the 3D printing resource in KTH. Finally, I would like to express my gratitude to Wei Qiu for invaluable theoretical guidance and access to advanced experimental equipment in Department of Biomedical Engineering for our collaborative project on acoustofluidics.

I want to post a big **Thank you** to all my nice colleagues in the department, Danan, Yuxiang, Zhan, Yucheng, Yong, Hongwei, Arvid, Gustav, Himani, Thommie, Alessandro, Francesco, Anupam, Guillaume, Xiaoqiang, Miao, Bora, Björn, Jan-peter, Marcus, Pierre, Diamantis, Rasmus, Miaoxin… all of you. Thank you for the interesting discussion in the lunchroom and the parties afterwork. I enjoy every moment of working with all of you.

Special thanks to my office mate Danan for discussing Matlab code with me in terms of work and treating each other like brothers in terms of life.

I would like to thank the technicians, Anders Olsson in my department and Axel Tojo in BME, for processing of experimental components. I also want to thank the administrative staffs, Catarina Lindén, Andrea Frydenlund and Isabelle Frej. Thanks for the help with student registration, course registration, expense reimbursement and arrangements for defense.

For financial support, I would like to appreciate the China Scholarship Council (CSC) which granted me the PhD scholarship for my living and accommodation in Sweden, and the Royal Physiographic Society of Lund and ÅForsk which supported me to attend the conferences.

Last but not least, I would like to thank my family, the most important people in my life: My father 杨经超, my mother 吴莹, my sister 杨海冰, my uncle 吴小锐. I really appreciate your care and support in my life. Every time I feel like giving up, your encouragement keeps me going. Thanks to your selfless love and support, I can feel free to explore the world and pursue my dream.

List of Publications

Publications included in the thesis:

i. **Shuo Yang**, Gaopan Kong, Zan Wu*, Experimental study of gas-Liquid Mass transfer in a rectangular microchannel by digital image analysis method. *ASME International Mechanical Engineering Congress and Exposition*, 2021, Nov 1 (Vol. 85666, p. V010T10A040).

ii. **Shuo Yang**, Gaopan Kong, Zhen Cao, Zan Wu*, Mass transfer and modeling of deformed bubbles in square microchannel. *Chemical Engineering Journal Advances*, 2023, 16: 100518.

iii. **Shuo Yang**, Gaopan Kong, Zhen Cao, Zan Wu*, Hongxia Li**, Hydrodynamics of gas-liquid displacement in porous media: fingering pattern evolution at the breakthrough moment and the steady state. *Advances in Water Resources*, 2022, 170: 104324.

iv. **Shuo Yang**, Hongxia Li*, Si Suo, Zan Wu**, Viscous-dependent fingering dynamics of gas invading into multi-fluids**.** *Advances in Water Resources*, 2024, 191: 104757.

v. **Shuo Yang***, Si Suo, Yixiang Gan, Lei Wang, Shervin Bagheri, Johan Revstedt, Experimental study on hysteresis during cyclic injection in hierarchical porous media. *Water Resources Research*, under review.

Publications not included in the thesis:

i. Hongxia Li*, Jiabao Li, **Shuo Yang**, Chengyao Wang, Zan Wu**, Microscopic insights of phase-transition-induced vapor transport enhancement in porous media. *International Journal of Multiphase Flow*, 2024, 177: 104855.

ii. Kunman Yao, Mou Xu, **Shuo Yang**, Xizhe Huang, Dongchuan Mo*, Shushen Lyu, Pool boiling heat transfer characteristics of porous nickel microstructure surfaces. *Journal of Enhanced Heat Transfer*, 2024, Vol. 31: 5, pp. 83-97.

iii. Zhan Liu, Kaifeng Yuan, Yunzhi Ling, Haihui Tan, **Shuo Yang,** Experimental study on a-86° C cascade refrigeration unit with environmental-friendly refrigerants R290-R170. *Environmental Science and Pollution Research.* 2023, Vol. 30, pp. 97339-97352

Nomenclature

a	specific interfacial area (m^{-1})
A_B	interface area of bubble (m^2)
A_{BT}	fingering area at breakthrough moment (m^2)
A_{bd}	cross-sectional area of bubble (m^2)
A_{body}	interface area of bubble body (m^2)
A_C	cross-sectional area of microchannel (m^2)
A_{front}	interface area of bubble front cap (m^2)
A_i	invaded area of each phase (m^2)
A_{rear}	interface area of bubble rear cap (m^2)
A_{SS}	fingering area at steady state (m^2)
$A(z_{\mathrm{B}})$	cross-section area on slice (m^2)
C	Land trapping coefficient
Ca	Capillary number
Ca_B	Capillary number of bubbles
Ca_T	Capillary number of both phases
$C_{L,b}$	concentration at the liquid bulk (mol/L)
$C_{L,i}$	concentration at the interface (mol/L)
d	distance between centroid of upper front cap and the revolution axis (m)
d_1	gap between the cylinders in the 1st-order structure (m)
d_2	gap between the cylinders in the 2nd-order structure (m)
D	depth of channel cross-section of porous media (m)
D_{dif}	diffusivity (m^2/s)
D_h	hydraulic diameter (m)
FD_B	Fractal dimension at breakthrough moment
FD_S	Fractal dimension at steady state
H	Henry constant in dimensionless form
H_B	depth of bubble (m)
H_C	depth of microchannel (m)
j_B	bubble velocity (m/s)
j_G	superficial gas velocity (m/s)
j_L	superficial liquid velocity (m/s)
j_T	total superficial velocity (m/s)
k_{abs}	absolute permeability (m^2)
$K_{\mathrm{abs,100\%}}$	maximum absolute permeability (m^2)
$\mathrm{k}_{\mathrm{G}}^{*}$	relative permeability of gas phase
k_G	overall mass transfer coefficient of gas phase (m/s)
$\mathrm{k}_{\mathrm{L}}^{*}$	relative permeability of liquid phase
k_L	overall mass transfer coefficient of liquid phase (m/s)

$k_L a$	volumetric mass transfer coefficient (1/s)
L_{total}	length of porous media domain (m)
L_{body}	length of bubble body (m)
$L_{boundary}$	length of the boundary of the upper front cap (m)
L_C	length of unit cell (m)
L_f	length of bubble film (m)
L_{front}	length of bubble front cap (m)
L_G	length of gas slug/bubble (m)
L_L	length of liquid plug (m)
L_{rear}	length of bubble rear cap (m)
M	viscosity ratio between the invading phase and defending phase
M_G	transferred mass in mole of gas phase (mol)
M_L	transferred mass in mole of liquid phase (mol)
N	number of boxes
N_z	number of slices
P	pressure (Pa)
ΔP	pressure drop (Pa)
$P_{\mathrm{atmosphere}}$	atmospheric pressure (Pa)
P_{bd}	perimeter of bubble cross-section (m)
P_C	perimeter of microchannel cross-section (m)
P_{c}	entry capillary pressure (Pa)
$P_{G,b}$	partial pressure at the gas bulk (Pa)
$P_{G,i}$	partial pressure at the interface (Pa)
$P(z_B)$	interfacial perimeter on slice (m)
Q_G	gas flow rate (mL/h)
Q_L	liquid flow rate (mL/h)
r_t/r	curvature radius (m)
R_1	cylinder radius in the 1st-order structure (m)
R_2	cylinder radius in the 2nd-order structure (m)
Re_B	Reynolds number of bubble
Re_G	Reynolds number of gas phase
Re_L	Reynolds number of liquid phase
Re_T	Reynolds number of total phases
S_B	saturations at breakthrough moment
Sc_L	Schmidt number of liquid phase
S_{front}	projected area of the upper front cap (m^2)
S_G	saturation of the gas phase
Sh	Sherwood number
S_{HL}	saturation of the high viscous phase
S_i	saturation of each phase
$S_{\mathrm{i,G}}$	initial gas saturation

S_L	saturation of the liquid phase
S_{LL}	saturation of the lower viscous phase
$S_{\mathrm{r,G}}$	residual gas saturation
S_S	saturations at stead state
t	time (s)
T	elapsed time (s)
T_B	elapsed time for the finger cap to reach breakthrough time (s)
T_{in}	moment when cap enters the local visualization area (s)
T_{out}	moment when cap leaves the local visualization area (s)
T_S	elapsed time for the finger cap to reach steady state (s)
U_{cap}	velocity of finger cap (m/s)
u_i	Darcy velocity of the invading phase (m/s)
V_B	bubble volume (m^3)
V_{body}	volume of bubble body (m^3)
V_{front}	volume of bubble front cap (m^3)
V_{rear}	volume of bubble rear cap (m^3)
V_C	volume of cell (m^3) $V_C = W_C^2 L_C$
W	width of porous media domain (m)
W_B	width of bubble (m)
W_C	width of microchannel (m)
W_S	width of straight channel in porous media (m)
W_{C1}	width of throat 1 in porous media (m)
W_{C2}	width of throat 2 in porous media (m)
$\overline{W_B}$	average width of bubble (m)
X_{Cap}	location of finger cap (m)

Greek symbols

α	filling angle (°)
δ	width of body film (m)
θ	contact angle (°)
θ_R	receding contact angle
μ	dynamic viscosity (Pa·s)
μ_{ave}	saturation-averaged dynamic viscosity of the defending phases (Pa·s)
μ_d	dynamic viscosity of the defending phase (Pa·s)
μ_{HL}	dynamic viscosity of the high viscous phase (Pa·s)
μ_i	dynamic viscosity of the invading phase (Pa·s)
μ_{LL}	dynamic viscosity of the lower viscous phase (Pa·s)
ρ	density (kg/m^3)
σ	surface tension (N/m)
σ_d	surface tension of dispersed phase (N/m)
Φ_B	bubble volume fraction
Δ	resolution scale

β_0	zeroth Betti number
β_1	first Betti number
β_2	second Betti number
χ	Euler number
χ_0	initial Euler number
χ_{ip}^*	normalized Euler number of the invading phase

Abbreviations

BT	breakthrough moment
CF	capillary fingering
CZ	crossover zone
G	gas phase
GCS	geological carbon storage
GDL	gas diffusion layer
H-model	hierarchical porous media
HL	high viscous liquid
LL	low viscous liquid
SS	steady state
U-model	uniform porous media
VF	viscous fingering

Table of Contents

CHAPTER 1

Introduction

1.1 Background

1.1.1 Porous media

Porous media is defined as a solid object with connected holes, where the liquid or gas flow through. Porous media is ubiquitous in our lives and nature, e.g., sedimentary rock underground, rain-moistened soil, babies' nappies, water uptake in plants and gas exchange in lungs.

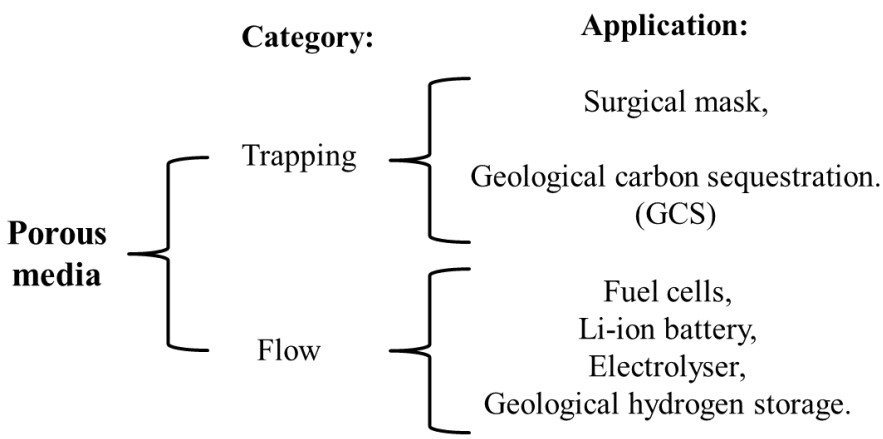

Figure 1-1 Category and industrial application of porous media.

Porous media have many applications ranging from small scales, e.g., industrial processes, to large scales, e.g., terrestrial/extraterrestrial subsurface resource extraction and storage. According to the flow motion in porous media, porous media can be divided into 2 categories shown in Figure 1-1. One category is that the fluid is surrounded by another fluid and they

both are trapped in the pore space. The most classic application is geological carbon sequestration (GCS). There are a lot of porous spaces between the underground rocks, which are filled with saline water and gas, as shown in Figure 1-2. Carbon dioxide can be captured from industrial processes, then compressed and injected into the pore space of the rock underground, where it can be stored in the reservoir permanently. Another application of porous structure underground is to storage hydrogen, which is belong to the second category in Figure 1-1. The second category is that all fluids can fully flow over a wide range of saturation. Little fluid is trapped in the porous media. It plays a significant role in energy fields, such as gas diffusion layer (GDL) in a fuel cells, Li-ion batteries, and electrolyzers.

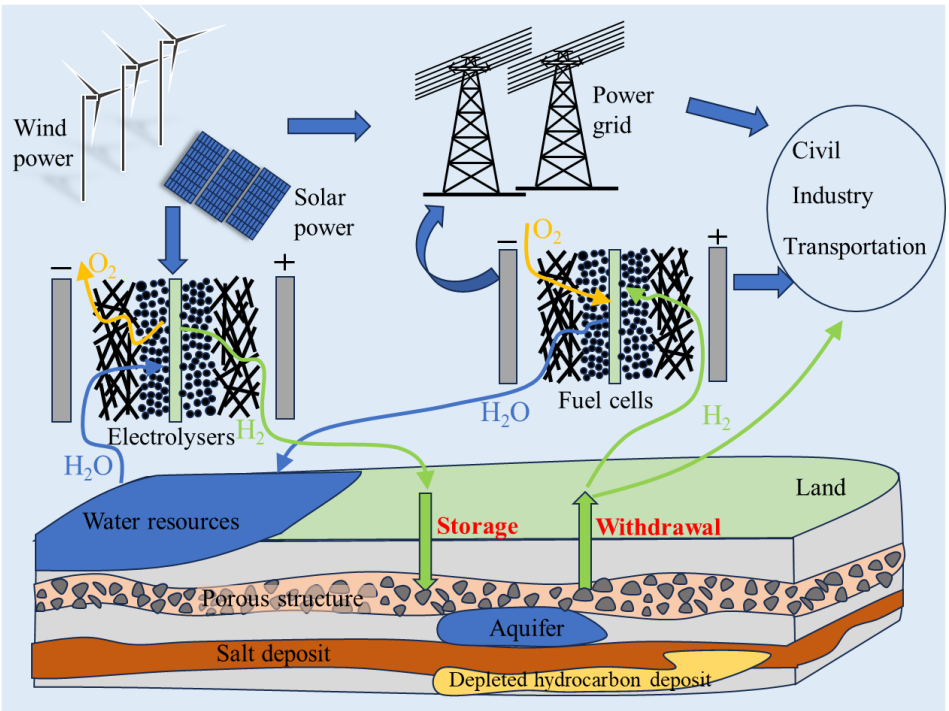

Figure 1-2 Schematic diagram on the production, storage and utilization of hydrogen energy

Nowadays, renewable sources like wind, solar, and hydro energy have been developed as alternatives to fossil fuels in response to growing energy demand and the urgent need to mitigate climate change. Hydrogen energy is a proven way to store excess electrical energy from such energy resources. As the cleanest energy source, hydrogen is promoted as a reliable, next-generation fuel. However, storage issues have hindered its development. As shown in Figure 1-2, geological hydrogen storage is considered as the promising solution [1]. Hydrogen can be safely and temporarily stored in rock space underground. When needed, hydrogen is extracted from the underground porous structure by cycle injection, which requires that the hydrogen cannot be permanently trapped in the pore space.

More generally, such process will occur in the myriad fields of science and technology where fluids pass through porous materials. Therefore, the research on pore-scale physics of fluid displacement process in porous media is greatly meaningful to reveal the dynamical behavior and fluid-mechanical forces.

1.1.2 Microfluidics

Microfluidics is an advanced technology that precisely controls and manipulates micro-scale fluids. Microfluidics originates from a concept called Miniaturized Total Analysis System (μTAS) that was first proposed by Manz, Graber, and Widmer et al.[2] in 1990. With the development of micromachining technology, we can fabricate various microstructure units such as micron to submillimeter fluid channels, reaction and detection chambers, filters and sensors on the micromodel. Various materials, e.g., glass, quartz, ceramic, metal, polymer and composite, have been developed to fabricate micromodels by using micromachining techniques, such as wet and dry etching, MEMS, micro-mechanical cutting, imprinting, lithography, embossing and advance micro-3D printing. Fluids can be manipulated precisely in the micron-scale space through fluid control or analytical instruments. The process, e.g., chemical reaction, separation, absorption and cell culture, can be finished automatically. Therefore, the potential development prospects of microfluidics are gradually being valued by academia and industry.

In the field of chemical and pharmaceutical, the microfluidic model is used as a modular microreactor shown in Figure 1-3 (a), by carrying out combinatorial chemical reactions or combining droplet technology [3]. Microscale channels in micromodels can achieve accurate feed control, enhanced mixing, fast reaction and side-reaction limitation. Energy and raw material savings as well as high product purity enable the micromodels to be used for drug synthesis, or for high-level synthesis of nanoparticles, microspheres, and crystals. And even a kind of "chemical factory or pharmaceutical factory on a micromodel" can be expected.

In the field of biomedicine, microfluidic bioreactor enables long-term culture and monitoring of extremely small populations of bacteria. As shown in Figure 1-3 (b), micro-fermentor systems can accelerate the process of strain screening and evaluation [4]. Besides, the clinical analysis can be integrated on a micromodel in Figure 1-3 (c) [5]. In recent years, integrated functions of microfluidic models are used to simulate the smallest functional units in human organs and realize drugs as shown in Figure 1-3 (d) [6]. The technology is used to understand and evaluate the effects of diseases, drugs, chemicals and food on humans. It was selected as one of the top ten emerging technologies of 2016 in the world economic forum.

All in all, due to the easy visualization of microfluidic models, porous structures have been fabricated on microfluidic models to study the multiphase behaviour in 2D porous media.

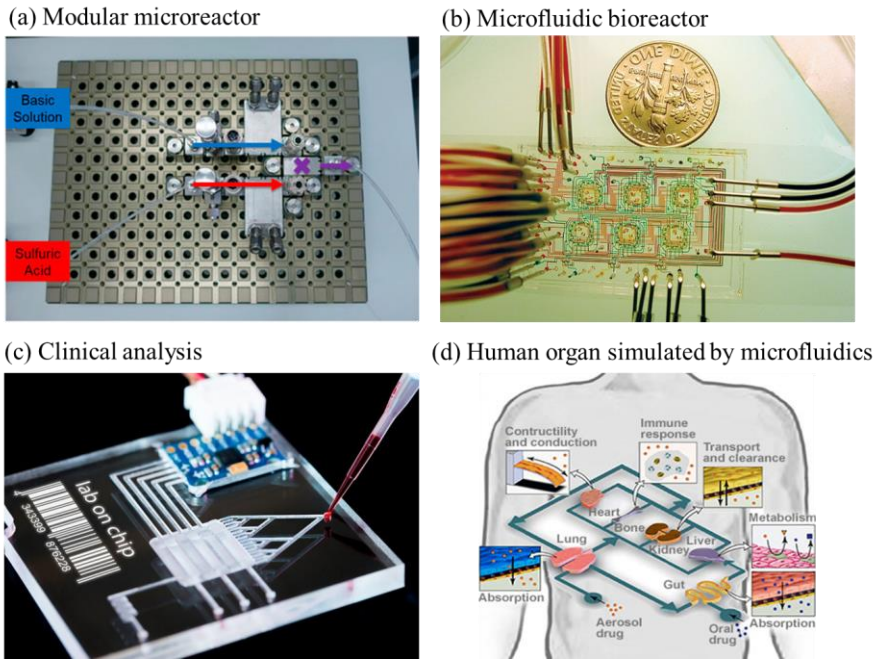

Figure 1-3 application of microfluidics: (a) modular microreactor [3]; (b) microfluidic bioreactor[4]; (c) clinical analysis [5]; (d) human organ simulated by microfluidics [6]. (Reprint by permission from the publisher)

1.1.3 Single straight microchannels as a simplified model for porous media

According to a discrete-domain model from Cueto-Felgueroso and Juanes [7], porous media can be conceptualized as an interconnected multistable microchannels network. The macroscopic invasion behavior in porous media results from the collective microscopic behavior of these microchannels. Therefore, before the main study of porous media in this thesis, I simplify the model by starting with gas-liquid flow in a single straight microchannel.

A single straight microchannel, as the basic unit of a complex microfluidic model, is fundamental and often addressed research topic[8]. The flow at the microscale is laminar and the straight microchannel can guarantee a stable flow. At the microscale, the effect of gravity on gas-liquid flow can be ignored. The gas-liquid flow in the straight microchannel is mainly controlled by the viscous force, surface tension, capillary force and inertial force. In practical industrial applications, one single microchannel is not sufficient to achieve complex reaction process. As shown in Figure 1-3 (d), multiple microchannels of different types are often required. Due to the limited area of a micromodel, using meandering microchannels is often a compromise. However, Dean vortices and other centrifugal effects then need to be considered [9].

1.2 Objectives and methodologies

As described above, microfluidic widely exists in the field of chemical, pharmaceutical, biomedicine and subsurface. Extensive work has been devoted to transport in the porous media. But there are still some unknown phenomena and mechanisms to be explored. In this thesis, the broad aims and goals are to improve the understanding of how gas and liquid flow in microchannels as well as in porous media with uniform and hierarchical microchannel networks. Especially, I focus on dynamics interaction between gas and liquid phases including mass transfer on the interface and interfacial instability due to viscosity contract between phases. To achieve the aim and goal, the initial objectives were detailly set as follows:

Single straight microchannel

Starting with a simplified model for porous media, the research focuses on the mass transfer of deformed bubbles in straight microchannels:

1. Built microchannel test platform with high-speed imaging and fluid feeding system.
2. Study hydrodynamics of gas-liquid flow in straight microchannels with square and rectangular cross-sections.
3. Develop 2D projection and 3D slicing method based on the digital image process technique to measure the volume of bubbles especially deformed bubbles in rectangular and square microchannels, separately.
4. Derive scaling laws of bubble volume, velocity and volume fraction to characterize the micro-reactors.
5. Calculate the mass transfer coefficient on the base of bubble volume and derive empirical correlations and a theoretical model to predict mass transfer coefficient.

Porous media

The research focuses on two-phase displacement after breakthrough, viscous-dependent three-phase displacement in homogeneous porous media and hysteresis effect during cyclic gas-liquid invasion in hierarchical porous media:

1. Build porous media test platform with high-speed imaging and fluid feeding system.
2. Design and fabricate hierarchical porous media with multiple levels of pore sizes to mirrors the actual underground structure.
3. Draw flow regime phase diagram and compare it with the region boundaries proposed by literatures. Visualize fingering displacement morphologies at breakthrough moment and steady state.
4. Conduct quantitative study on the invasion velocity, saturation, complexity, connectivity and permeability based on the digital image process technique. Quantify the hysteresis effect during cycle injection by using Land model.
5. Explore the complete dynamical fingering evolution process before and after breakthrough to reveal the underlying mechanism of invading dynamics.
6. Analyze local invasion behavior by microscopically observation and reveal the mechanism of residue ganglia motion.

CHAPTER 2

State-of-the-Art Literature Review

Flow in microscopic space is a complex process. Due to its broad application prospects, gas-liquid flow at the microscale has been a hot research topic. This chapter reviews the research progress over the last few decades, from mass transfer of gas-liquid flow in a single microchannel as a simple model, to multiphase displacement in porous media with microchannel networks over the past decades.

2.1 Microchannel

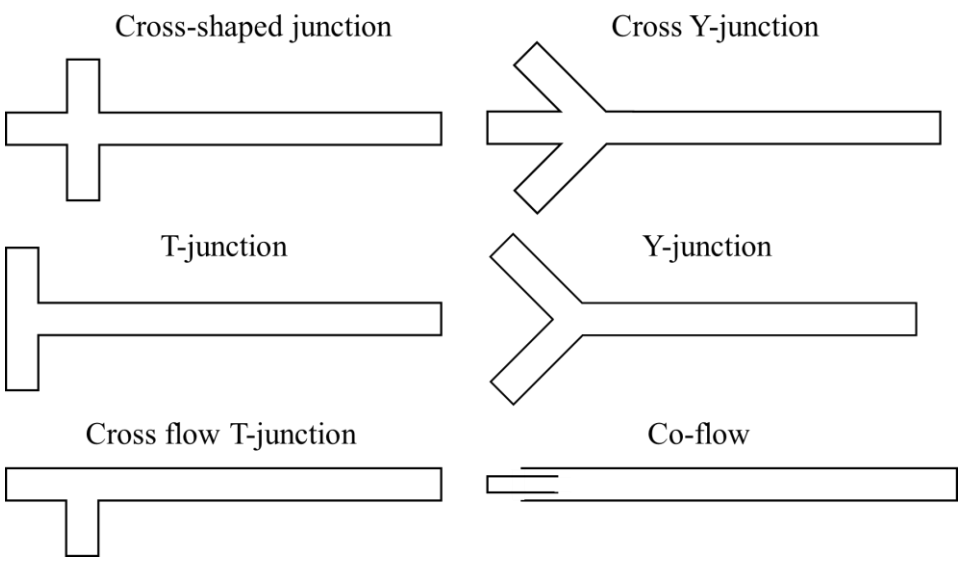

Figure 2-1 Junction configuration of microchannel.

In order to meet different application conditions, various cross-sectional shapes of microchannels have been applied, such as circular, square, rectangular, trapezoidal and so on. Based on the number and mixing degree of feed streams, the number of inlets and configuration of junctions both need to be customized. Figure 2-1 demonstrates the different configurations of mixing junctions at the entrance of the microchannels, including cross-shaped junction, cross Y-junction, T-junction, Y-junction, cross flow T-junction and co-flow. Different mixing junctions can produce different mixing degrees of fluids, which will generate different flow patterns [10].

2.1.1 Flow pattern

Over the past few decades, many studies focus on the exploration of gas-liquid flow patterns. The flow pattern map including different flow regimes may be firstly proposed by Baker [11], based on superficial gas and liquid velocities. As shown in Figure 2-2, five types of flow patterns were found, including bubbly, slug (plug), churn (froth/dispersed), slug-annular (transition) and annular. Although they were named differently in literature, they share some common characteristics:

- Bubbly flow. At the low j_G and high j_L, the irregularly shaped bubbles are dispersed in liquid phase and they do not flow in a horizontal line. Besides, the coalescence of bubbles may happen.
- Slug (plug) flow. Slugs with different lengths are generated and the shorter slug has a bullet shape. Due to the low j_G and j_L, the flow is stable. The distance between the slug and the size of slug are uniform.
- Slug-annular (transition) and annular flow. With the increase of j_G, the gas phase merges and thus elongated bubbles are generated. They are surrounded by a thin liquid film. The fluctuations occur at the interface but are not enough to block the bubbles.
- Churn (froth/dispersed) flow. At the high j_G and j_L, disruption resulting from periodical flooding-type churning waves will lead to unstable slug flow.

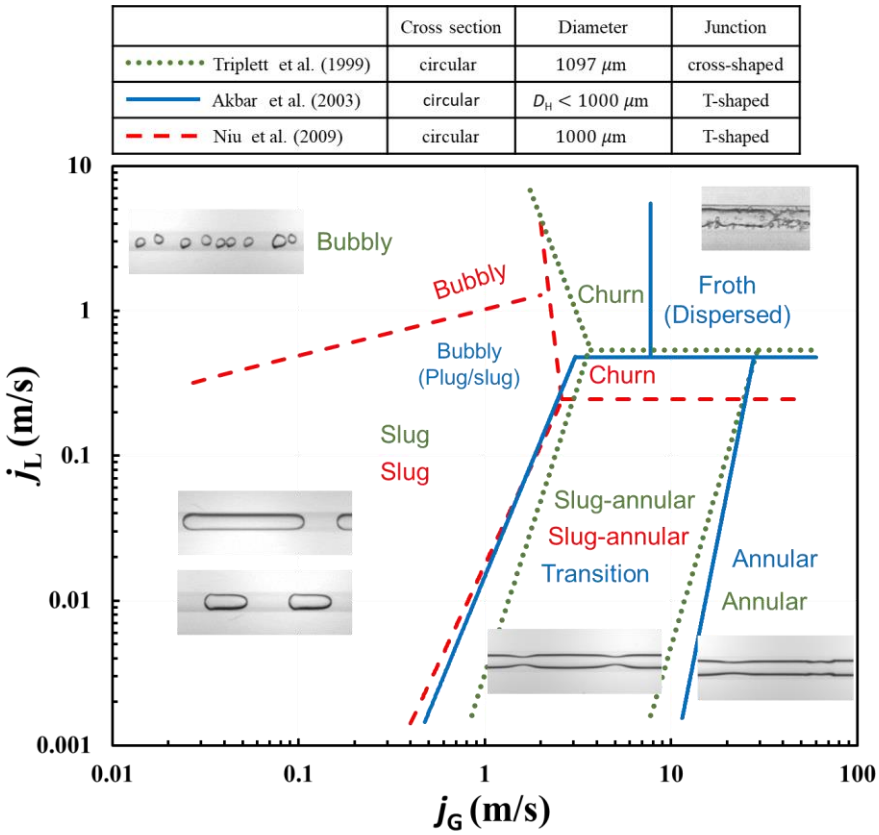

Figure 2-2 Comparison of the transition lines in gas-liquid flow pattern maps [12-14] and the flow pattern in different regions. (superficial gas velocity j_G and superficial liquid velocity j_L are calculated by the flow rate divided by the channel cross-sectional area, i.e., Q_G/A_C and Q_L/A_C. Reprint of churn image [12] by permission from the publisher)

The research on gas-liquid flow patterns transition can help predict flow patterns. Many studies proposed flow pattern transition lines to distinguish the different flow pattern transitions. Figure 2-2 shows the classical and popular transition lines in the flow pattern map reported by Triplett et al.[12], Akbar et al.[13] and Niu et al.[14]. Because their map was based on limited experimental data and different microchannel geometers, there are disagreements with boundaries. The transition line from slug to bubbly proposed by Triplett et al.[12] is curved, while the one proposed by Niu et al.[14] is straight. In particular Akbar et al.[13] didn't distinguish bubbly and slug flow. At the higher superficial gas and liquid velocities, Akbar et al.[13] defined the regime as froth (dispersed) flow, while Triplett et al.[12] and Niu et al.[14] defined as churn flow. Their boundaries between churn and the other four flow regimes are not consistent. However, the boundaries between slug-annular and annular as well as between slug to slug-annular coincide reasonably well. It should be noted

that Niu et al.[14] didn't distinguish the slug-annular and annular flow regime due to different flow pattern definitions.

2.1.2 Mass transfer

In geological carbon sequestration, dissolution trapping is the most important way of permanently sequestering CO_2. The dissolution is the mass transfer process of carbon dioxide to the aqueous phase. In single-phase flow, a classical Poiseuille flow profile with a maximum velocity on the center and a minimum velocity near wall is generated. In two-phase flow, the Poiseuille velocity profile is destroyed as shown in Figure 2-3 (b), because the flow speed of the dispersed phase is lower than the maximum velocity. Therefore, the recirculation is generated in both phases, as shown in Figure 2-3 (a). Recirculation can refresh the concentration near the gas-liquid interface. It is the recirculation that leads to the intensification of mass transfer between dispersed phases (bubble/slug) and continuous phase (liquid), which was validated by using micro-PIV and CFD simulation in Figure 2-3 (c,d).

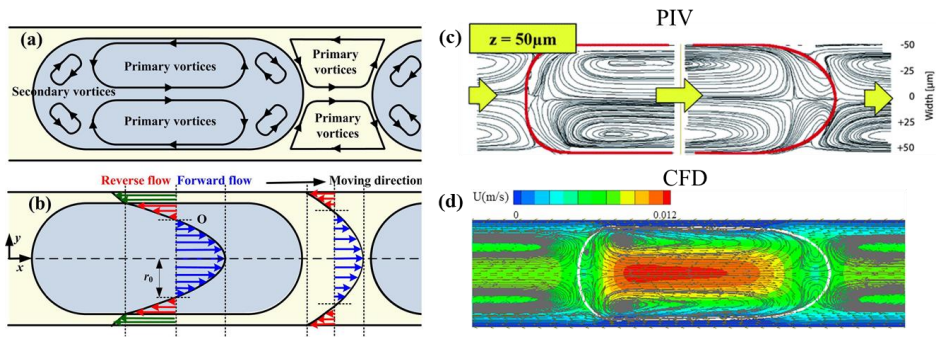

Figure 2-3 (a,b) Schematic diagram of recirculation [15]; (c,d) velocity profile from experimental Micro-PIV [16] and CFD simulation [17]. (Reprint by permission from the publisher)

Mass transfer between phases is described based on two-film theory, which is a classical theory of mass transfer process at gas-liquid interface, proposed by Whitman [18]. It simplifies the entire interphase mass transfer process as the molecular diffusion process of the component through two effective films. As shown in Figure 2-4, there exists stable gas stagnation layers (gas film) and liquid stagnation layers (liquid film) on both sides of the gas-liquid interface, respectively. The gas and liquid phases at the interface are in equilibrium. No mass transfer resistance is assumed at the phase interface. Besides, no mass transfer resistance is also assumed in the gas and liquid bulk outside the membrane layer, which means the

concentration gradient (or partial pressure gradient) is zero. Therefore, the mass transfer coefficient can be expressed as:

As for gas phase:

$$\frac{dM_G}{dt} = k_G A_B (P_{G,b} - P_{G,i}) \tag{2-1}$$

As for liquid phase:

$$\frac{dM_L}{dt} = k_L A_B (C_{L,i} - C_{L,b}) \tag{2-2}$$

Here, k_G and k_L are the overall mass transfer coefficient of gas phase and liquid phase, respectively. M_G and M_L are the transferred mass in mole of gas phase and liquid phase, respectively. A_B is the gas-liquid interface area. $P_{G,b}$ and $P_{G,i}$ are the partial pressure at the gas bulk and interface, respectively. $C_{L,b}$ and $C_{L,i}$ are the concentration at the liquid bulk and interface, respectively. Smaller bubbles can have more contact area with liquid phase per unit volume, which enhances mass transfer. The specific interfacial area a characterizes the ratio of surface area A_B and volume of cell V_C, which has an important influence on mass transfer coefficient. Therefore, most literatures focus on the overall mass transfer coefficient of liquid phase k_L (unit: m/s) and volumetric mass transfer coefficient $k_L a$ (unit: 1/s).

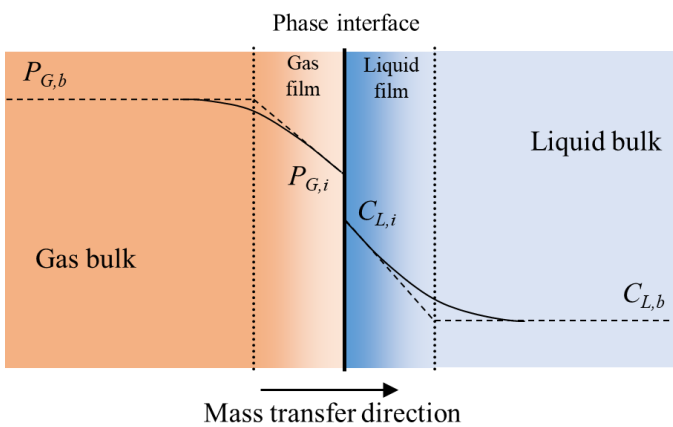

Figure 2-4 Schematic diagram of two film theory.

As shown in Figure 2-5, the unit cell consists of one slug (bubble) and one plug (liquid). It is reasonable to assume the mass transfer from gas to liquid phase only happens in a single unit cell, which means there is no mass transfer between unit cells. Due to mass conservation, the transferred mass in mole of gas phase and liquid phase is equivalent: $\frac{dM_G}{dt} = -\frac{dM_L}{dt}$. The volume of bubble decreases along the microchannel because of mass transfer, as shown in Figure 2-5.

According to ideal gas law, the mole mass of bubble can be represented as:

$$M_G = \frac{P_B V_B}{RT} \tag{2-3}$$

Substituting Equation (2-3) into Equation (2-2), the overall mass transfer coefficient of liquid phase k_L can be calculated:

$$k_L = -\frac{1}{RTA_B(C_{L,i}-C_{L,b})}\frac{d(P_B V_B)}{dt} = -\frac{1}{RTA_B(C_{L,i}-C_{L,b})}\left(P_B\frac{dV_B}{dt} + V_B\frac{dP_B}{dt}\right) \tag{2-4}$$

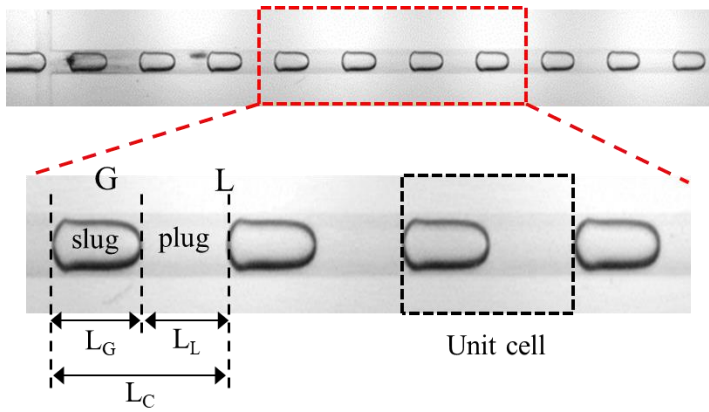

Figure 2-5 Schematic diagram of unit cell.

The key to calculating k_L is to measure the bubble volume change rate $\frac{dV_B}{dt}$. As for most of the studies, the actual parameter to be monitored is the length of bubble [19, 20]. To a first approximation, bubble volume is calculated by multiplying the cross-section area of microchannel and length of bubble L_G. To increase precision, some researchers have considered the rear and cap of the bubble as two hemispheres. The film of the body is still assumed to be uniform, which indicates a constant cross-section area of the bubble body. In other word, bubble body is considered as a cylindrical shape. The volumes of the rear and cap are calculated by the formula for the volume of a sphere. The volume of the body is calculated by multiplying the cross-section area of the body by the body length [21, 22]. This technique is, therefore, effectively limited to the bubbles with a bilateral (cap-to-rear) symmetrical shape as shown in Figure 2-6 (a,b). However, with the increase of superficial liquid velocity j_L, bubbles become bullet-shaped gradually. Bubble cap becomes pointed and the rear becomes flat as shown in Figure 2-6 (c-e). They are completely bilateral asymmetrical, and the width of the body film δ varies along the body length [23, 24]. The above assumptions for simplicity are not valid anymore for deformed bubbles. Consequently, the 3D bubble reconstruction and new bubble volume calculation method are necessary to develop to estimate the mass transfer coefficient.

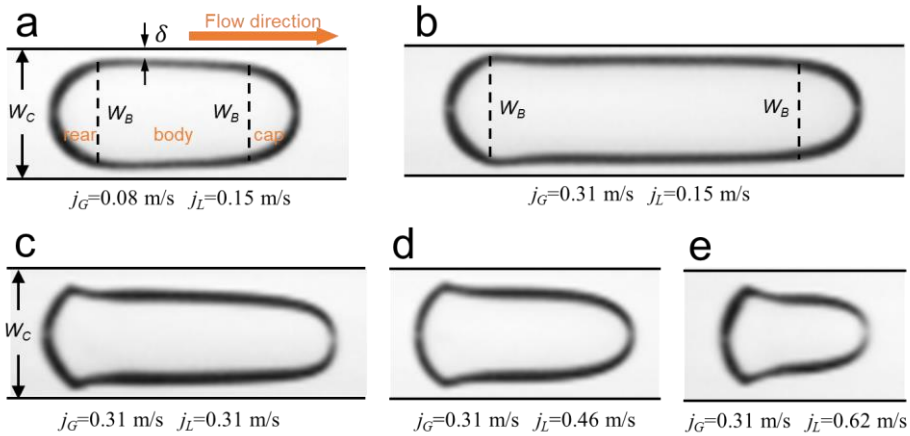

Figure 2-6 (a-b) Symmetric bubbles; (c-d) Deformed bubbles.

Micro laser-induced fluorescence (micro-LIF) is an advanced technology to obtain the concentration distribution in liquid plugs [25, 26]. But due to the limitation of equipment, LIF was not used in this thesis. Although this thesis only focuses on the experimental method, CFD is a useful tool to obtain information that cannot be obtained from experiments [17]. Verification between numerical and experimental results can enhance the reliability of conclusion.

2.2 Porous media with microchannel network

Porous media is a network of microchannels formed by interconnected pores, which widely exists in industrial and subsurface applications. Fluids can flow through or trap in the pore space. When two fluids flow in porous media, the interface between fluids may become unstable. Such instability will limit extraction effectiveness and cause leakage in the applications.

2.2.1 Interfacial instability

The interface will become unstable when a more viscous fluid is displaced by a less viscous fluid, and thus fingering pattern will occur [27]. Although the first scientific study was conducted by Hill (1952) [28], the interfacial instability is called Saffman-Taylor instability[29] due to Saffman and Taylor's now-classical work in 1958 about essentially identical liner-instability analyses of one-dimensional displacement [29]. Since then, this beautiful physical phenomenon has attracted extensive attention. Various configurations have been used to investigate this phenomenon. In the rectangular configuration, the pattern will evolve until a single stable finger is generated (Figure 2-7 (a)). In the radial configuration, fingering will spread and split up successively (Figure 2-7 (b)). This instability is traditionally investigated in a very thin space between two closely spaced parallel glass sheets, which is

called Hele-Shaw cell. In addition, researcher also fabricated the solid structure like posts in the cell to form a porous space. Zhao et al. [30] studied fluid-fluid displacement in disordered media patterned with vertical posts. The post pattern forms a macroscopically homogeneous porous structure, in which incomplete pore-scale displacement can be observed. The non-compact viscous fingering pattern with branches was generated in the radial direction.

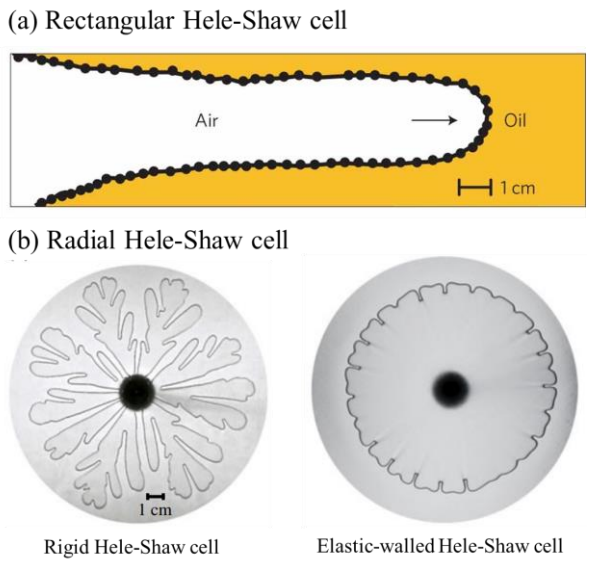

Figure 2-7 Fingering pattern in literature: (a) Hele-Shaw cell with rectangular configuration [31]; (b) Hele-Shaw cell with radial configuration [32]. (Reprint by permission from the publisher)

2.2.2 Phase diagram and finger pattern of two-phase displacement

Apart from the Hele-Shaw cell, the porous structure is also fabricated in porous media. The holes are connected to each other, forming a microchannel network. Intensive work has been conducted to study the instability dynamics at pore scale [33] and macroscale [34]. In addition, microscale is also an interesting topic of research. In porous media with microscale structures, related dynamic capillary pressure, relaxation time [35] and transient flow states [36] play a significant role in the fingering displacement process. Depending on the wettability of invading phase and defending phase, the displacement process is divided into two types: drainage and imbibition. When non-wetting fluid displaces wetting fluid, this process is called drainage. The imbibition process is the opposite. Viscous force, surface tension and capillary force mainly control the flow motion, which can be characterized by two dimensionless numbers: the capillary number *Ca* and the viscosity ratio *M* of the invading phase to the defending phase.

$$Ca = \frac{\mu_i u_i}{\sigma_d} \tag{2-5}$$

$$M = \frac{\mu_i}{\mu_d} \tag{2-6}$$

Where, μ_i and μ_d denote dynamic viscosity of the invading and defending phases, respectively. u_i is Darcy velocity of the invading phase, and σ_d is the surface tension of dispersed phase. As shown in Figure 2-8, the phase diagram of fingering displacement was mapped based on the dimensionless numbers $Log_{10}Ca$ and $Log_{10}M$. The morphologies of the fingering pattern in different regimes are illustrated, including viscous fingering (VF), capillary fingering (CF), crossover zone (CZ) and stable displacement (SD) [37, 38].

- Viscous fingering (VF). In the region with lower $Log_{10}M$ and high $Log_{10}Ca$, a narrow finger pattern with branches is observed because the viscous force mainly controls the process. At the moment when the cap of the finger reaches the outlet, called breakthrough, the displaced area is the lowest.
- Capillary fingering (CF). At high viscosity ratio and low capillary number, the finger pattern becomes wide and the number of branches reduces. Capillary fingering is mainly controlled by capillary force.
- Crossover zone (CZ). The width of the finger is between that in CF and VF regimes, because displacement is controlled by the viscous force and capillary force simultaneously.
- Stable displacement (SD). When the viscosity ratio and capillary number are both high, the interface keeps stable and the displaced area is the highest at the breakthrough moment.

Many studies have been conducted to explore fingering pattern transition and the boundaries to distinguish different regimes, which provides guidance for the prediction of flow patterns. By deriving a simple force balance relating viscous to capillary forces, Lenormand et al. [39] firstly proposed the boundaries to distinguish different flow regimes in a pore network as shown in blue solid lines of Figure 2-8. The result was obtained by experiment and simulation, but position of the boundaries is system-dependent. The now-famous boundaries (green dot lines) were defined by Zhang et al. [40] based on an almost homogeneous and isotropic micromodel. It is unlike for the multiple flow regime to coexist, so the area of crossover zone is narrower than that defined by Lenormand et al. [39]. Recently, Guo et al. [41] also proposed the boundaries on the base of the drainage process in the pore network that represents the pore distribution of Berea sandstone. As shown in red dash lines of Figure 2-8, the boundaries are completely inconsistent with that of Zhang et al. [40]. The crossover zone between the CF and VF is extremely narrow. The reason may originate from pore size distribution and domain size.

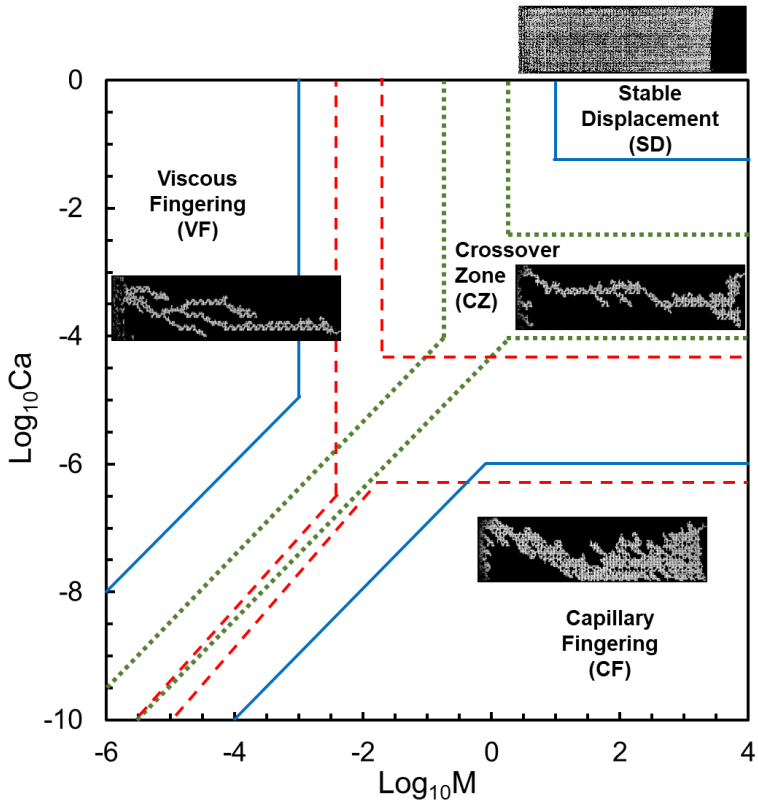

Figure 2-8 Phase diagram of fingering displacement (blue solid lines, green dot lines and red dash lines are the boundaries between different displacement patterns defined by Lenormand et al. [39], Zhang et al. [40] and Guo et al. [41], respectively.).

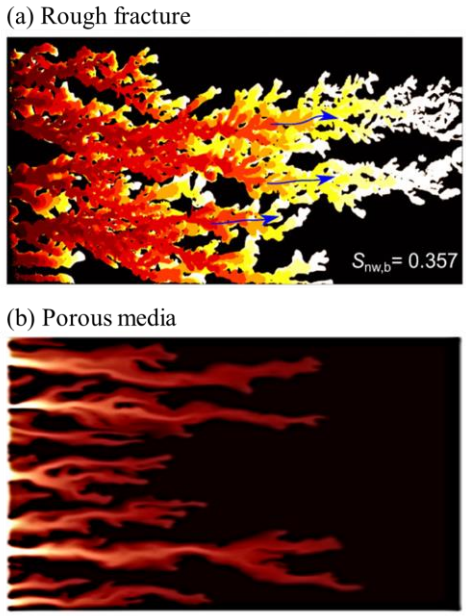

Figure 2-9 Fingering pattern in rough fracture [42] and porous media [43]. (Reprint by permission from the publisher)

As mentioned above, fingering displacement in porous media is greatly important in many subsurface and industrial applications. However, this non-compact fingering pattern resulting from interfacial instability has an important influence on extraction effectiveness and leakage risk, which are related to economic benefits and storage safety. Therefore, extensive work focused on the dynamic evolution process of fingering pattern in rough fracture and porous media as shown in Figure 2-9. In addition to experiments, lattice Boltzmann method (LBM) [44, 45] was used to simulate the complex fingering displacement and explore the mechanisms of interfacial instability. The fingering pattern was quantified by parameters such as cap velocity [46], finger width [47], number of fingers [48], interface curvature [49-51], breakthrough time [46, 48], invading area [52] and saturation [48, 53], fractal dimension [47, 54], and pressure difference [53, 55]. Most research was limited to the displacement process before or at the breakthrough moment. However, evolution of fingering patterns after breakthrough is still of great importance. It can provide guidance on how to achieve relatedly high extraction efficiency in the shortest time and avoid leakage. The mathematical model based on non-equilibrium effects was created [56, 57] and gradually modified [58-60] to describe two-phase displacement process. After breakthrough, the evolution of displacement pattern varies in different flow patterns. When the displaced area becomes maximum, a steady state reaches. Yet, the evolution process from breakthrough to steady state remains unclear. In different flow regimes, the dynamical transition of fingering patterns from breakthrough to steady state and the underlying mechanisms still need to be explored further [47].

2.2.3 Three-phase displacement

In various geological gas sequestration procedures, invading gases like CO_2 or H_2 are injected into aquifers containing multiple fluids, such as depleted oil reservoirs nearing the end of exploitation following water/brine flooding. Often, to enhance storage efficiency or subsequent extraction processes, operational strategies can be enriched by alternating injections of multiple fluids, such as tertiary gas injection [61] and water-alternating-gas [62]. In this context, the gas interacts with both water and oil phases. Thus, it is imperative to comprehensively understand the mechanisms underlying gas invasion into multi-fluid systems within porous media.

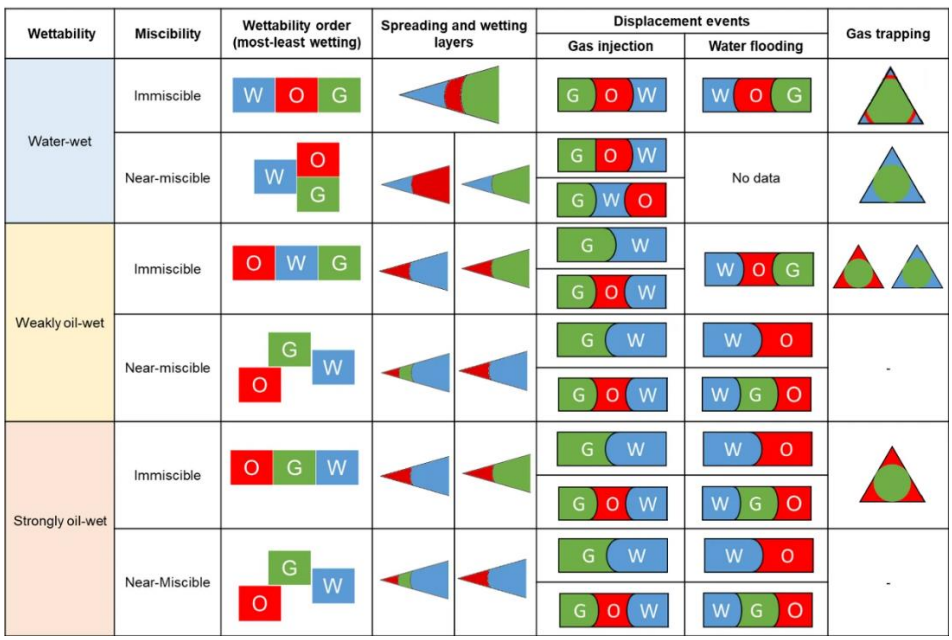

Figure 2-10 The wettability orders, spreading and wetting layers, and double displacement events for various wettability and miscibility conditions during capillary-dependent three-phase displacement in porous media. (Reprint by permission from the publisher)

In three-phase displacement, the dynamics of gas (G) invasion into multi-fluids G→(L→L) has greater complexity compared to liquid invasion L→(L→L). This complexity arises from interface instabilities due to the significantly low viscosity of the invading gas and the coupled interfacial interactions at the gas-liquid (G-L) and liquid-liquid (L-L) interfaces. Mathematically, there are six potential three-phase displacement scenarios: $F_1 \rightarrow (F_2 \rightarrow F_3)$, $F_1 \rightarrow (F_3 \rightarrow F_2)$, $F_2 \rightarrow (F_1 \rightarrow F_3)$, $F_2 \rightarrow (F_3 \rightarrow F_1)$, $F_3 \rightarrow (F_1 \rightarrow F_2)$, $F_3 \rightarrow (F_2 \rightarrow F_1)$. It is conventionally assumed that gas remains the most non-wetting phase throughout these displacement processes. Together with conventional flow imaging platform [63, 64], X-ray micro-CT scanning [65-67] and numerical approaches such as Lattice Boltzmann methods (LBM) [68-

70], effects of saturation history [71, 72], wettability [73-75], pressure (Primkulov et al. 2019), spreading [76], and layer drainage [77] on the three-phase displacement have been explored in porous media.

Singh et al. [78] reviewed capillary-dominated displacement in porous media. Alhosani et al.[79] also summarized multiple displacement events for capillary-dominated flow conditions, as shown in Figure 2-10. The most wetting phase typically occupies the smallest pores, throats, and the wetting layers. Conversely, the most non-wetting phase tends to predominantly reside in the central regions of larger pores, whereas the intermediate-wet phase occupies medium-sized pores or forms spreading layers between the other phases. However, apart from capillary-dominated displacement, research on viscosity-dominated three-phase displacement are rare, and the pore-scale physics remains incompletely revealed in the literature.

2.2.4 Hysteresis effect during cyclic gas-liquid invasion

Hydrogen is a promising green energy source that can be used to store excess electricity generated due to erratic production of renewable energy sources such as wind, solar and hydro. Underground hydrogen storage (UHS) is considered an effective way of storing hydrogen [80]. The vast underground pore space can be used to store large quantities of hydrogen.

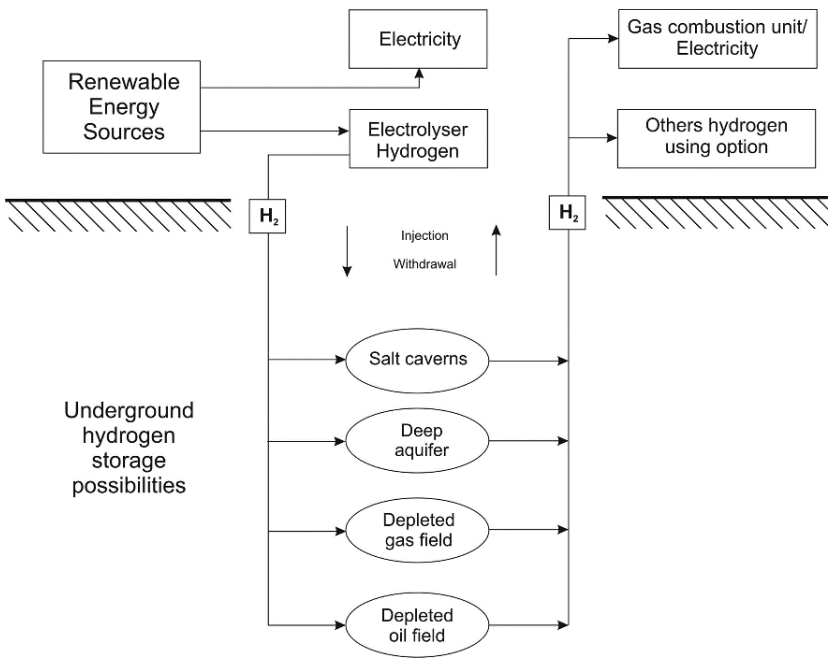

Figure 2-11 Scheme of the underground hydrogen storage facility [80]. (Reprint by permission from the publisher)

As shown in Figure 2-11, UHS entails both temporary storage and subsequent extraction processes, which correspond to water-alternating-gas displacement of H_2 injection (drainage) and withdrawal (waterflooding) [81]. In UHS, some H_2 may unavoidably be lost due to residual trapping. The residual phase distribution is affected by hysteresis effect of saturation [62] and relative permeability [82] during cycle injection influence. Over the past few decades, numerous models have been developed to describe gas trapping.

Land Trapping Model (1968) [83] stands out as one of the most widely-utilized models, defining ultimate residual oil saturation as a function of the initial water saturation.

$$S_{\mathrm{r}} = \frac{S_{\mathrm{i}}}{1+C\,S_{\mathrm{i}}} \tag{2-7}$$

Here, S_{i} and S_{r} are initial saturation and residue saturation, respectively. C is the Land trapping coefficient.

Carlson Trapping Model (1981) [84] is a simplified hysteresis model that requires the bounding drainage and waterflood curves. The saturation of trapped phase is determined by shifting the bounding waterflood curve to intersect the intermediate initial saturation at the point of flow reversal.

$$S_{\mathrm{r}} = S_{\mathrm{r,max}} - \Delta S \tag{2-7}$$

Here, ΔS is the shift in the waterflood scanning curve with respect to the imbibition bounding curve.

Jerauld Trapping Model (1997) [85] is an extension of the Land trapping model that considers the "plateau" observed in the initial-residual curves for mixed-wet rocks.

$$S_{\mathrm{r}} = \frac{S_{\mathrm{i}}}{1+CS_i^{1+b/C}} \tag{2-7}$$

A second tuning parameter b was introduced apart from the Land trapping coefficient C. When b is equal to 0, this model becomes Land model. When b is equal to 1, the trapping curve has a zero slope at S_{i}, which is equal to 1.

These models play in important role in quantifying the strength of hysteresis effect of cyclic invasion in subsurface storage and extraction application.

2.2.5 Heterogeneous porous structure

In addition to homogeneous porous structures, recent research endeavors have increasingly focused on heterogeneous porous media, which closely mirrors the actual underground structure. Heterogeneous structures encompass surface attributes such as wettability [86, 87], as well as topological features like pore size distribution [88, 89] and connectivity [90].

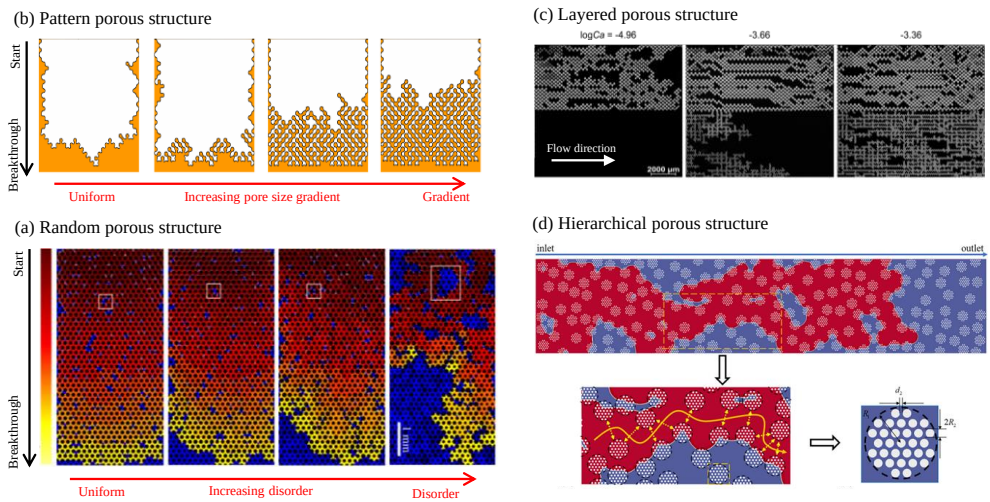

Figure 2-12 Invasion pattern in: (a) gradient porous structure [88]; (b) random porous structure [87]; (c) layered porous structure[91]; (d) hierarchical porous structure[92]. (Reprint by permission from the publisher)

Figure 2-12 (a, b) illustrates that research on the impacts of geometry in literature is divided into two categories: random and patterned structures. In patterned porous structures, manipulating the pore size gradient along the flow direction has emerged as an effective strategy for suppressing viscous fingering [88] and capillary fingering [89]. In random porous structures, previous studies [86, 87] have explored the intricate relationship between wettability and disorder, revealing that as disorder decreases, the interface tends to stabilize.

These studies only considered porous structures with a single level of pore sizes. However, in natural subsurface rock formations and synthetic materials such as porous electrodes and fibrous materials, porous structures typically have multiple levels of pore sizes. Previous investigations have demonstrated that sharp stratification [93, 94], dual permeability [91, 95] and dual porosity [96] within the porous structure profoundly influence fluid pathways (Figure 2-12 (c)). The limitation is that these dual structures are directly segregated into upper and lower layers.

In practical applications, beyond the evident layering, various levels of pore sizes are commonly distributed throughout the entire porous domain. This configuration constitutes a hierarchical or fractal structure characterized by dual/multiple permeability. As shown in Figure 2-12 (d), Suo et al. conducted the numerical exploration of viscous fingering [97] and capillary fingering [92] in hierarchically structured porous media. They provided comprehensive insights into fluid-fluid displacement control in hierarchical porous media, spanning a wide range of flow conditions from capillary- to viscous-dominated modes. They uncovered three fluid-fluid displacement modes. The results show that a higher porosity of

the second-order porous structure enables the displacement to maintain compactness across a broad range of wettability conditions.

CHAPTER 3

Experimental setups and methods

In this chapter, the microfluidics platform and experiment procedure are presented. Besides, the geometry of micromodel (microchannel and porous media), 3D bubble reconstruction and bubble volume calculation, image processing method and data processing procedure are introduced.

3.1 Geometry of micromodels

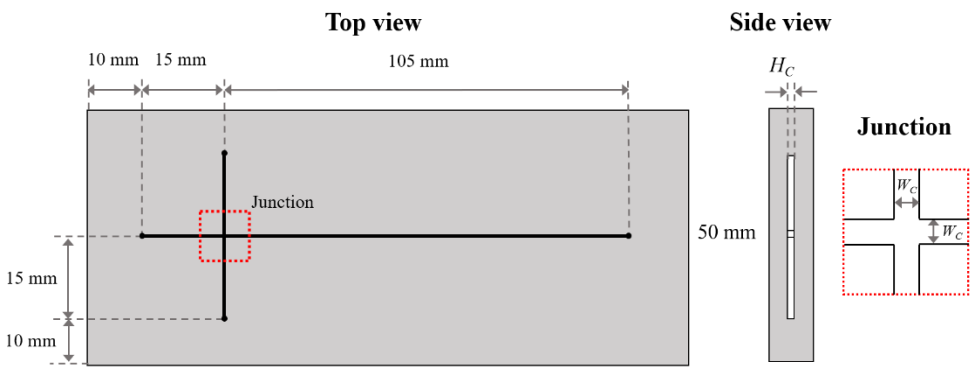

	Width W_C	Depth H_C
Square	600 μm	600 μm
Rectangular	600 μm	300 μm

Figure 3-1 Geometrical details of the rectangular and square microchannels (**Papers i and ii**).

Figure 3-1 indicates the geometry of two microchannels with square and rectangular cross-sections, manufactured by Little Things Factory, Germany. A cross-shaped junction downstream of the inlets merges the flows from the three inlets. After the junction, a straight main microchannel with 105 mm length is connected. As for square microchannel, the width

and depth are both 600 μm. As for rectangular microchannel, the width and depth are 600 μm and 300 μm. The accuracy of the width and depth is within ±10 μm. The material is glass, so it is intrinsically hydrophilic for water.

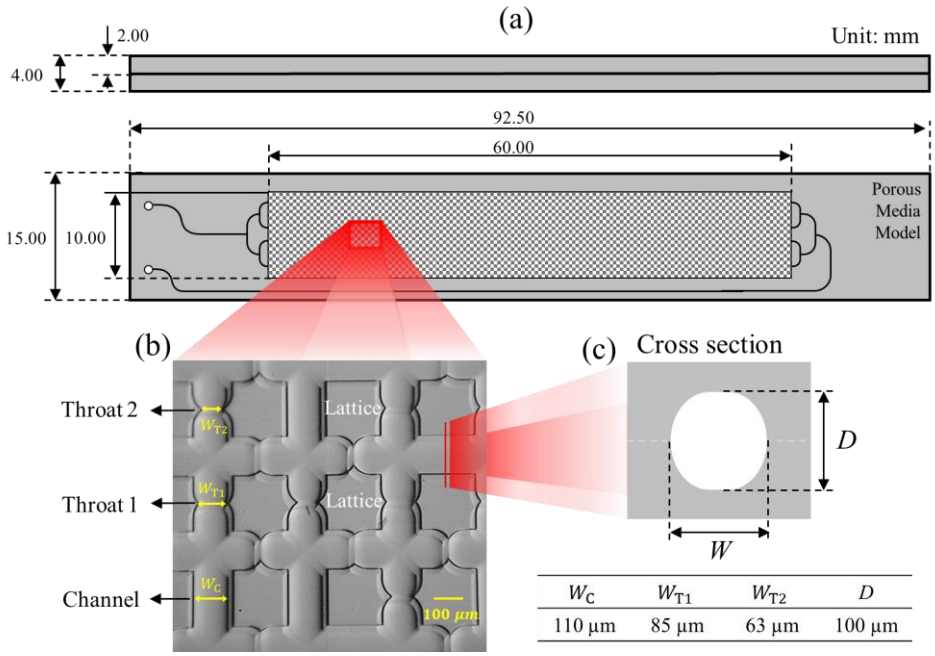

W_C	W_{T1}	W_{T2}	D
110 μm	85 μm	63 μm	100 μm

Figure 3-2 Geometrical details of porous patterned microfluidic model (**Papers iii and iv**): (a) dimensions with mm unit; (b) geometries of porous patterns; (c) cross section of the channel.

Figure 3-2 shows the geometry of the porous media model with microchannel network, manufactured at Dolomite company. The porous media model involves a gas inlet and liquid outlet and a 60×10 mm porous domain. The gas inlet and liquid outlet are designed as a tree-shaped layout, which can ensure a uniform inflow and outflow. Figure 3-2 (b) shows the micrograph of the porous domain. The microchannel network is formed by the orderly arrangement of the different lattices. There are straight channels and two types of throats with the width of 110 μm, 85 μm and 63 μm, respectively. Figure 3-2 (c) indicates the cross-section of channels with the same depth *D* 100 μm. The material is quartz glass with 5 nm surface roughness (Ra). Its measured contact angle is 38.3° for water, so it is hydrophilic. The channel is fabricated by the etching process, which will further reduce the contact angle. The contact angle measurements experiment (see the last row of Table 3-6) found that glycerol has a similar static contact angle as the water.

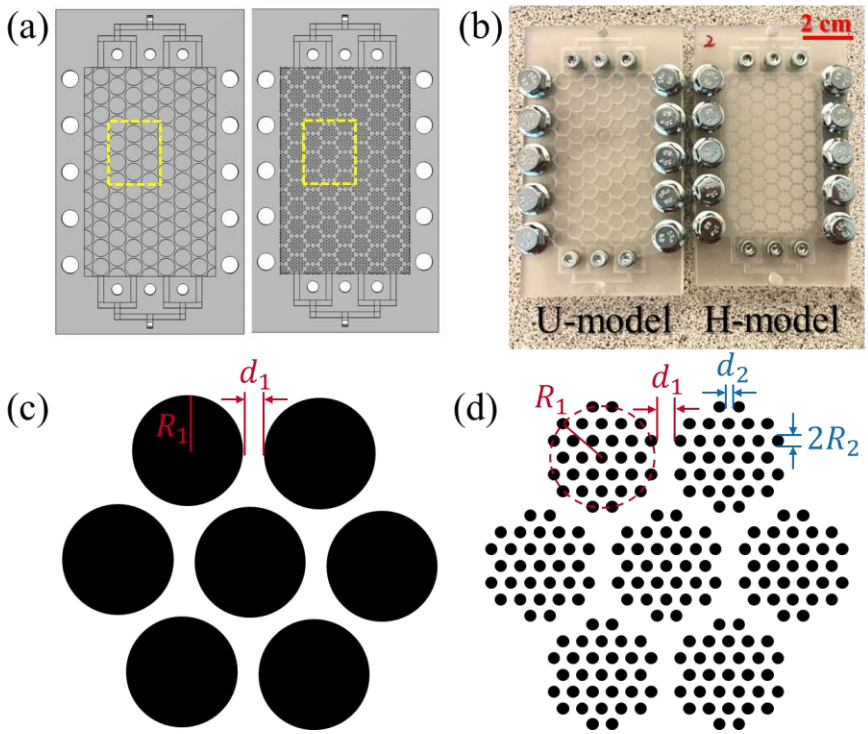

Figure 3-3 Geometrical details of the uniform and hierarchical porous media model (**Paper v**): (a) The schematic diagrams of lower plate. (b) 3D printing of the uniform and hierarchical micromodels, named as **U-model** and **H-model** respectively. The periodic geometries of (c) the uniform model with 1st-order structure and (d) the hierarchical model with 1st-order and 2nd-order structures.

The porous media micromodel is composed of upper and lower plates, both of which were separately fabricated using resin materials through 3D printing. Both uniform and hierarchical models have flat upper plates. As depicted in Figure 3-3 (a, b), screws along the model's edges securely fasten the upper and lower plates. The porous structure was achieved by processing the cylinders on the lower plate. Hierarchical structure (**H-model**) features dual permeability through the inclusion of both 1st-order and 2nd-order structures. As for the 2nd-order structure, 31 small cylinders with radius R_2 were arranged on the regular hexagonal grids with the 2nd -order gap d_2 to form a cell with radius R_1. As shown in Figure 3-3 (d), such cells were arranged on same hexagonal grids to form 1st-order structure with the 1st-order gap d_1. The entire 6996×4406×100 μm porous domain contains 7 rows and 11 columns of cells. For comparison, the uniform structure (**U-model**) only with 1st-order structure was designed as shown in Figure 3-3 (c). The big cylinders with R_1 were fabricated to replace each cell in hierarchical porous media and the gap between cylinders is kept the same d_1. These size parameters of uniform and hierarchical structures are shown in Table 3-1. The total porosities

of uniform and hierarchical structures were calculated based on the design, which are 17.44% and 69.34%. The tree-like layouts were assembled to the outlet and inlet to generate uniform inflow and outflow.

Table 3-1 Geometric parameters of the uniform and hierarchical designs

	1st-order structure			2nd-order structure		
	d_1 (mm)	R_1 (mm)	φ_{1st}	d_2 (mm)	R_2 (mm)	φ_{2nd}
Hier	0.66	2.70	29.98%	0.42	0.30	61.74%
Unif	0.66	3.00	17.4%	/	/	/

3.2 Experimental platform and Experimental procedure

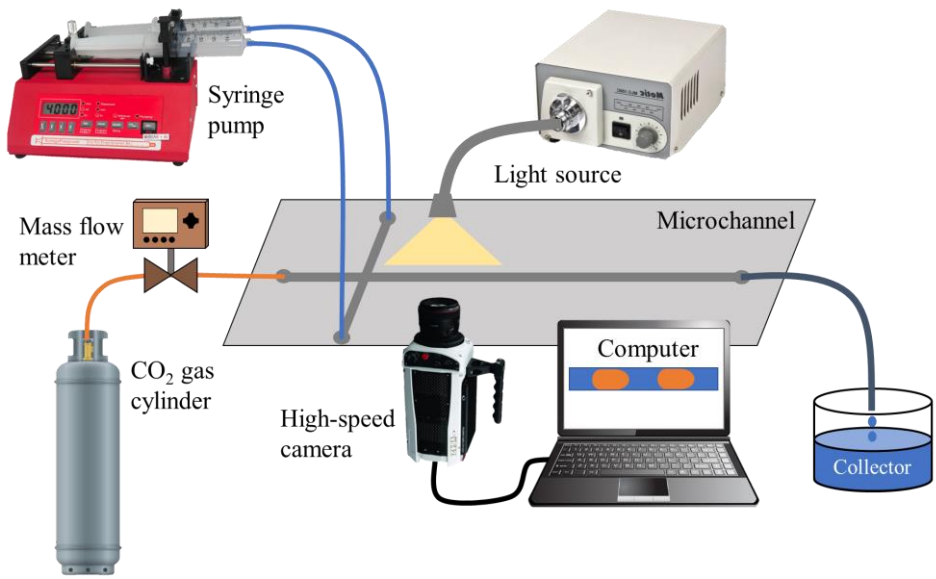

Figure 3-4 Experimental setup for single microchannel (**Paper i and ii**).

Microfluidics platform was built up to explore gas-liquid flow and mass transfer in microchannels. As shown in Figure 3-4, the liquid was injected into the two side inlets, controlled by the syringe pump (New Era NE-4000). The gas was introduced into the center inlet, controlled by the gas mass flow meter (Bronkhorst EL-Flow prestige FG-200CV). Gas and liquid merged at the junction and then the gas-liquid flow is generated in the main microchannel. A high-speed camera (Phantom V611, maximum 6242 fps at full resolution 1280 × 800) equipped with a lens (micro-NIKKOR 105mm) was used to capture the images

and videos of the gas-liquid flow. Light source provided powerful cold light (Motic, MLC-150C) to increase the brightness for photography. The reduced recording resolution (1280 × 104) was selected to increase the recording speed to 20000 fps at a 20 μs exposure time. By counting the number of pixels across the channel width, the spatial resolution was measured and was 19.6 μm/pixel. Computer was connected to the camera to record the data. The collector was used to collect the residue water.

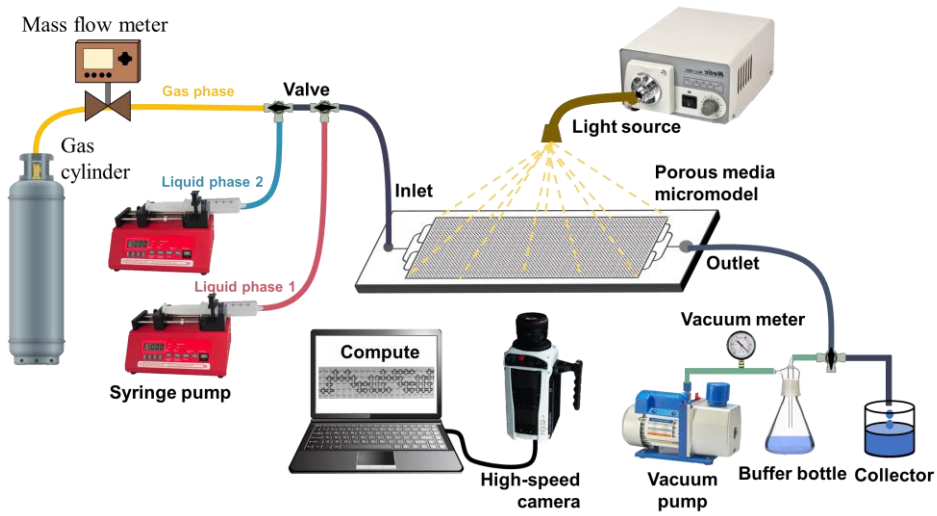

Figure 3-5 Experimental platform for porous media (**Paper iii, iv and v**).

Another microfluidic platform was built specifically for imaging fluid invasion in porous media. In different papers, there may be some minor differences in the setups and experimental procedures. As shown in Figure 3-5, the experimental platform consists of a fluid feeding system, a horizontally placed porous media micromodel, a high-speed imaging system and a residue liquid collector. In fluid feeding system, the gas injection was controlled by mass flow meter (Bronkhorst EL-Flow prestige FG-200CV) and the liquid injection was controlled by syringe pumps (New Era NE-4000). By adjusting the gas and liquid injection sequence, gas-liquid displacement (**Paper iii**), gas invasion into multi-fluid systems (**Paper iv**) and gas-liquid cyclic invasion (**Paper v**) can be achieved. The images and videos of invasion process in porous media was captured by a high-speed camera (Phantom V611) equipped with a lens (micro-NIKKOR 105mm) in high-speed imaging system. A properly sized recording window at 24~2000 frames per second and 20 μs exposure time was performed on the whole porous domain. Light source (Motic, MLC-150C) provided the desired brightness for photography. In gas-liquid displacement and gas invasion into multi-fluid systems, the defending liquid phase needs to be injected into the porous media and completely filled before invasion of invading phase. To make sure no gas residue in the porous space, a vacuum pump was used to remove the gas from the micromodel until the vacuum degree reached approximately 10^{-2} bar. The buffer bottle was in place to prevent liquid from

entering the vacuum pump and causing any damage. The collector was used to collect the residue liquid.

3.3 Experimental conditions and dimensionless numbers

This chapter presents the experimental conditions of each paper. Due to its universality, dimensionless numbers can expand the physical phenomena of research to other scalable systems with different sizes. Therefore, dimensionless numbers, including Reynolds number, Capillary number, Sherwood number and Schmidt number, were calculated based on these operating parameters and presented in this chapter.

Paper i (rectangular microchannel):

As for the research on rectangular microchannel, the dispersed phase is CO_2 and the continuous phase is de-ionized water. The physical properties at 20.5 ± 0.5 °C of them are listed in Table 3-2.

Table 3-2 Physical properties at 20.5 ± 0.5 °C

Property		Unit	water	CO_2
Density	ρ	kg/m^3	998.2	1.797
Viscosity	μ	10^{-6} Pa · s	1005	15
Surface tension	σ	N/m	0.0728	-
Diffusivity	D_{dif}	10^{-9} m^2/s	1.954	-

The experiments were carried out with varied gas flow rates and liquid flow rates. The liquid flow rate varied from 5 to 700 mL/h, and the gas flow rate varied from 50 to 2000 mL/h. Dimensionless numbers in slug flow regime, including Reynolds number, Capillary number and Sherwood number, are listed in Table 3-3.

Table 3-3 Dimensionless number in slug flow regime

Dimensionless number		Value range
Reynolds number of the liquid phase	$Re_L = \frac{D_h j_L \rho_L}{\mu_L}$	30.7 - 306.6
Reynolds number of the gas phase	$Re_G = \frac{D_h j_G \rho_G}{\mu_G}$	3.7 - 73.9
Reynolds number in a cell	$Re_T = \frac{D_h j_T \rho_L}{\mu_L}$	611.6 - 924.1
Capillary number of the gas phase	$Ca_B = \frac{\mu_L j_B}{\sigma_L}$	0.0028 - 0.024
Sherwood number	$Sh = \frac{k_L D_h}{D_{dif}}$	84.9 - 1017.3

Paper ii (square microchannel):

As for the research on square microchannel, the dispersed phase was CO_2 and N_2 and the continuous phase is de-ionized water. The physical properties at 20.5 ± 0.5 °C of them are shown in Table 3-4.

Table 3-4 Physical properties at 20.5 ± 0.5 ◦C

			water	CO_2	N_2
Density	ρ	kg/m^3	998.2	1.797	1.138
Viscosity	μ	mPa·s	1.005	0.0150	0.0179
Surface tension	σ	N/m	0.0728	/	/
Diffusivity	D_{dif}	10^{-9} m^2/s	1.954	/	/

The experiments were carried out with varied gas flow rates and liquid flow rates. The liquid flow rate varied from 2 to 1400 mL/h, and the gas flow rate varied from 100 to 2000 mL/h. Dimensionless numbers in slug flow regime, including Reynolds number, Schmidt number, Capillary number and Sherwood number, are listed in Table 3-5.

Table 3-5 Dimensionless numbers in slug flow regime

Dimensionless number		Value range
Reynolds number of bubble	$Re_B = \frac{\rho_G j_B D_H}{\mu_G}$	23 - 153
Reynolds number of gas phase	$Re_G = \frac{\rho_G j_G D_H}{\mu_G}$	6 - 66
Reynolds number of liquid phase	$Re_L = \frac{\rho_L j_L D_H}{\mu_L}$	92 - 460
Schmidt number of liquid phase	$Sc_L = \frac{\mu_L}{\rho_L D_{dif}}$	515
Capillary number of both phases	$Ca_T = \frac{\mu_L j_T}{\sigma}$	0.0032 - 0.0234
Sherwood number	$Sh = \frac{k_L D_h}{D_{dif}}$	167 - 1149

Paper iii (gas-liquid two phase displacement in porous media):

As for the research on gas-liquid displacement in porous media, the mixtures of deionized water and glycerol solution with concentrations varying from 0 - 80%, were used as the defending phase. The air was used as invading phase to displace liquid. Their properties at 20.5 ± 0.5 °C are listed in Table 3-6.

Table 3-6 Physical properties at 20.5 ± 0.5 °C ("Gly" represents glycerol solution).

		Defending phase				Invading phase
		water	40% Gly	60% Gly	80% Gly	air
Density, ρ	(kg/m^3)	998.2	1099	1154	1209	1.138
Viscosity, μ	(mPa·s)	1.01	3.72	10.8	60.1	0.0179
Surface tension, σ	(N/m)	0.0728	0.0695	0.0676	0.0653	-
Contact angle, θ	±4 °	38.3°	39.7°	38.4°	39.2°	-

The viscosity ratio M between the invading phase and defending phase was calculated. Based on different concentrations of glycerol solution, $\mathrm{Log_{10}M}$ varied from -1.75 to 3.53 as shown in Table 3-7. Capillary number Ca was calculated and $\mathrm{Log_{10}Ca}$ varied from -8.17 to -4.17 when the gas flow rate varied from 0.1-1000 mL/h.

Table 3-7 Dimensionless numbers

Gas flow rate (mL/h)	0.1	1	10	100	1000
Capillary number $\mathrm{Log_{10}Ca} = \mathrm{Log_{10}}\left(\frac{\mu_i U_i}{\sigma_d}\right)$	-8.17	-7.17	-6.17	-5.17	-4.17
Concentration of glycerol solution	**water**	**40%**	**60%**	**80%**	
Viscosity ratio $\mathrm{Log_{10}M} = \mathrm{Log_{10}}\left(\frac{\mu_i}{\mu_d}\right)$	-1.75	-2.32	-2.78	-3.53	

Paper iv (gas invasion into multi-fluids in porous media):

As for the research on gas invasion into multi-fluids in porous media, N_2, Hexane and 60 wt.% Glycerol solution were used as gas phase (G) with extremely low viscosity, low viscous liquid phase (LL), and high viscous liquid phase (HL), respectively. Their properties at 20.5 ± 0.5 °C are listed in Table 3-8.

Table 3-8 Physical properties at 20.5 ± 0.5 °C ("Gly" represents glycerol solution).

		Gly60 (HL)	Hexane (LL)	N_2 (G)
Density, ρ	(kg/m^3)	1154	654.8	1.138
Viscosity, μ	(mPa·s)	10.8	0.312	0.0179
Surface tension to N_2, σ	(N/m)	0.0676	0.0185	-
Surface tension to Hexane, σ	(N/m)	0.0510	-	-
Contact angle, θ		38.4° ± 4 °	0°	-

The various gas invasion scenarios of HL, LL, and their co-existing multi-fluid system were conducted by changing fluid injection sequence, including G → LL, G → (HL → LL), G → HL, and G → (LL → HL) displacements. The injection rate was varied from 20 to 2000 mL/h.

Paper v (cyclic injection in porous media):

As for the research on cyclic injection in porous media. The N_2 and deionized water were used as gas phase (G) and liquid phase (L), which are alternately injected into the porous medium to achieve cyclic injection. Their properties at 20.5 ± 0.5 °C are listed in Table 3-9.

Table 3-9 Physical properties at 20.5 ± 0.5 °C

	Deionized water	N_2
Density, ρ (kg/m^3)	998.2	1.138
Viscosity, μ (mPa·s)	1.01	0.0179
Surface tension, σ (N/m)	0.0728	/
Contact angle, θ	75°	/

During waterflooding process, the corresponding capillary number Ca ranging from 2.57E-06 to 1.46E-05 with the viscosity ratio (liquid to gas) M equal to 56.4. During drainage process, capillary number Ca ranging from 4.55E-08 to 2.58E-07 with the viscosity ratio (gas to liquid) M equal to 0.0177.

3.4 Image and data processing method in microchannel

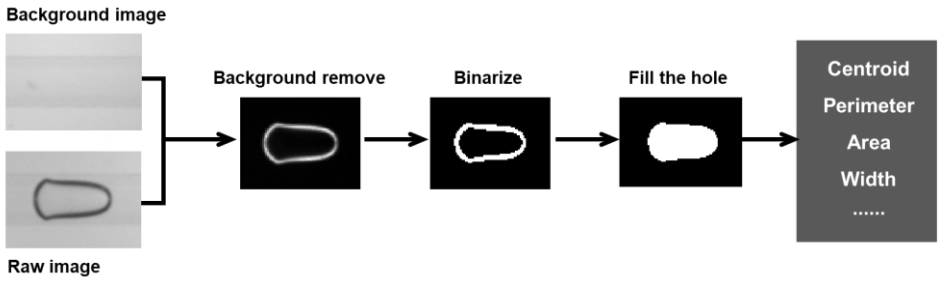

Figure 3-6 Image processing procedure for bubble in microchannels.

Since the images were recorded in a high-speed mode, several thousands of frames were available to provide details of the process of bubbles flowing through the channel. These images can be processed in batches by developed in-house MATLAB code. The image process procedure was shown in Figure 3-6. Firstly, liquid was injected into microchannel without the gas phase. About 1000 frames of background images were captured in this condition. The background image was generated by averaging the gray levels of each pixel of these images. Then all the raw images of the case were divided by the background image pixel by pixel to remove the background. In the processed images, the gray level of the pixel in the center of the bubble and the outer region is close to 1. But that within the boundary of the bubble is much higher than 1. By setting threshold value of 1.2, the images were binarized. After filling the holes of inner area of bubble, the binarized bubble shape was obtained. Based on binarized bubble shape, bubble characteristics, such as the centroid, perimeter, area, width, etc., were measured by MATLAB algorithm. The velocity of the bubble j_B was obtained by fitting the position of the centroid of the bubble over time. Finally, the bubble volume V_B and interfacial area between gas and liquid phase A_B were calculated, which will be detailed in the following subsection.

3.4.1 Calculation of bubble 3D volume V_B and interfacial area A_B in rectangular microchannel based on 2D projection

The image of 3D bubble captured by camera is a 2D projection. But the bubble volume and interface area should be determined in 3D. It is necessary to convert 2D projection to 3D volume. The theoretical model based on the principle of interfacial energy minimization is implemented for the conversion[98]:

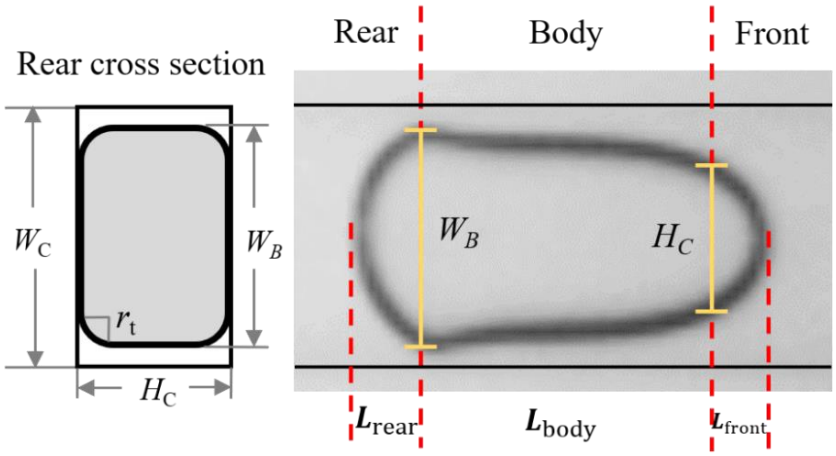

Figure 3-7 Schematic diagram of bubble (The front of bubble is divided at the position where the width is smaller than H_C (300 μm)).

As shown in Figure 3-7, the cross section is characterized by width W_B, depth H_B and curvature radius r_t at the channel corner. According to the model, the curvature radius r_t, the cross-sectional area A_{bd} and the perimeter P_{bd} are calculated by:

$$r_t = \frac{H_B + W_B - \sqrt{{H_B}^2 + (\pi - 2) H_B W_B + {W_B}^2}}{4 - \pi} \approx \left(\frac{2}{H_B} + \frac{2}{W_B}\right)^{-1} \tag{3-1}$$

$$A_{bd} = H_B W_B - (4 - \pi) {r_t}^2 \tag{3-2}$$

$$P_{bd} = 2(H_B + W_B - 4r_t + \pi r_t) \tag{3-3}$$

The length of the bubble rear is assumed as $L_{rear} = W_B/2$. The film on the depth side is negligible, which means $H_B = H_C$. As shown in Figure 3-7, bubble is divided into three parts: rear cap, front cap and body, and the volumes of these are calculated separately, as is described below.

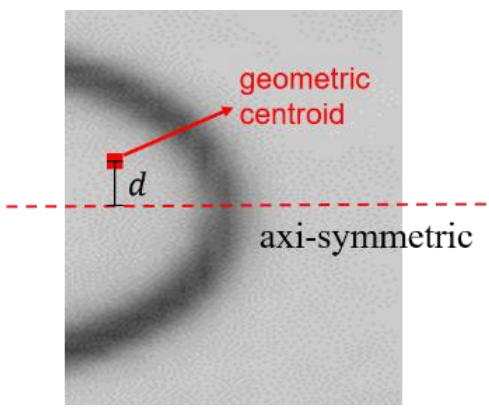

Figure 3-8 Schematic diagram of the front cap.

As for the front cap (Figure 3-8), the width is smaller than H_C (300 μm) and it can therefore be considered as a revolution body [99]. The volume and interface area are then calculated based on the Pappus theorem:

$$V_{front} = S_{front} \times 2\pi d \tag{3-4}$$

$$A_{front} = L_{boundary} \times 2\pi d \tag{3-5}$$

Here, d is the distance between the centroid of the upper front cap and the revolution axis. S_{front} is the projected area of the upper front cap. $L_{boundary}$ is the length of the boundary of the upper front cap.

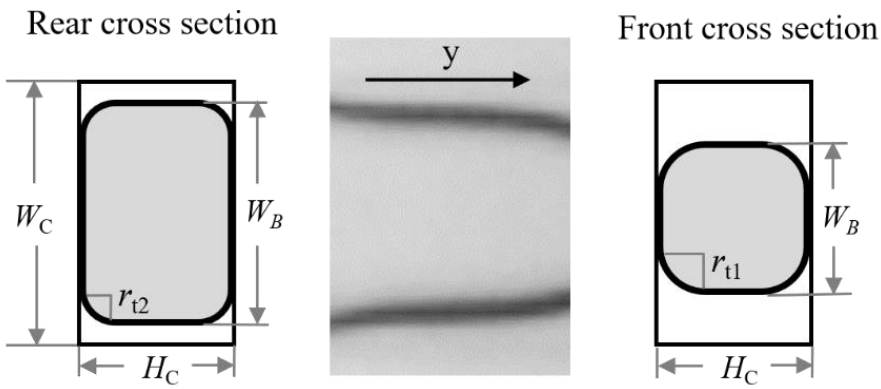

Figure 3-9 Schematic diagram of body.

For the body part (Figure 3-9), It is assumed that the cross-section area $A_b(y)$ and the perimeter $P_b(y)$ decrease linearly from rear to front, and these are calculated as:

$$A_b(y) = \frac{A_{bd1} - A_{bd2}}{L_{body}} y + A_{bd2} \tag{3-6}$$

$$P_b(y) = \frac{P_{bd1} - P_{bd2}}{L_{body}} y + P_{bd2} \tag{3-7}$$

Based on Eq. (3-6) and Eq. (3-7), and the cross-section area A_{bd1}, A_{bd2} and perimeter P_{bd1}, P_{bd2} for the front cap side and rear cap side are calculated. Therefore, the volume and interface area of the body can be measured as the integrals:

$$V_{body} = \int_0^{L_{body}} A_b(y)\, dy = \frac{1}{2} L_{body}(A_{bd1} + A_{bd2}) \tag{3-8}$$

$$A_{body} = \int_0^{L_{body}} P_b(y)\, dy = \frac{1}{2} L_{body}(P_{bd1} + P_{bd2}) \tag{3-9}$$

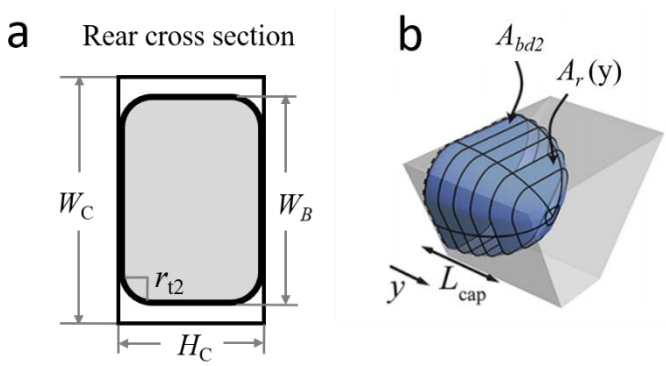

Figure 3-10 Schematic diagram of rear cap: (a) rear cross section; (b) shape of the cap [98] (Reprint by permission from the publisher).

As for the rear cap (Figure 3-10), it is assumed that the cross-section area $A_r(y)$ decreases monotonically from $A_r(y) = A_{bd2}$ at $y = 0$ to $A_r(y) = 0$ at $y = L_{rear}$. Similarly, the perimeter monotonically decreases from $P_r(y) = P_{bd2}$ at $y = 0$ to $P_r(y) = 0$ at $y = L_{rear}$ [98].

$$A_r(y) = A_{bd2}\left(1 - \frac{y^2}{{L_{rear}}^2}\right) \tag{3-10}$$

$$P_r(y) = P_{bd2}\left(1 - \frac{y^2}{{L_{rear}}^2}\right) \tag{3-11}$$

So, the volume V_{rear} and interface area A_{rear} of the rear cap can be calculated as:

$$V_{rear} = \int_0^{L_{rear}} A_r(y)\, dy = \frac{2}{3} L_{rear} A_{bd2} \tag{3-12}$$

$$A_{rear} = \int_0^{L_{rear}} P_r(y)\, dy = \frac{2}{3} L_{rear} P_{bd2} \tag{3-13}$$

The volume and cross-section area of the bubble can be measured by sum:

$$V_B = V_{rear} + V_{body} + V_{front} \tag{3-14}$$

$$A_B = A_{rear} + A_{body} + A_{front} \tag{3-15}$$

A mass centroid is obtained based on the calculated bubble volume, which is distinct from the 2D image centroid. Then bubble velocity is obtained by fitting the position of mass centroid with time.

3.4.2 Calculation of deformed bubble in square microchannel based on 3D slicing method

Based on the slicing method [100], the 3D shape of symmetric bubbles and deformed bubbles in square microchannel were reconstructed. As shown in Figure 3-11 (a, b), the bubble was sliced along the streamwise direction z_B according to the pixels. $W_B(z_B)$ was estimated by in-house codes of MATLAB at each slice. When bubbles flow in a square microchannel, the

corner flow and liquid film flow between bubble surface and wall will occur. According to the principle of interfacial energy minimization [98], the cross-section of a slice is assumed to involve a square and four circular arcs with the radius r at the corners when width of bubble $W_B(z_B) > 2r$, as shown in Figure 3-11 (c). When the gas/liquid interface contacts the walls of microchannel, the width of body film δ is equal to zero. The stress boundary condition at the interface can be simplified to $\nabla \cdot \mathbf{n} = \frac{1}{r}$ [101], where $\mathbf{n}$ is the unit vector normal to the interface in the outward direction. After integrating and using the Gauss theorem, r can be calculated by the ratio of the area and perimeter of cross-section of microchannel:

$$r = \frac{A_C}{P_C} = \frac{{W_C}^2 + (\pi - 4)r^2}{4W_C + (2\pi - 8)r} \tag{3-16}$$

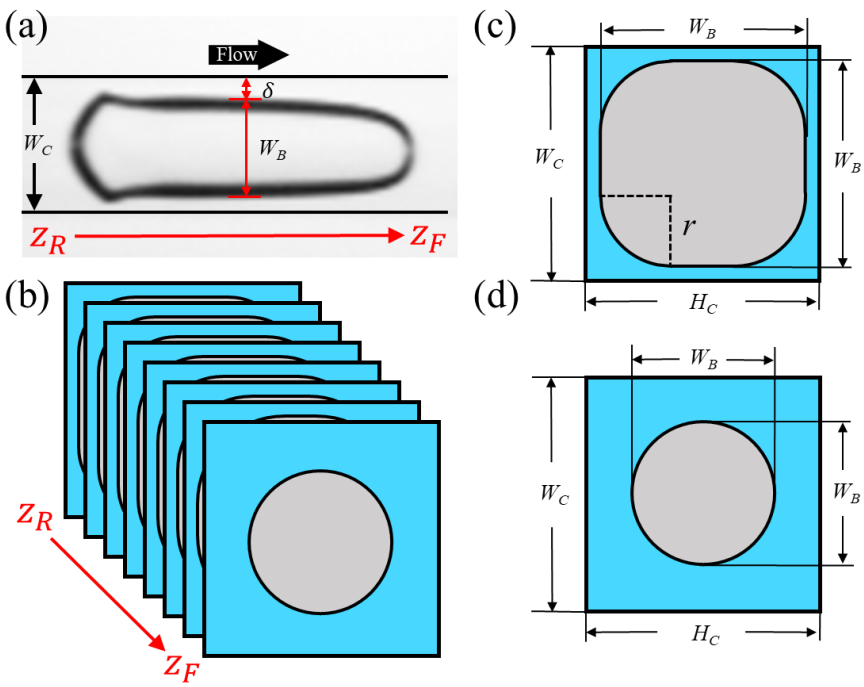

Figure 3-11 Physical image captured by the high-speed camera; (b) Schematic diagram of bubble slices from bubble rear z_R to bubble front z_F; (c) Schematic diagram of cross-section of the slice when $W_B(z_B) > 2r$; (d) Schematic diagram of cross-section of the slice when $W_B(z_B) \leq 2r$.

Here, P_C and A_C are the cross-section perimeter and cross-section area when the width of body film δ is equal to zero. The width of channel W_C is equal to 600 μm. So, r is calculated

as 159 μm according to Eq. (3-16). When $W_B(z_B) > 2r$, the width of bubble $W_B(z_B)$ varies but r doesn't change, because r only depends on the channel aspect ratio. When the slice is located near bubble front or rear, W_B reduces. When $W_B(z_B) = 2r$, the cross-section becomes a circle with the diameter W_B as shown in Figure 3-11 (d). When $W_B(z_B) < 2r$, the diameter W_B of circle becomes smaller as the slice further closes to bubble front or rear. Therefore, the cross-sectional area $A(z_B)$ and the interfacial perimeter $P(z_B)$ of the bubble slices at each z_B position can be calculated as:

$$A(z_B) = \begin{cases} W_B^2(z_B) + (\pi - 4)r^2, & W_B(z_B) > 2r \\ \frac{\pi}{4} W_B^2(z_B), & W_B(z_B) \leq 2r \end{cases} \tag{3-17}$$

$$P(z_B) = \begin{cases} 4W_B(z_B) + (2\pi - 8)r, & W_B(z_B) > 2r \\ \pi W_B(z_B), & W_B(z_B) \leq 2r \end{cases} \tag{3-18}$$

The volume V_B and interfacial area A_B of a bubble are calculated by superimposing all slices N_z:

$$V_B = \int_{z_R}^{z_F} A(z_B) dz_B \approx \Delta z \sum_{i=1}^{N_z} A(z_{B,i}) \tag{3-19}$$

$$A_B = \int_{z_R}^{z_F} P(z_B) dz_B \approx \Delta z \sum_{i=1}^{N_z} P(z_{B,i}) \tag{3-20}$$

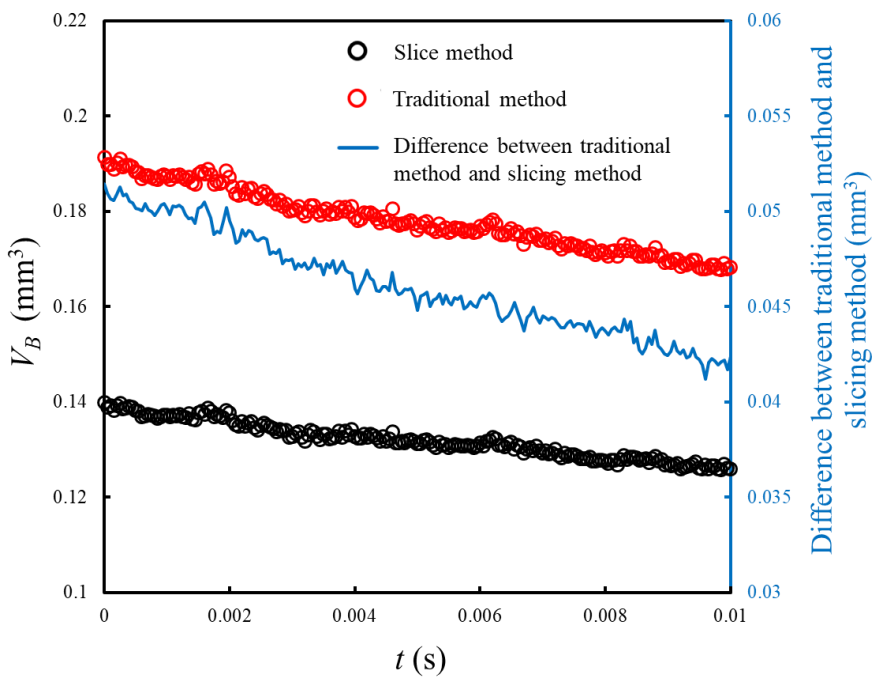

Figure 3-12 Comparison between the traditional method and the slicing method.

In the traditional method, the rear and cap of the bubble are considered as two hemispheres. The volume is calculated by volume formula of sphere. Besides, the width of bubble body W_B is assumed to be constant. Therefore, traditional bubble volume calculation is as below:

$$(V_B)_{tra} = \left[\overline{W_B}^2 + (\pi - 4)r^2\right]\left(L_B - \overline{W_B}\right) + \frac{1}{6}\pi\overline{W_B}^3 \tag{3-21}$$

Here, L_B is the length of the bubble. Because of the varying width of deformed bubble body, an average value $\overline{W_B}$ was used. Figure 3-12 confirms that the bubble volume is overestimated by using the traditional method. The volume difference between the traditional method and the slicing method is from 0.0185 to 0.043 mm^3, which is approximately 35% of V_B obtained by the slicing method. So, the slicing method is more feasible to estimate the volume of the deformed bubble.

3.4.3 Principle of mass transfer coefficient calculation

As mentioned above, the mass transfer coefficient of CO_2 bubbles can be calculated by using the two-film theory and ideal gas law:

$$k_L = -\frac{1}{RTA_B(C_{L,i}-C_{L,b})}\frac{d(P_{CO_2}V_{CO_2})}{dt} = -\frac{1}{RTA_B(C_{L,i}-C_{L,b})}\left(P_{CO_2}\frac{dV_{CO_2}}{dt} + V_{CO_2}\frac{dP_{CO_2}}{dt}\right) \tag{3-22}$$

Here, $\frac{dP_{CO_2}}{dt}$ of CO_2 bubbles is difficult to measure. To measure it, N_2 was used to repeat all the cases of CO_2 experiments. Because N_2 has no mass transfer with water, we can have:

$$\frac{d(P_{N_2}V_{N_2})}{dt} = V_{N_2}\frac{dP_{N_2}}{dt} + P_{N_2}\frac{dV_{N_2}}{dt} = \frac{dM_{N_2}}{dt}RT = 0 \tag{3-23}$$

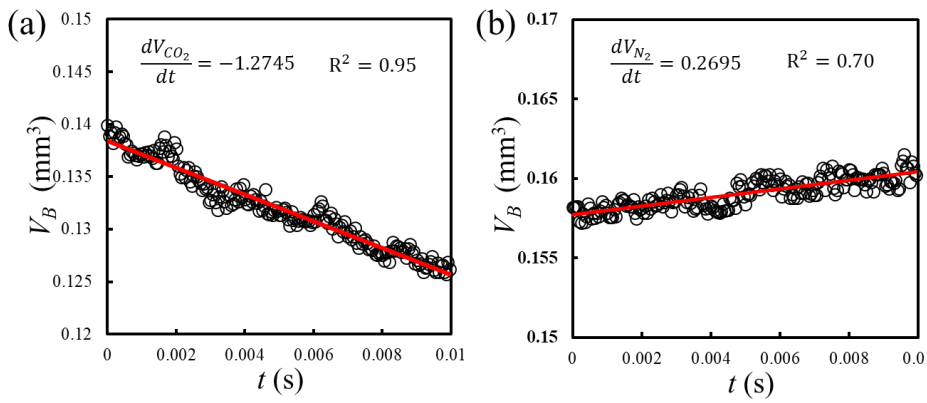

Figure 3-13 (a) Volume changes of a CO_2 bubble with time and the fitting curve; (b) Volume changes of a N_2 bubble with time and the fitting curve.

Based on the bubble volume calculation method above, the volumes of CO_2 and N_2 bubbles V_{CO_2} and V_{N_2} can be measured. Figure 3-13 shows the volume change of CO_2 and N_2 bubbles flowing through the microchannel at the same case (same gas and liquid volume flow rate).

The CO_2 bubble volume decreased over time due to the mass transfer from bubble to liquid, while N_2 bubble volume over time due to pressure drop. Actually, the volume of CO_2 also expands because of pressure drop, but it is offset by the volume reduction caused by mass transfer. As shown in Figure 3-13, the initial volumes of CO_2 and N_2 bubbles are close, because the gas injection volume controlled by flow meter are same in the same case. Therefore, $\frac{V_{CO_2}}{V_{N_2}}$ is approximately 1. By ignoring the effect of bubble volume change on pressure drop, the pressure drops of CO_2 and N_2 bubbles flowing through microchannels are identical at a same flow rate, which is equal to:

$$\Delta P = P - P_{atmosphere} \tag{3-24}$$

Therefore, the pressure in microchannel P is also the same as for CO_2 and N_2 bubbles, which means $\frac{dP_{N_2}}{dt} = \frac{dP_{CO_2}}{dt}$ and $\frac{P_{N_2}}{P_{CO_2}} = 1$. Eq. (3-23) is substituted into Eq. (3-22):

$$k_L = -\frac{P_{CO_2}}{RTA_B(C_{L,i}-C_{L,b})}\left(\frac{dV_{CO_2}}{dt} - \frac{dV_{N_2}}{dt}\right) \tag{3-25}$$

According to ideal gas law, the volume expansion of bubbles resulting from pressure drop is independent of gas species. Therefore, it is reasonable to use N_2 volume expansion to correct the CO_2 volume expansion resulting from pressure drop. $\left(\frac{dV_{CO_2}}{dt} - \frac{dV_{N_2}}{dt}\right)$ represents the volume reduction purely resulting from mass transfer.

Because the mass transfer rate of CO_2 is relatively low, the concentration at the bulk $C_{L,b}$ is much lower compared with the concentration at the interface $C_{L,i}$. So, $C_{L,b}$ can be neglected. Henry's law describes the solubility of gases absorbed by water:

$$\frac{H}{RT} = \frac{C_{L,i}}{P_{CO_2}} \tag{3-26}$$

Here, H is the Henry constant in dimensionless form, which is 0.827 for CO_2 at 298 K [102]. Substituting the Eq. (3-26) into Eq. (3-25), the mass transfer coefficient k_L can be calculated as:

$$k_L = -\frac{1}{A_B H}\left(\frac{dV_{CO_2}}{dt} - \frac{dV_{N_2}}{dt}\right) \tag{3-27}$$

After linear fitting, $\frac{dV_{CO_2}}{dt}$ and $\frac{dV_{N_2}}{dt}$ can be obtained as shown in Figure 3-13. Based on the above calculation method of the interfacial area A_B of CO_2 bubble, we can obtain mass transfer coefficient k_L finally.

3.5 Image and data processing method in porous media

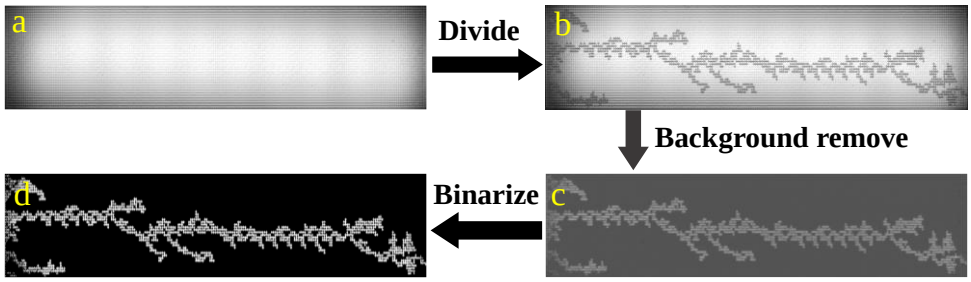

Figure 3-14 Procedures of image processing of fingering pattern in porous media: (a) background image of porous patterns before gas invasion; (b) raw image of gas invasion; (c) greyscale image after subtracting background; (d) binarized image.

Image processing procedures of fingering pattern in porous media are similar to the procedure for the bubble in a single microchannel. The procedure was achieved by an in-house code in MATLAB. As shown in Figure 3-14 (a), about 1000 frames of background images were captured to average the gray value pixel by pixel. Then, all the raw images of cases were divided by the average background image to remove the background as shown in Figure 3-14 (c). The processed image was binarized as shown in Figure 3-14 (d). Finally, the quantification study was conducted by popular algorithms and LBM simulation, including invading velocity, saturation, finger complexity, topology connectivity and permeability.

3.5.1 Invasion velocity

Invasion velocity is also an important parameter that affects the cost in subsurface storage and extraction application. In this study, velocity of finger cap U_{cap} was measured by fitting the slope of the curve of fingering cap position versus time. In addition, breakthrough time T_B was calculated based on the frames of high-speed camera, which is the elapsed time for the finger cap to invade from the inlet to outlet. After breakthrough, the invasion in viscosity regime and crossover regimes will continue until the invasion phase cannot overcome the resistance to invade new areas. At this time, the invading area reaches maximum, a condition that we define as a steady state. Steady state time T_S also was counted from the inlet to steady state.

3.5.2 Saturations

The displacement coefficient is an important indicator in subsurface storage and extraction application, which can be characterized by phase saturation. The saturations S of each phase are calculated:

$$S = \frac{A}{L_{total} W_{total} \varphi} \tag{3-28}$$

Here, A is the invaded area of each phase. L_{total} and W_{total} are the length and width of the porous domain, respectively. φ is the porosity of the porous domain.

3.5.3 Finger complexity:

Finger complexity can be quantified by fractal dimension FD, which was measured by box-counting method [103]. By fitting the curve of boxes number N occupied by the pattern as a function of the resolution scale Δ (size of box), the FD at the breakthrough moment and the steady state can be calculated:

$$FD = \lim_{\Delta \to \infty} \frac{log(N)}{log(\Delta)} \tag{3-29}$$

3.5.4 Topology connectivity

To characterize the fluid connectivity of fingering pattern in porous media, a topological invariant, i.e., Euler number (or Euler characteristic) χ [90, 104]was calculated from the family of Betti numbers:

$$\chi = \beta_0 - \beta_1 + \beta_2 \tag{3-30}$$

β_0, β_1, and β_2 correspond to the number of disconnected fluid elements, “handles” or loops within each fluid elements, and isolated voids or cavities in the fluid elements, respectively. As for our two-dimensional micromodel, the value of β_2 is equal to 0.

3.5.5 Permeability

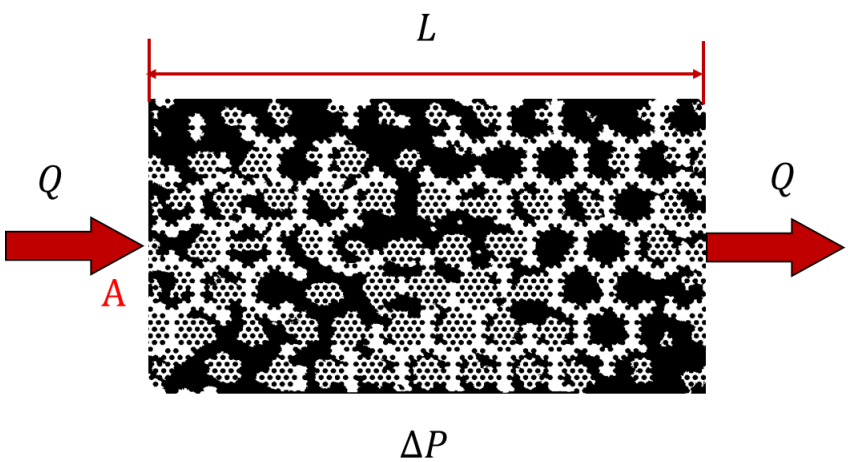

Figure 3-15 Schematic diagram of Lattice Boltzmann method (LBM)

To access the ease with which the invading phase flows through the porous media, the absolute permeability k_{abs} was measured by LBM simulation based on the binarized image

of the invasion pattern at the steady state as shown in Figure 3-15. By applying the pressure difference ΔP between the inlet and outlet, water will flow through the invaded channels (white pixels). Employing the flow rate Q obtained from the simulation results, the absolute permeability can be calculated based on Darcy's law [105]:

$$k_{\text{abs}} = \frac{\mu L Q}{A \Delta P} \tag{3-31}$$

Here, μ is the viscosity of water, A is the cross-sectional area of porous media inlet. Then, the relative permeability k^* of the invading phase was calculated:

$$k^* = \frac{K_{\text{abs}}}{K_{\text{abs,100\%}}} \tag{3-32}$$

Here, $k_{\text{abs,100\%}}$ is the maximum absolute permeability when the porous media is initially 100% saturated with gas.

3.6 Uncertainty analysis

Table 3-10 Uncertainties.

Parameters	Uncertainty	Remarks
Thermocouple T	± 0.2 °C	-
Surface roughness Ra	± 2.0%	-
Contact angle	± 5.0 °	-
Bubble width W_B, cell length L_C	± 0.0196 mm (± 1 pixel)	-
Bubble velocity j_B	Max. ± 2%	-
Cross-sectional area $A(z_B)$ in each slice	Max. ± 0.02 mm^2	$\delta A(z_B) = 2W_B \delta W_B$
Interfacial perimeter $P(z_B)$ in each slice	Max. ± 0.08 mm	$\delta P(z_B) = 4\delta W_B$
Bubble volume V_B	Max. ± 0.005 mm^3	$\delta V_B = \left[\Delta z^2 \sum_{i=1}^{N_z} \delta A\left(z_{B,i}\right)^2\right]^{1/2}$

Interfacial area A_B	Max. ± 0.02 mm^2	$\delta A_B = \left[\Delta z^2 \sum_{i=1}^{N_z} \delta P\left(z_{B,i}\right)^2\right]^{1/2}$
Overall mass transfer coefficient k_L	Max. ± 5%	$\frac{\delta k_L}{k_L} = \left[\left(\frac{\delta A_B}{A_B}\right)^2 + \left(\frac{\delta \frac{dV_B}{dt}}{\frac{dV_B}{dt}}\right)^2\right]^{1/2}$
Volume of cell V_C	Max. ± 0.007 mm^3	$\delta V_C = W_C^2\ \delta L_C$
Specific interfacial area a	Max. ± 1%	$\frac{\delta a}{a} = \left[\left(\frac{\delta A_B}{A_B}\right)^2 + \left(\frac{\delta V_C}{V_C}\right)^2\right]^{1/2}$
Volumetric mass transfer coefficient $k_L a$	Max. ± 5%	$\frac{\delta k_L a}{k_L a} = \left[\left(\frac{\delta k_L}{k_L}\right)^2 + \left(\frac{\delta a}{a}\right)^2\right]^{1/2}$
Velocity of finger cap U_{cap}	Max. ± 2%	-
Breakthrough time T_B	Max. ± 3%	-
Fingering area A	Max. ± 5%	-
Saturations S	Max. ± 5%	$\delta S = \frac{\delta A}{LW\varphi}$
Fractal dimension FD	Max. ± 7%	$\frac{\delta FD}{FD} = \left[\left(\frac{1}{N \ln 10} \frac{\delta N}{\log(N)}\right)^2 + \left(\frac{1}{\Delta \ln 10} \frac{\delta \Delta}{\log(\Delta)}\right)^2\right]^{1/2}$

Euler number χ	Max. ± 7%	$\delta\chi = [(\delta\beta_0)^2 + (\delta\beta_1)^2]^{1/2}$
Absolute permeability k_{abs}	Max. ± 6%	$\frac{\delta\chi}{\chi} = \left[\left(\frac{\delta Q}{Q}\right)^2 + \left(\frac{\delta \Delta P}{\Delta P}\right)^2\right]^{1/2}$

CHAPTER 4

Results and Discussion

This chapter shows an overview and summary of the most important results and discussion of five papers. It is divided into two sections i.e., mass transfer of gas-liquid flow in single rectangular and square microchannels as well as gas-liquid multiphase displacement in porous media with microchannel network.

4.1 Single straight microchannels

This section consists of the result and discussion of **papers I and ii** on mass transfer of gas-liquid flow in single rectangular microchannel as well as mass transfer and modeling of deformed bubbles in square microchannel, respectively.

4.1.1 Flow pattern map

Figure 4-1 shows the flow pattern map in a square microchannel. By varying the superficial gas and liquid velocity, the flow regime can cover bubbly flow, slug flow and annular flow. The flow pattern map was compared with boundaries defined by Triplett et al.[12], Akbar et al.[13] and Niu et al.[14]. The transition line in this study between slug and annular-slug flow is located at a lower superficial gas velocity compared with that obtained by Triplett et al.[12], while it is in great agreement with that of Akbar et al. [13] and Niu et al.[14]. As the same as Niu et al.[14], the present map didn't distinguish the slug-annular and annular flow. The transition line between bubbly and slug flow didn't coincide with that proposed by Triplett et al.[12] and Niu et al.[14]. The deviation partly results from the larger size of circular microchannel and different junction configurations used in their study as shown in Figure 2-2.

Due to its relatively stable and preferable characteristics for mass transfer, only gas-liquid flow in the slug flow regime was investigated in the following study. In order to be more intuitive, the gas phase in slug flow is named bubble.

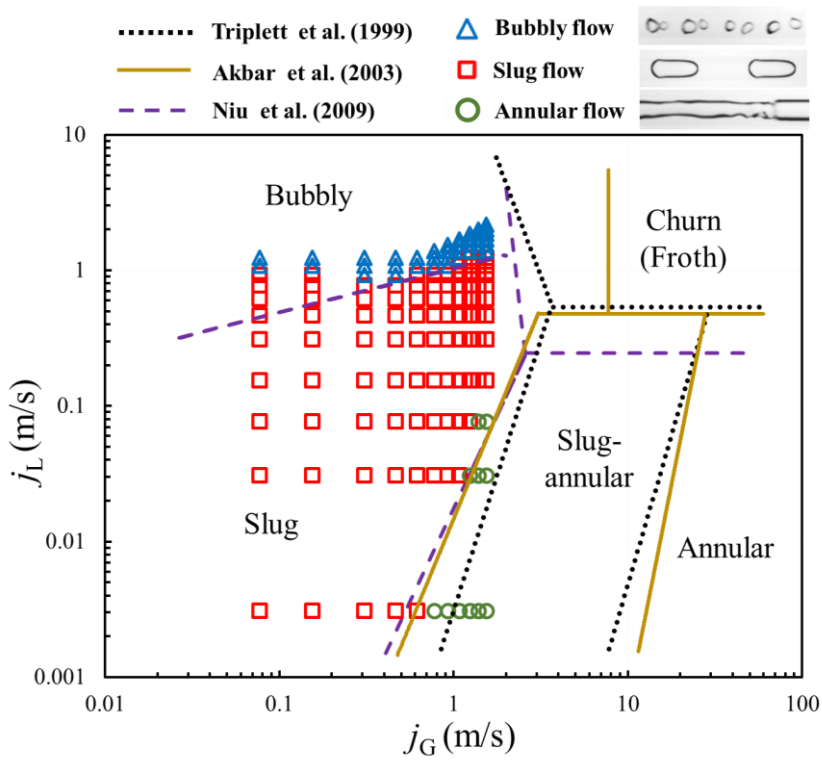

Figure 4-1 Flow pattern map of square microchannel. (superficial gas and liquid velocity are calculated by j_G and j_L).

4.1.2 Scaling law

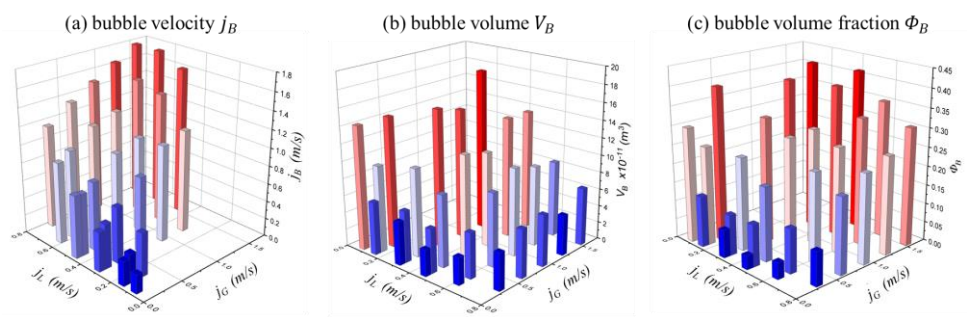

Figure 4-2 bar charts of parameters of rectangular microchannel against superficial gas and liquid velocities: (a) bubble velocity j_B; (b) bubble volume V_B; (c) bubble volume fraction Φ_B.

Figure 4-2 demonstrates the effect of superficial gas and liquid velocities on bubble velocity and volume. As shown in Figure 4-2 (a), the bubble velocity shows remarkably positive relationships with superficial gas and liquid velocities. As shown in Figure 4-2 (b), the bubble volume is larger at the higher superficial gas velocity and lower superficial liquid velocity. The reason is related to the time for bubble to grow and break up. Bubble volume fraction in Figure 4-2 (c) shows the same trend.

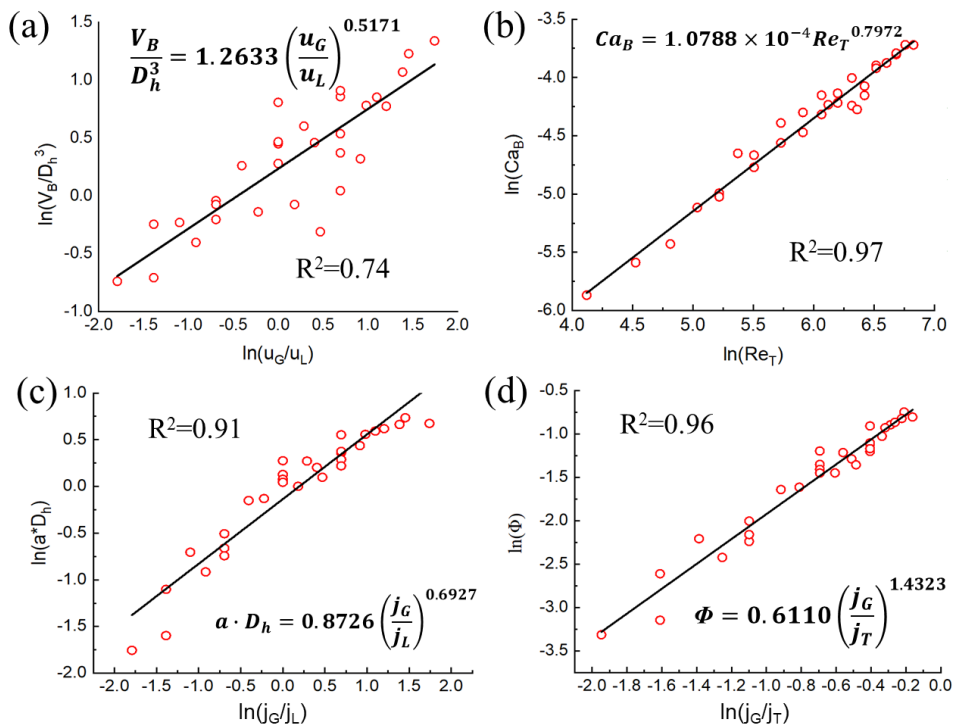

Figure 4-3 Correlations of hydrodynamics of the bubbles in rectangular microchannel.

$$\frac{V_B}{D_h^3} = 1.2633\left(\frac{j_G}{j_L}\right)^{0.5171} \tag{4-1}$$

$$Ca_B = 1.0788 \times 10^{-4} Re_T^{0.7972} \tag{4-2}$$

$$a \cdot D_h = 0.8726\left(\frac{j_G}{j_L}\right)^{0.6927} \tag{4-3}$$

$$\Phi_B = 0.6110\left(\frac{j_G}{j_T}\right)^{1.4323} \tag{4-4}$$

Figure 4-3 shows the scaling lows about the bubble properties and dimensionless numbers in rectangular microchannel, including bubble volume V_B, superficial gas and liquid velocity

j_G and j_L, total superficial velocity j_T, Capillary number Ca_B, Reynolds number Re_T, specific interfacial area a and bubble volume fraction Φ_B. The correlations were fitted as shown in Eq. (4-1,2,3,4). They all show a good fitting result. The coefficient of determination R^2 is higher than 0.7.

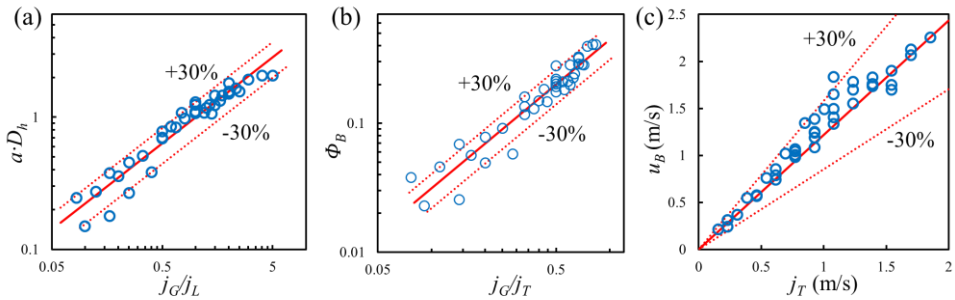

Figure 4-4 Correlations of square microchannel: (a) specific interfacial area; (b) bubble volume fraction; (c) bubble velocity.

$$a \cdot D_h = \left(\frac{j_G}{j_L}\right)^{0.6530} \tag{4-5}$$

$$\Phi_B = 0.4470 \left(\frac{j_G}{j_T}\right)^{1.1560} \tag{4-6}$$

$$j_B = 1.2175 \cdot j_T \tag{4-7}$$

In order to explore the influence of cross section on the scaling laws, scaling lows in a square microchannel were fitted, by using bubble properties including the specific interfacial area a, bubble volume fraction Φ_B, superficial gas and liquid velocity j_G and j_L, bubble velocity j_B and total superficial velocity j_T. Figure 4-4 shows a good fitting result for all correlations. All the points are almost within $\pm 30\%$ error bound.

By comparing the scaling laws of square and rectangular microchannels, the coefficients in correlations of $a \cdot D_h$ and Φ_B are very close. Therefore, these correlations have a significant universality. All in all, these scaling laws can provide the guidance for the design of micro-reactors. They played an important role in the estimation of important parameters in micro-reactors, such as the ratio of the feed volume of reactant streams and residence time.

4.1.3 Mass transfer coefficient

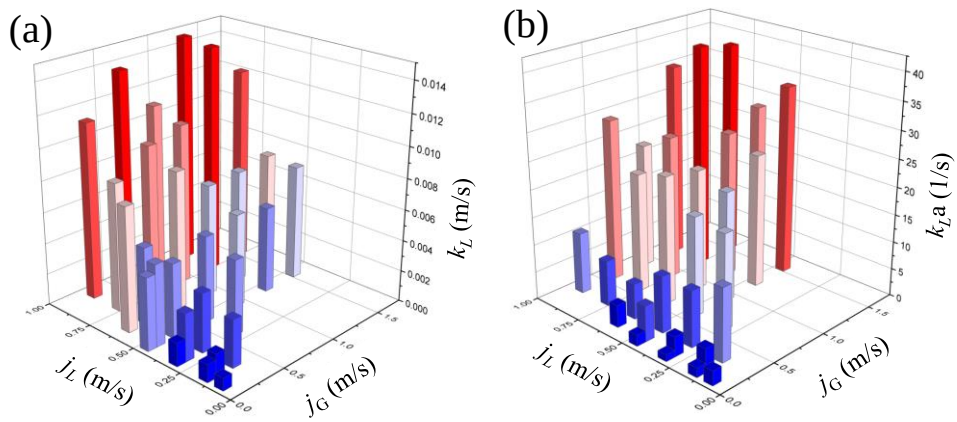

Figure 4-5 Effect of the superficial gas and liquid velocity on mass transfer in rectangular microchannel (a) mass transfer coefficient k_L; (b) volumetric mass transfer coefficient $k_L a$.

By calculating bubble volume and interface area, the mass transfer from gas phase to liquid phase in rectangular and square microchannels was estimated. Figure 4-5 shows the effect of superficial gas and liquid velocity on mass transfer coefficients in rectangular microchannel. Mass transfer coefficient k_L and volumetric mass transfer coefficient $k_L a$ both show a significant positive relationship with superficial gas and liquid velocity. It is because the higher superficial gas and liquid velocities, the stronger internal circulation and the renewal of liquid at the interface.

Many correlations based on dimensionless numbers were developed to predict dimensionless number $Sh \cdot a \cdot D_h = k_L a D_h^2 / D_{dif}$. $Sh \cdot a \cdot D_h$ can consider simultaneously the important effect on mass transfer process, including mass transfer coefficients, diffusion rate, specific interfacial area of bubble and size of microchannel. Figure 4-6 shows the comparison between the present measured values and the predicted values from typical correlations of $Sh \cdot a \cdot D_h$ in literature of rectangular microchannel [106-109] and square microchannel [107, 110, 111]. Like this study, these correlations were all developed based on CO_2 absorption in water. However, the correlations all underestimated the mass transfer in the rectangular microchannel. In the square microchannel, the correlations overestimate the measured values in square microchannel except Yue et al. [107]. The correlation proposed by Yue et al. [107] can properly predict our measured data, because of similar hydraulic diameters of square microchannel. The differences in hydraulic diameter, type of junction and shape of the cross-section may be the reason of deviation. Therefore, it is necessary to develop new correlations that can accurately predict mass transfer coefficient in rectangular and square microchannels.

(a) Rectangular microchannel

	Geometry of cross section	Hydraulic diameter D_h	Cross section	Junction
Yue at el. 2006	1000 × 500 μm	667μm	rectangular	Y-shaped
Li at el.	400 × 600 μm	480μm	rectangular	T-shaped
Yue at el. 2009	400 × 400 μm	400μm	square	Y-shaped
Niu at el.	1000μm	1000μm	circular	T-shaped

(b) Square microchannel

	Geometry of cross section	Hydraulic diameter D_h	Cross section	Junction
Yue et al.	1000 × 500 μm	667 μm	rectangular	Y-shaped
Yao et al.	600 × 300 μm	400 μm	rectangular	T-shaped
Bercic and Pintar	D_C: 1500, 2500, 3100 μm	1500,2500,3100 μm	circular	/
Van Baten et al.	D_C: 1500, 2000, 3000 μm	1500,2000,3000 μm	circular	/

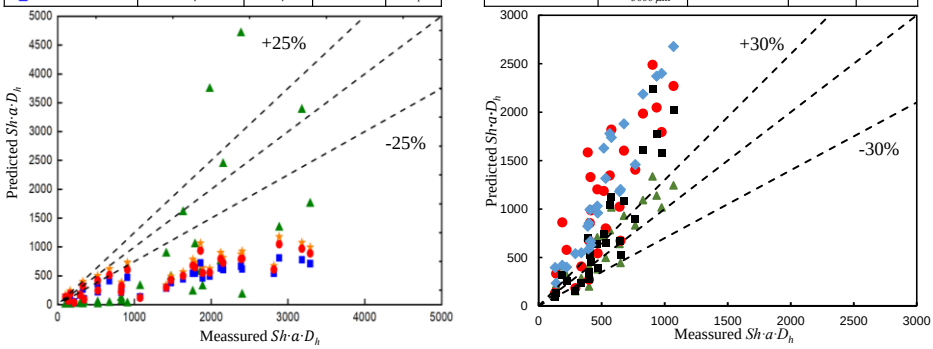

Figure 4-6 (a) Comparison between the measured $Sh \cdot a \cdot D_h$ in rectangular microchannel and predictions of pure empirical correlations in literatures [106-109]; (b) Comparison between the experimental $Sh \cdot a \cdot D_h$ in square microchannel and predictions from empirical correlations [107, 110, 111] and the theoretical model [112](Eq. (4-13)) in the literature.

(a) Rectangular microchannel

(b) Square microchannel

	Geometry of cross section	Hydraulic diameter D_h	Cross section	Junction
Yao et al.	300 × 600 μm	400 μm	rectangular	T-shaped
Yue et al.	1000 × 500 μm	667 μm	rectangular	Y-shaped
Zhang et al.	400 × 400 μm	400 μm	square	T-shaped
This study	600 × 600μm	600 μm	square	cross

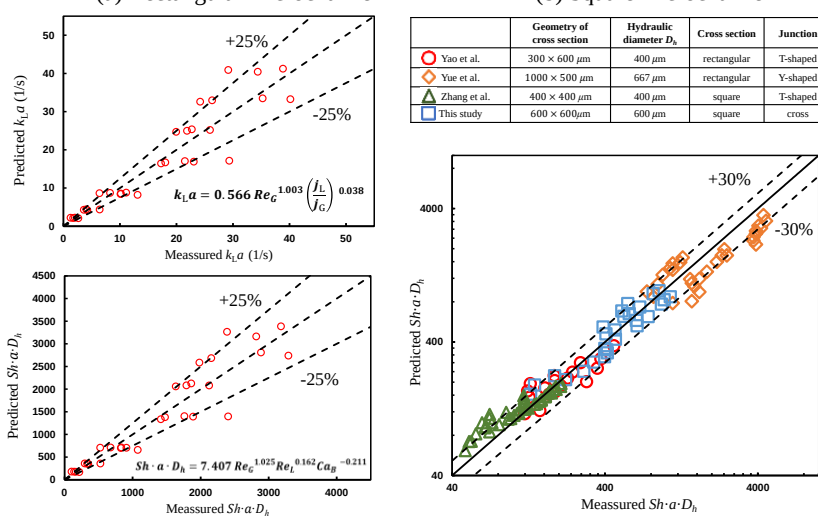

Figure 4-7 (a) The comparison between measured values from rectangular microchannel and predictions of fitted empirical correlations Eq. (4-8) and Eq. (4-9). (b) Comparison between the measured $Sh \cdot a \cdot D_h$ (based on the data from square microchannel and literature data[19, 23, 107]) and the predicted $Sh \cdot a \cdot D_h$ from fitted empirical correlation Eq. (4-10).

As for rectangular microchannel,

$$k_L a = 0.566\, {Re_G}^{1.003} \left(\frac{j_L}{j_G}\right)^{0.038} \tag{4-8}$$

$$Sh \cdot a \cdot D_h = 7.407\, {Re_G}^{1.025} {Re_L}^{0.162} {Ca_B}^{-0.211} \tag{4-9}$$

As for square microchannel,

$$Sh \cdot a \cdot D_h = 0.9566 \cdot {Re_G}^{0.5698} \cdot {Re_L}^{0.2296} \cdot {Sc_L}^{0.5} \tag{4-10}$$

By using the experiment data in rectangular microchannel, the correlations of $k_L a$ and $Sh \cdot a \cdot D_h$ were fitted based on dimensionless numbers as shown in Eq. (4-8) and Eq. (4-9).

Figure 4-7 (a) shows the comparison between measured values and predicted values of correlations Eq. (4-8) and Eq. (4-9). The correlations both have good predicted performance, and they can predict the mass transfer within ± 25% error band. It should be noted that the index of dimensionless numbers is close to 0 except Re_G, which means that the mass transfer process may be mainly related to gas flow conditions. This sparked our interest in continuing to explore mass transfer in square microchannel.

A correlation Eq. (4-10) based on dimensionless numbers was fitted to predict $Sh \cdot a \cdot D_h$ in square microchannel. Figure 4-7 (b) shows that blue square points locate within ± 30% error bound, confirming that the correlation Eq. (4-10) can precisely predict the measured values in square microchannel. Besides, the correlation Eq. (4-10) also shows excellent prediction performance to predict the measured $Sh \cdot a \cdot D_h$ in literature[19, 23, 107], even though channel geometry, shape of cross-section and junction are different. The error is also within a ± 30% bound.

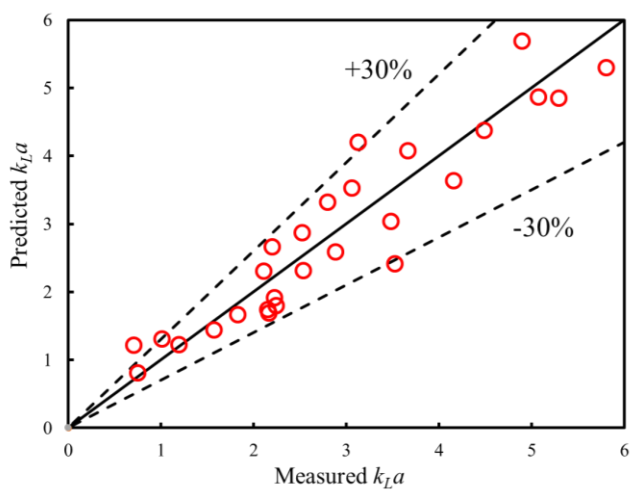

Figure 4-8 Comparison between the measured $k_L a$ from square microchannel and the predicted $k_L a$ from semi-theoretical model Eq. (4-14).

Although empirical correlation Eq. (4-10) shows a good prediction performance, there are still restrictions due to the limited database. In contrast, theoretical models are more convincing. A fundamental model based on two contributions to the mass transfer process was developed by Van Baten et al.[112]. The contributions consist of mass transfer between the film and the bubble body and mass transfer between two bubble caps and the liquid plug. Penetration theory[113] was used to derive the model:

$$(k_L a)_{film} = 2\sqrt{\frac{D_{dif} j_G}{\pi L_f}} \cdot \frac{4L_f}{L_C D_h} \tag{4-11}$$

$$(k_L a)_{caps} = 2\frac{\sqrt{2}}{\pi}\sqrt{\frac{D_{dif} j_G}{D_h}} \cdot \frac{4}{L_C} \tag{4-12}$$

Here, D_{dif} is the diffusivity, L_f is the length of the film, D_h is the hydraulic diameter. After validation of CFD simulation, the total volumetric mass transfer coefficient $k_L a$ is calculated:

$$k_L a = (k_L a)_{film} + (k_L a)_{caps} \tag{4-13}$$

However, Figure 4-6 (b) shows that the predicted values by Eq. (4-13) deviated from the measured values. It is because deformed bubbles in the square channel caused the non-uniform film and asymmetrical caps. It is not accurate to directly apply the sum of the contributions for deformed bubbles. According to bubble visualizations in Figure 2-6, the ratio of the length of liquid phase and gas phase, i.e. $\frac{L_L}{L_G}$, can characterize the degree of bubble deformation. Therefore, a new semi-theoretical model was proposed by including $\frac{L_L}{L_G}$:

$$k_L a = 0.3469 \cdot (k_L a)_{caps} + 0.4806 \cdot (k_L a)_{film} \cdot \left(\frac{L_L}{L_G}\right)^{0.5012} \tag{4-14}$$

As shown in Figure 4-8, the new semi-theoretical model Eq. (4-14) can predict the measured $k_L a$ accurately within ± 30% error bound.

4.2 Porous media with microchannel networks

This section consists of the result and discussion of **papers iii, iv, v** on gas-liquid two-phase displacement emphasis on fingering evolution after breakthrough, viscous-dependent multifluid invasion behavior during three-phase displacement, and hysteresis effect during cyclic injection in hierarchical porous media, respectively.

4.2.1 Displacement pattern morphology

Displacement pattern during gas-liquid two-phase displacement

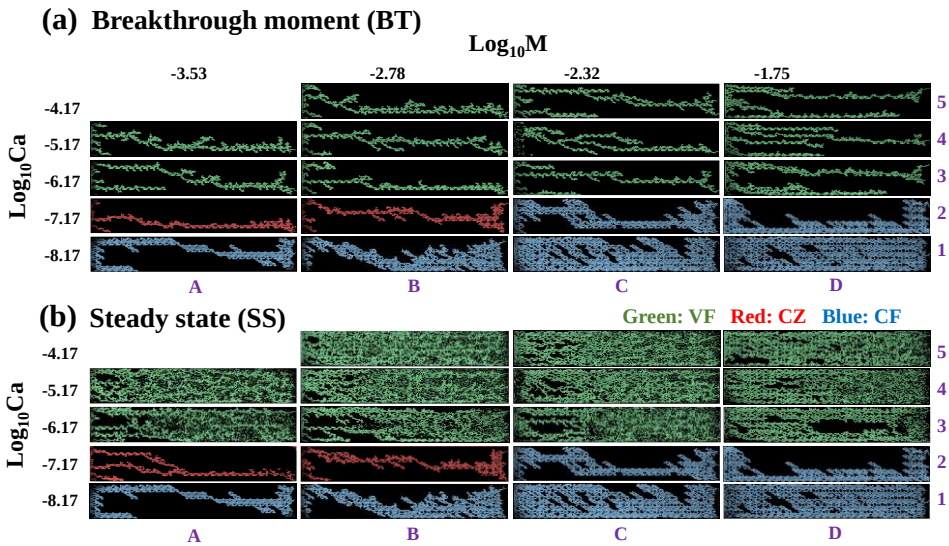

Figure 4-9 Fingering pattern visualization of gas-liquid displacement at the breakthrough moment and at the steady state for three different flow regions as a function of the viscosity ratio $Log_{10}M$ and the capillary number $Log_{10}Ca$: (a) morphologies at the breakthrough moment when the finger cap reaches the outlet; (b) morphologies at the steady state when invasion area no longer increases.

In this section, I turn our insight to the flow in porous media. Gas-liquid two-phase displacement is an essential process in geological extraction and storage applications and is also a popular research topic in the study of porous media. Due to interface instability, the fingering pattern occur in the domain. Figure 4-9 shows the fingering morphologies of gas-liquid displacement at the BT (breakthrough moment) and SS (steady state) in different flow regions. For convenience, the symbols with letters and numbers (A1, A2…D4, D5) were used to represent the different cases. The cases include the regions of viscous fingering (VF), capillary fingering (CF) and crossover zone (CZ):

In viscous fingering (VF) region, the viscous force mainly controls the fingering displacement process, which allows gas to invade forward rather than lateral. A narrow and straight flow path is generated in the green patterns of Figure 4-9 (a). After breakthrough, the gas will continue to invade liquid. At steady state, almost all the liquid phase is displaced as shown in Figure 4-9 (b).

Capillary fingering (CF) region is located in the region with lower $Log_{10}Ca$ and higher $Log_{10}M$ as shown in the blue patterns of Figure 4-9 (a). Due to the lower velocity of the invading phase and the lower viscosity of the defending phase, the viscous force can be neglected and the capillary force mainly controls the displacement process. The gas will mainly spread lateral channels, and thus a wide finger forms. After breakthrough, invasion stops in capillary fingering regime as shown in the blue patterns of Figure 4-9 (b).

In crossover zone (CZ) region, the finger is similar to the finger in VF region. But compared with VF, the finger in CZ region will only expand less area after breakthrough, as shown in the red patterns of Figure 4-9. It is because the capillary force and viscous force jointly control fingering displacement process.

Displacement pattern during three-phase displacement

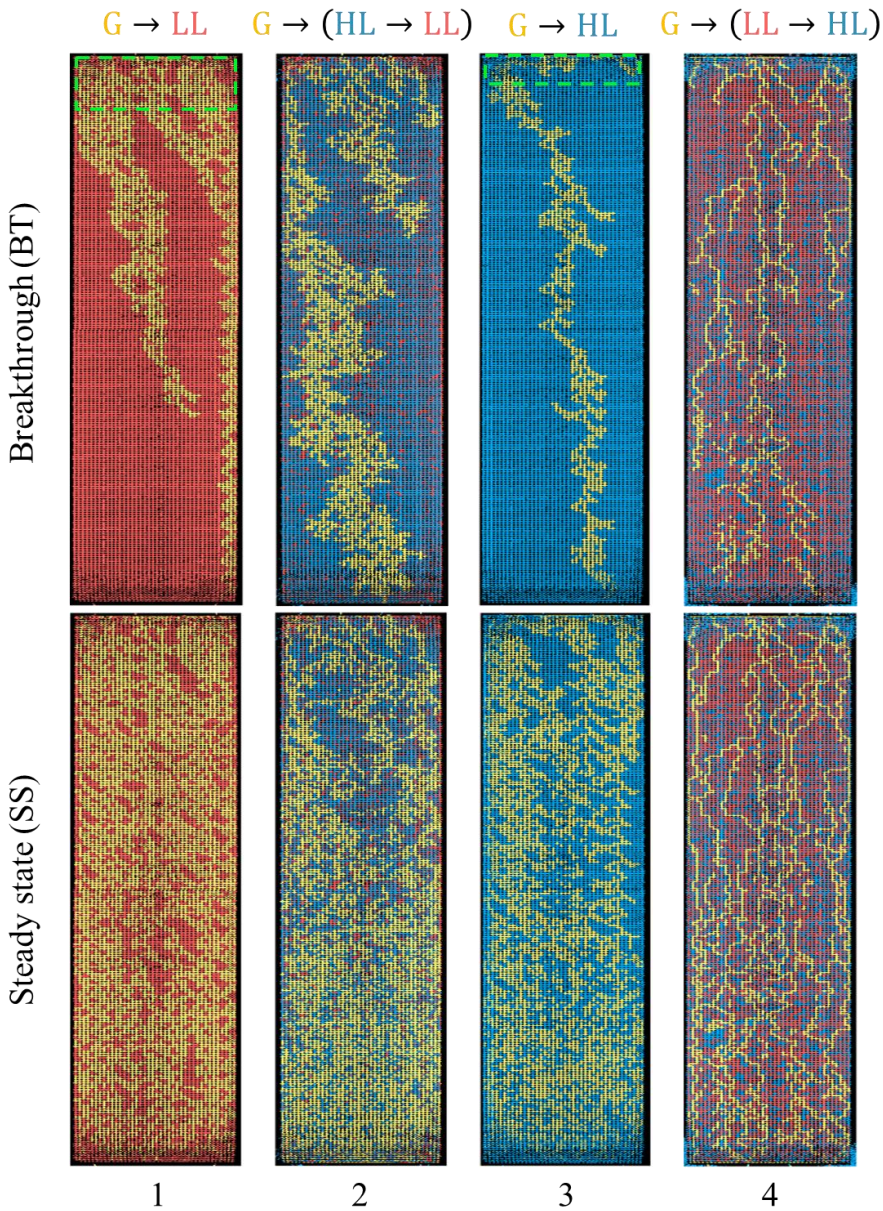

Figure 4-10 Visualization of gas-invading fingers under different multiphase scenarios at breakthrough moment and steady state at 20 mL/h flow rate (G, LL and HL are painted golden, red and blue colors, respectively. BT and SS represent breakthrough moment and steady state. Invasion direction is from up to down.)

In numerous geological gas sequestration processes, the invading gas (G) is commonly introduced into aquifers that host multiple fluids, e.g. depleted oil reservoirs where the extraction process has nearly concluded after water/brine flooding. In order to investigate the invading behavior under different multiphase invasion scenarios, i.e. G→LL, G→(HL→LL), G→HL, and G→(LL→HL), the fingering patterns at BT (breakthrough moment) and SS (steady state) with a 20 mL/h flow rate of invading phase were compared in Figure 4-10. Here, HL and LL represent high and low viscous liquids, respectively. The gas invasion observed during G→(HL→LL) displacement displays a pattern similar to the G→L two-phase displacement. Notably, a distinctive and previously undocumented yarn-like pattern is discerned in the G→(LL→HL) displacement experiment, as illustrated in BT4 in Figure 4-10. It is crucial to highlight that the defending phase in both instances comprises a co-existing LL and HL mixture, but the gas invading patterns in the G→(HL→LL) and G→(LL→HL) processes are entirely different. This discrepancy is attributed to the distinct occupation sequences of LL and HL within the pore spaces, potentially resulting in varying liquid distribution and saturation. Prior investigations [114] have shown the significant sensitivity of the invading phase's fingering pattern to the initial liquid distribution within the porous domain. To delve into the underlying reasons, an analysis of invading dynamics is presented in subsequent sections.

Displacement pattern during cycle gas-liquid invasion in hierarchical porous media

In applications of underground hydrogen storage, the operational processes typically involve temporary storage and later-on extraction (use), corresponding to cyclic displacement of gas injection (drainage) and withdrawal (waterflooding). In the context of cyclic gas-liquid injection, the displacement pattern is influenced by the porous structure. Therefore, the displacement patterns at the steady state of each cycle between uniform and hierarchical porous media was compared, as shown in Figure 4-11. In the initial cycle (Cycle 0), liquid injection was employed to displace the gas that originally occupied the pore space. Given the significantly higher viscosity of the liquid compared to that of the gas and the weak wettability of the solid surface, the displacement process was favorable, and the interface remained stable. Figure 4-11 demonstrates that in **U-model**, the liquid effectively displaced most of the gas phase, leaving only a few small gas ganglia distributed along the streamwise direction. However, in **H-model**, large gas clusters persisted in the 2nd-order pore space, despite the clear displacement of the 1st-order pore space by the liquid. Following the initial waterflooding process, the first drainage process occurred in Cycle 1, as depicted in the gas invasion in Figure 4-11. Due to the lower viscous ratio, the interface became unstable in **U-model**, leading to a fingering pattern and the substantial uninvaded areas. In **H-model**, the gas invasion pattern of Cycle 1 indicated a preference for invading the 1st-order structure. As the number of injection cycles in **U-model** increases, both gas and liquid invasion progressively stabilizes into a singular pathway. This stabilization is accompanied by the suppression of bypass expansion, culminating in the formation of a thin and straight invaded path, as shown in light colors in cycle 4 of Figure 4-11. However, in the 1st-order structure of **H-model**, the invasion pattern fails to stabilize into a consistent pathway. In the 2nd-order

structure, the displacement pattern remains relatively constant after the water invasion in cycle 0, suggesting that gas becomes entrapped and lacks the ability to mobilize.

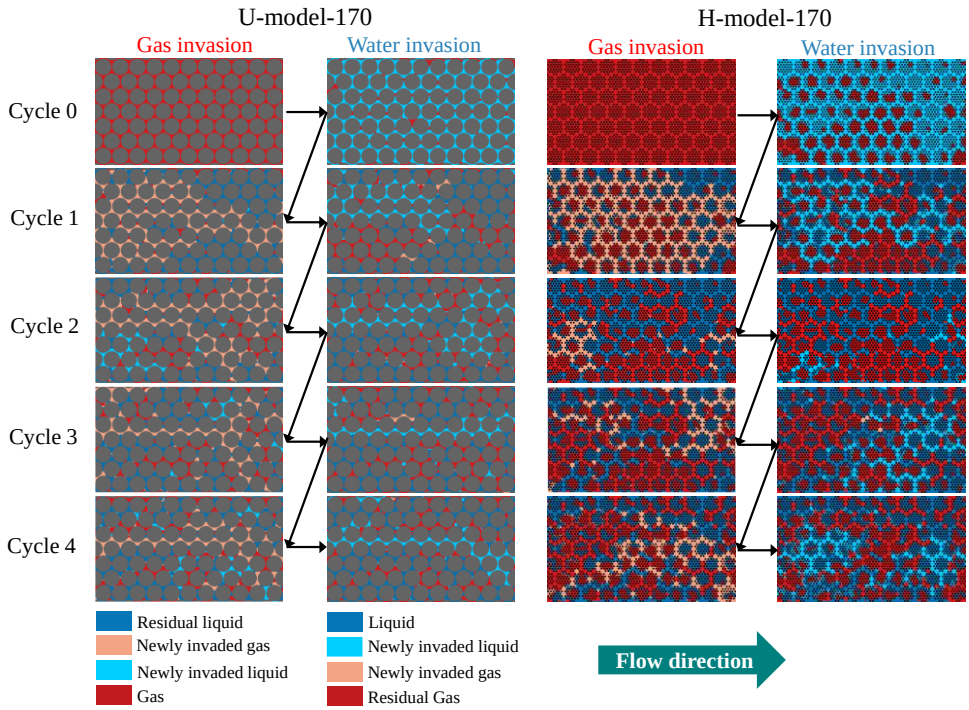

Figure 4-11 Comparison of fingering pattern of cyclic gas-liquid injection between uniform and hierarchical structures at flow rate of 170 mL/h. (Blue and red represent the liquid and gas phase, respectively. The light blue and light red represent the newly invaded liquid and gas, respectively. ‘‘**U-model**’’ and ‘‘**H-model**’’ represent uniform and hierarchical porous media, respectively.)

4.2.2 Comparative quantification

Quantitative study of gas-liquid two-phase displacement

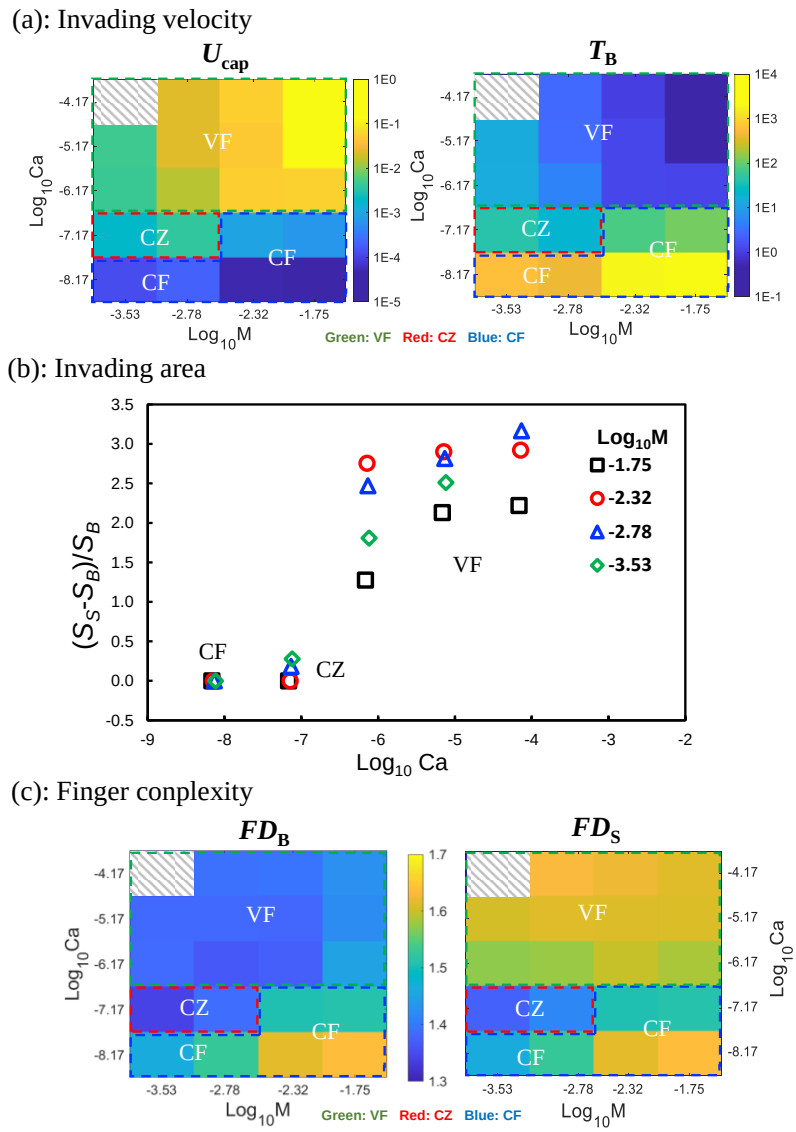

Figure 4-12 (a) Maps of the finger cap velocity U_{cap} and breakthrough time T_B; (b) Saturation gain ratio $(S_S - S_B)/S_B$; (c) Maps of fractal dimension FD_B at the breakthrough moment and FD_S at the steady state. (VF region: green dotted rectangle; CZ region: red dotted rectangle; CF region: blue dotted rectangle).

The detailed quantitative analysis of the two-phase fingering displacement was conducted. Firstly, Figure 4-12 (a) shows velocity map of the finger cap U_{cap} and breakthrough time T_B with the function of $Log_{10}Ca$ and $Log_{10}M$. U_{cap} is fastest and T_B is shortest in VF region. Invasion velocity has a positive relationship with $Log_{10}Ca$ and $Log_{10}M$ in VF region because of higher gas flow rate and weaker resistance. The minimum time to breakthrough is only 0.48 s at the highest $Log_{10}M$ and $Log_{10}Ca$. T_B in the CF region is about 4 orders of magnitude higher than the shortest time, which demonstrates that the displacement region have a significant impact on the invading velocity. Then, the saturation was measured to characterize the invasion area. By measuring fingering area A_{BT} at the breakthrough moment and A_{SS} at the steady state, the saturation gain ratio $(S_S - S_B)/S_B$ can be calculated, which is the normalized increment of saturation from the breakthrough moment to steady state. As shown in Figure 4-12 (b), the saturation gain ratio is equal to zero in CF region because gas stops expanding new area after breakthrough. The gas with a low flow rate can only flow along the previously formed invading paths after breakthrough. Saturation gain ratio increases to ranges from 1.0 to 3.0 in the VF region, because gas continues to invade new area after breakthrough. The invaded area increases significantly after breakthrough in the VF region. It is validated by previous experimental observations of fingering morphologies in Figure 4-9. Finally, fractal dimension FD was used to quantify finger complexity as shown in Figure 4-12 (c). FD grows approximately from 1.4 to 1.6 in the VF region after breakthrough. As the invaded area expands after breakthrough, new finger branches form and thus the fingers become more fractal and complex. The comparative quantitative research before and after breakthrough provides potential guidance on how to achieve high displacement efficiency in a relatively short time and whether it is cost-effective to continue gas injection after breakthroughs in industrial applications.

Quantitative study of three-phase displacement

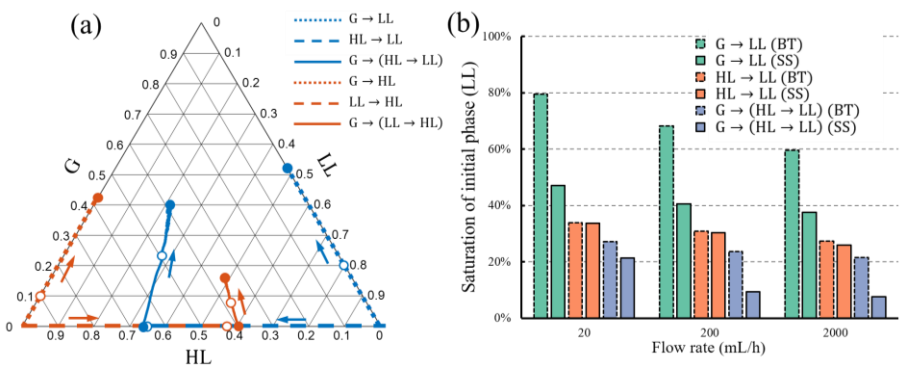

Figure 4-13 (a) Three-phase diagram illustrating saturation evolution of each phase under different multiphase scenarios at 20 mL/h flow rate (The solid and hollow dots represent the breakthrough moment and the steady state, respectively.). (b) Saturation of initial phase (LL) after the two-phase and three-phase displacement at different flow rates of invading phase.

Then three phase displacement process was quantified and compared with the two-phase displacement process. Figure 4-13 (a) demonstrates the displacement scenarios categorized into two distinct parts based on the different initial liquid phases, represented by the various colors of the curves. Here, the displacement efficiency is defined as $1 - S_{\text{initial}}$ (S_{initial} is the saturation of the initial phase. The initial phase's low saturation indicates high displacement efficiency. Figure 4-13 (a) illustrates that alternating to gas phase injection G→(L→L) after the L→L displacement reached steady state further enhances displacement efficiency. In other words, introducing a third phase after saturation limit is reached in L→L displacement can surpass this limit and significantly increase efficiency. In summary, displacement efficiency follows the order G→(L→L) > L→L > G→L. The three-phase displacement, specifically in G→(HL→LL), exhibits the lowest saturation of the initial phase, with residue saturation approaching 20%. The superiority of G→(L→L) in achieving the highest displacement efficiency suggests substantial potential for enhancing subsurface extraction through three-phase flow.

Figure 4-13 (b) presents the influence of invading flow rate on residue saturations of the initial phase (LL). No matter flow rate varies, the order of displacement efficiency remains the same. Notably, when employing the lowest flow rate (20 mL/h) in G→(HL→LL) displacement, the residue saturation of LL remains considerably lower compared to the use of the highest flow rate (2000 mL/h) in G→LL and HL→LL displacements. The same trend appears in G→(LL→HL) displacement. This finding underscores the superiority of three-phase displacement efficiency, even at low injection rates, despite the usual expectation that increasing injection rates would reduce LL residue. The advantage of a slow injection rate lies in the reduced energy consumption of pumping equipment, offering substantial economic benefits for practical geo-applications.

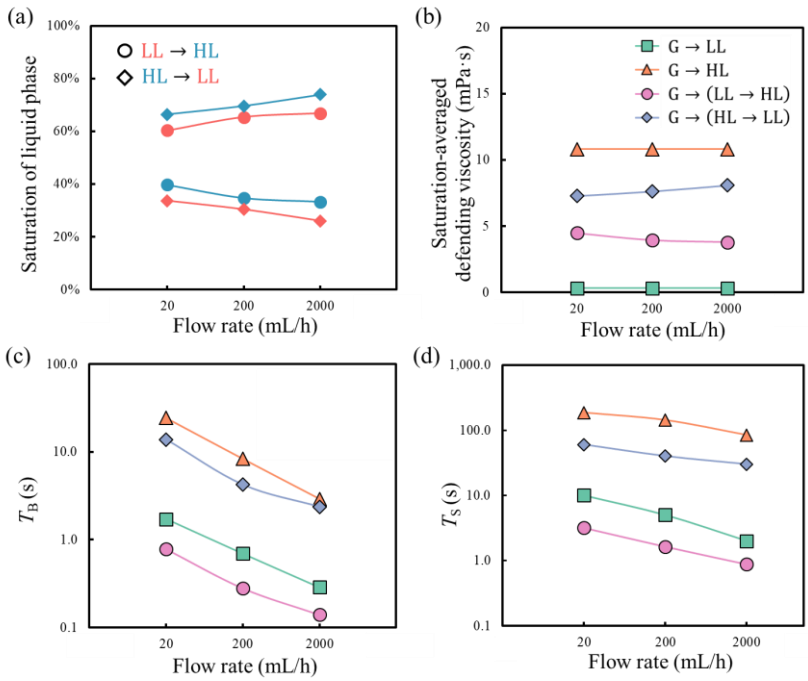

Figure 4-14 Saturation of liquid phase when L→L displacement reaches steady state. (b) Saturation-averaged defending viscosity in G→(L→L) displacement after L-L displacement reaches equilibrium μ_{ave}. (c,d) Breakthrough time T_{B} and steady-state time T_{S} of gas invading in the case of G→L and G→(L→L).

The gas invasion behavior in three phase displacement is located in the region of phase diagram that is dominated by viscous effect. Therefore, the viscosity of the defending phase was initially examined. In the case of the co-existing HL and LL multi-fluids, the saturation of each liquid phase before gas invasion is depicted in Figure 4-14 (a). Subsequently, the saturation-averaged defending viscosity, denoted as μ_{ave}, was calculated based on the liquid saturation after L-L displacement reach steady state:

$$\mu_{ave} = S_{HL}\mu_{HL} + S_{LL}\mu_{LL} \tag{4-15}$$

Due to distinct invading phases during the L→L displacement, Figure 4-14 (b) illustrates a divergent trend in μ_{ave} for G→(HL→LL) and G→(LL→HL) as the flow rate increases. Obviously, the μ_{ave} in G→(HL→LL) is higher than that in G→(LL→HL).

From the gas invasion experiments, the breakthrough time T_{B} and steady-state time T_{S} were also measured as shown in Figure 4-14 (c,d). Often, higher viscosity implies greater resistance from the defending phase during gas invasion, lead to the longer invasion time. However, the gas invasion time does not strictly adhere to the order of averaged viscosities of the defending phase. The T_{B} and T_{S} of G→LL are not the fastest even though its viscosity of defending

phase is the lowest. Surprisingly, G→(LL→HL) displays the shortest invading time, counterintuitively accelerated after encountering the high-viscosity phase HL before gas injection. This intriguing observation suggests that the unique yarn-like finger structure may hold the key to unraveling the mysteries behind the ultra-fast invading speed of G→(LL→HL). The mechanism behind the formation of yarn-like finger will be discussed in later section.

Quantitative study of cycle gas-liquid invasion in hierarchical porous media

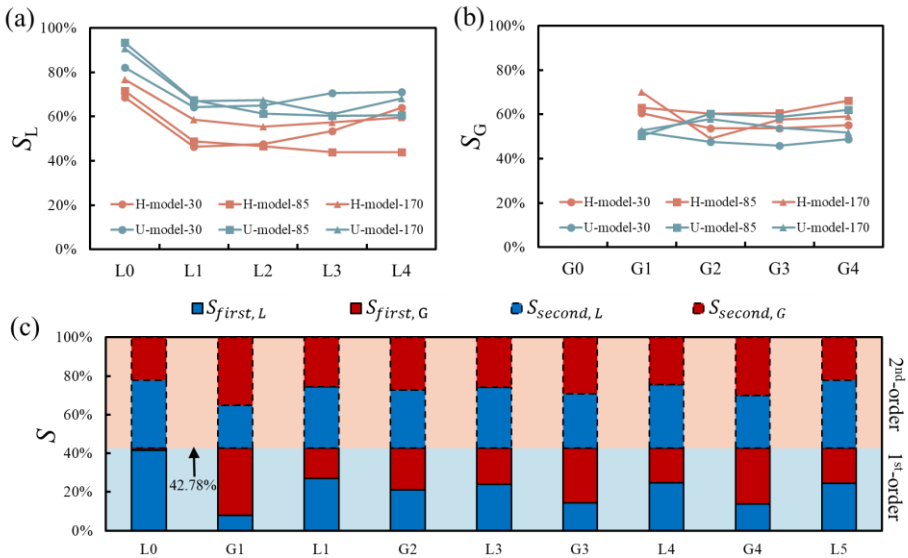

Figure 4-15 Saturation of liquid phase (a) and gas phase (b) during cyclic liquid and gas invasion in uniform and hierarchical structures; (c) liquid and gas saturation in various order structure of hierarchical structure at 170 mL/h flow rate. (Solid border: 1st-order structure; dotted border: 2nd-order structure).

Finally, quantitative study on cycle gas-liquid injection in hierarchical porous media was conducted compared with the uniform porous media. The results were separated into liquid invasion (Figure 4-15 (a)) and gas invasion (Figure 4-15 (a) illustrates the diminishing trend in liquid saturation S_L for both uniform and hierarchical structures as the number of cycles increases. The curves gradually level off during the cyclic invasion of both uniform and hierarchical structures, exhibiting fluctuations within the range of 50% to 70%. As depicted in Figure 4-15 (a), S_L of **U-model** is higher than that of **H-model** during liquid cyclic invasion. This discrepancy arises from the robust gas trapping effect in the 2nd-order structure of **H-model** mention above, resulting in a substantial amount of gas residue. Figure 4-15 (b) reveals no significant difference in gas saturation S_G between **U-model** and **H-model** during gas invasion. To further explore the invasion saturation evolution in different order structures of **H-model**, stacked column charts of saturation in 1st and 2nd-order structures were illustrated

in Figure 4-15 (c). It was found that the changes in gas and liquid saturations within the 1st-order structure are more pronounced than those in the 2nd-order structure during cyclic invasion. This reconfirms the earlier findings regarding the preferential invasion in the 1st-order structure and the potent capillary trapping effect in the 2nd-order structure. The diminishing trend of liquid saturation S_L observed in Figure 4-15 (a) signifies the manifestation of the saturation hysteresis effect during cyclic injection, which holds implications for the storage and extraction efficiency in UHS applications. In the subsequent section, a detailed comparison of the hysteresis effect between **U-model** and **H-model** will be conducted.

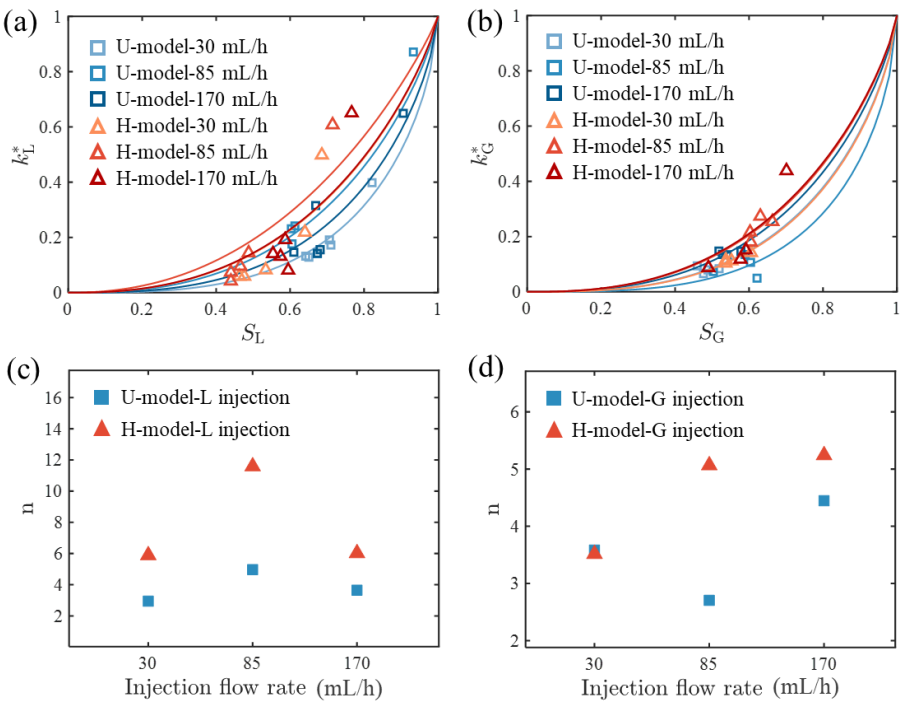

Figure 4-16 (a, b) Relative permeability as a function of saturation for liquid and gas invasions, respectively (solid lines: van Genuchten model fitting curve [115]); (c, d) comparison of model parameter between **U-model** and **H-model** for liquid and gas injection, respectively.

Next, absolute permeability was quantified by using LBM simulation as descripted by section 3.5.5. The relative permeability k_G^* of the gas phase and k_L^* of the liquid phase are calculated by Equation (3-32). As shown in Figure 4-16 (a, b), relative permeability increases with the increase of saturation in both gas and liquid invasions. To show the difference more clearly between **U-model** and **H-model**, data was fitted by the van Genuchten model analytically integrated into the Mualem's relative permeability model [115, 116]:

$$k^* = S^{\epsilon}\left(1-\left(1-S^{1/m}\right)^m\right)^2 \tag{4-16}$$

The van Genuchten parameter $m = 1 - 1/n$ was obtained and then n was plotted in Figure 4-16 (c, d). The results show that **H-model** has a higher n than **U-model.** The presence of additional pore spaces within the 2nd-order structure is the main reason.

4.2.3 Dynamical invading behavior

Fingering evolution during gas-liquid two-phase displacement

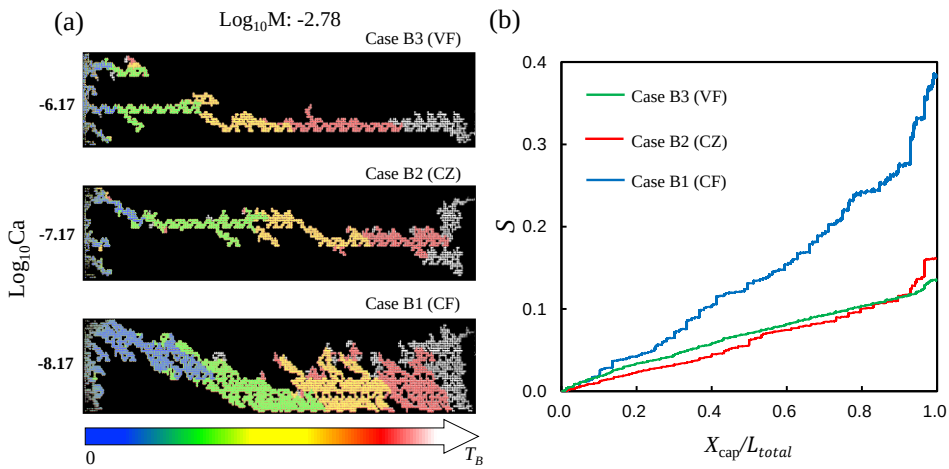

Figure 4-17 Invading process and evolution of fingering patterns before breakthrough: (a) finger evolution of invasion process in VF (Case B3), CZ (Case B2) and CF (Case B1) regions until breakthrough, respectively; (b) corresponding saturation curve as a function of the normalized location of finger cap X_{cap}/L_{total}, where L_{total} is the length of porous media domain.

Figure 4-17 (a) shows the gas displacement process before breakthrough. To intuitively show the displaced location in each period, images were painted in different colors according to different periods from 0 to T_B. In the earlier period (painted in blue), the displacement is compact. As the displacement progresses, the compact displacement is broken by one or two preferential flow paths (painted in green). The interface gradually becomes unstable. A sudden rise in fingering branches occurs in the final period of invasion (painted in white). So, the sudden increase at the end of the saturation curves in Figure 4-17 (b) can be observed. It is more prominent in the CZ and CF regions. Because The capillary dispersion effect allows the cap to invade the branches. It is also interesting to observe the minor newly displaced area (painted in red and white) appears near the inlet in the VF region close to breakthrough, which strongly motivates us to explore the fingering evolution from breakthrough to steady state.

As shown in Figure 4-18 (a), dramatic changes of fingering patterns are observed in the VF regime after breakthrough. Figure 4-18 (a) illustrates the fingering evolution in VF region from breakthrough moment T_B to steady state T_S. Most of the displaced area is located near the outlet except for case D3, leaving the uninvaded area near the inlet. As the decrease of liquid viscosity (increase of $Log_{10}M$), the saturation reaches S_S in earlier times. As illustrated by the curves of S in Figure 4-18 (b), the slope of saturation curves shows a positive relationship with $Log_{10}M$. It is because the lower liquid viscosity, the weaker resistance. The curves are approximately linear before T_B. Fluctuation begin to occur after T_B. After the turning point indicated by the dotted circles, the curves flatten and steady state T_S reaches.

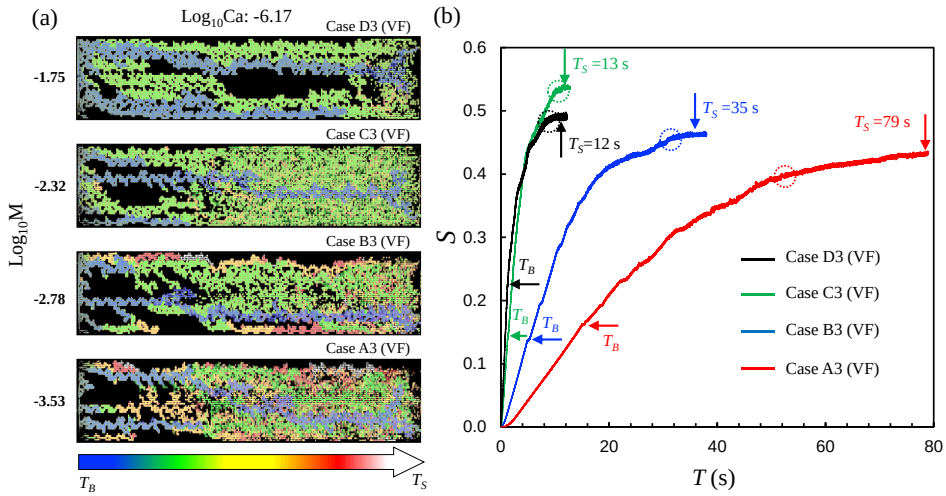

Figure 4-18 Invading process and finger evolution from breakthrough to steady state in VF region. (a) evolution of invasion process after breakthrough (painted in different colors according to different periods); (b) saturation curve as a function of the elapsed time T.

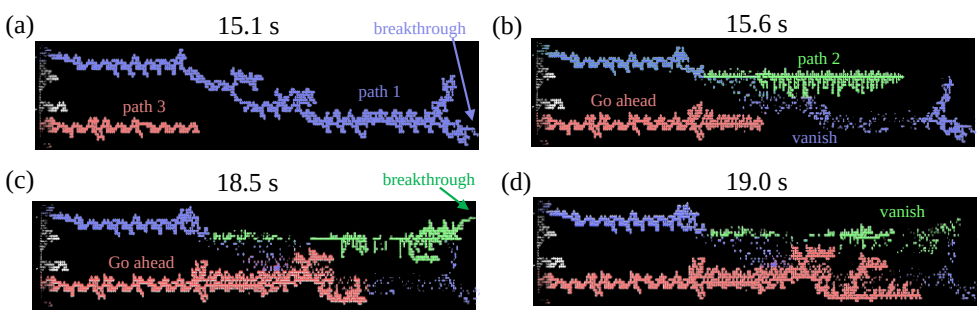

Figure 4-19 Time evolution of fingering after breakthrough in VF region at the case A3, where different paths were painted in different colors.

In order to dig into the underlying mechanism, time evolution of fingering after breakthrough in VF region is analyzed. Taking case A3 as an example, a previously unobserved finger vanishing and re-forming cycle was found. Figure 4-19 (a) illustrates that path 1 breakthrough preferentially compared with path 3. After a short time of about 0.5 s, the front part of path 1 disappears, leaving the disconnected ganglia (Figure 4-19 (b)). Such fingering instability is originally caused by the sudden decrease of the entry pressure P_c at breakthrough moment, which can be estimated by:

$$P_c = \frac{2\sigma \cos \theta_R}{r} \tag{4-17}$$

Entry pressure is calculated as about 2000 Pa by using a receding contact angle θ_R of 30° and throat size r of 63 μm. After breakthrough, high entry pressure is released. Air only needs to overcome the relatedly lower flow resistance. So, the front part of path 1 escapes fast. A similar phenomenon also can be found in previous research [117]. The finger vanishing and disconnected ganglia will quickly restore the pressure, which facilitates the generation of new path 2. After about 3 s, path 2 breaks through and becomes disconnected as shown in Figure 4-19 (c). Similar to path 1, the front part of path 2 disappears after about 0.5 s, leaving scattered dots (Figure 4-19 (d)). All in all, each path will repeat a process, including new finger forming, cap invading, breakthrough and finger vanishing. Until saturation reaches the maximum, a steady state reaches.

Fingering evolution during three-phase displacement

Figure 4-20 (a, c) depicts the time evolution of the gas invasion process in three-phase displacement. Similar to the two-phase displacement (Figure 4-17 (a)), the invasion process in G→(HL→LL) begin as soon as the gas entered the porous domain, with fingers gradually generating at the interface between the gas and liquid. Compared to common fingering pattern in G→(HL→LL), completely different yarn-liked pattern was observed in G→(LL→HL), confined within a single channel. Within these narrow flow paths, the flow speed increases, giving rise to the thin yarn-like finger pattern responsible for the ultra-fast invading speed in G→(LL→HL). As depicted in Figure 4-20 (c), the yarn-like structure becomes denser but less twisted at higher Ca number. Near breakthrough, disconnected gas ganglia are observed, highlighted in white. Especially at the highest Ca number, numerous scattered gas ganglia appeared near the outlet. The saturation curve of each phase during gas invasion (Figure 4-20 (d)) illustrates that LL saturation drops much faster than that of HL. Particularly at lower Ca number, the HL saturation curve levels off, indicating that gas primarily invades the pores occupied by LL. The main reason is because lower viscosity of LL lead to lower invasion resistance.

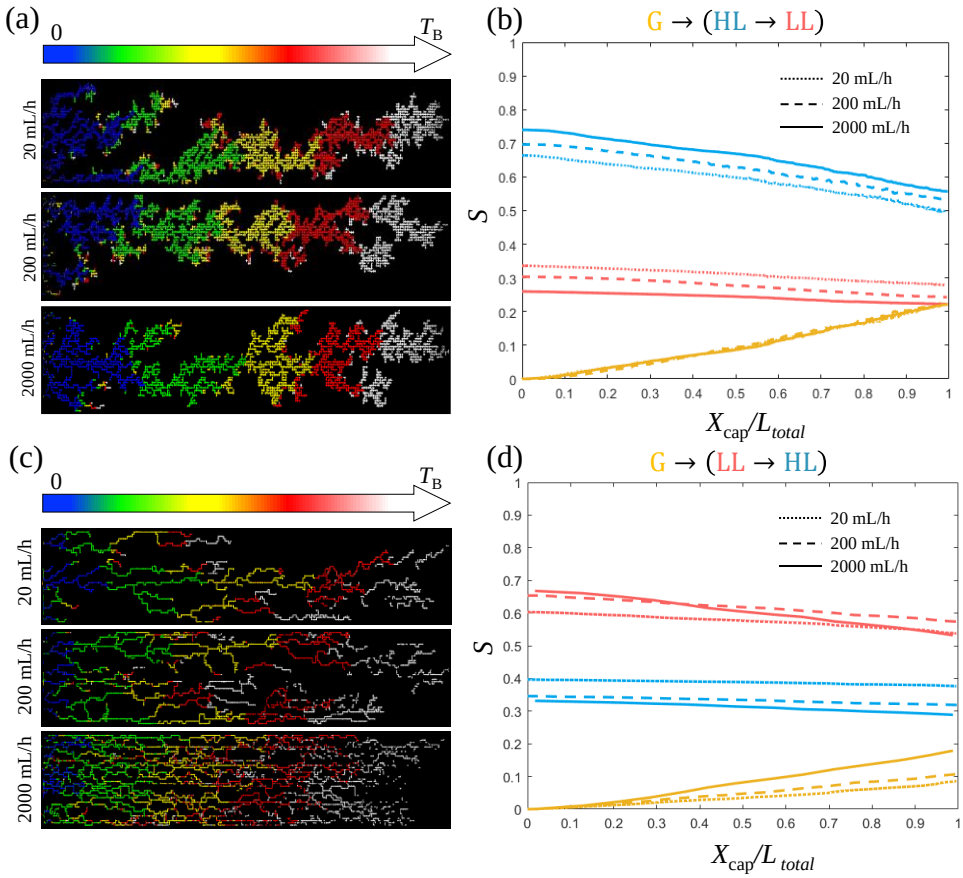

Figure 4-20 Time evolution of gas invasion process in G→(HL→LL) before breakthrough. (b) Corresponding saturation curve. (c) Time evolution of gas invasion process in G→(LL→HL) before breakthrough. (d) Corresponding saturation curve. (X_{cap}/L_{total} is the normalized location of finger cap, where L_{total} is the length of porous media domain.

Dynamics hysteresis during cycle gas-liquid invasion in hierarchical porous media

Based on Land trapping model [83, 118], the hysteresis effect was quantified during gas-liquid cyclic injection:

$$S_{\mathrm{r,G}} = \frac{S_{\mathrm{i,G}}}{1+C\,S_{\mathrm{i,G}}} \tag{4-18}$$

Here, the initial gas saturation $S_{\mathrm{i,G}}$ and the residual gas saturation $S_{\mathrm{r,G}}$ were measured when the gas and liquid invasion reach steady state, respectively. Figure 4-21 (a) illustrates the trajectories of $S_{i,G}$ and $S_{r,G}$ starting from $S_{\mathrm{i,G}} = 1$ during cyclic injections, representing the

evolution of saturation hysteresis over the cycles. C denotes the Land trapping coefficient, with two black solid curves plotted for C values of 0.4 and 2. In **U-model**, trajectories after cycle 0 remain within the range of the two black solid curves. Conversely, for all injection flow rates, the trajectories of **G-model** exceed the upper boundary curve of 0.4, subsequently reverting back towards higher C. $S_{\mathrm{r,G}}$ in **H-model** is higher than that in **U-model**, attributed to the stronger capillary trapping effect of the 2nd-order structure. As the number of cyclic injections increases, the trajectories of both **U-model** and **H-model** gradually converged within a small area, indicating the attainment of hysteresis equilibrium. The stabilization of the invasion fingering pattern in Figure 4-11 is also a manifestation of hysteresis equilibrium. Notably, trajectories of the hierarchical structure cover a larger range than those of the uniform structure, suggesting more difficulty for the hierarchical structure to reach hysteresis equilibrium.

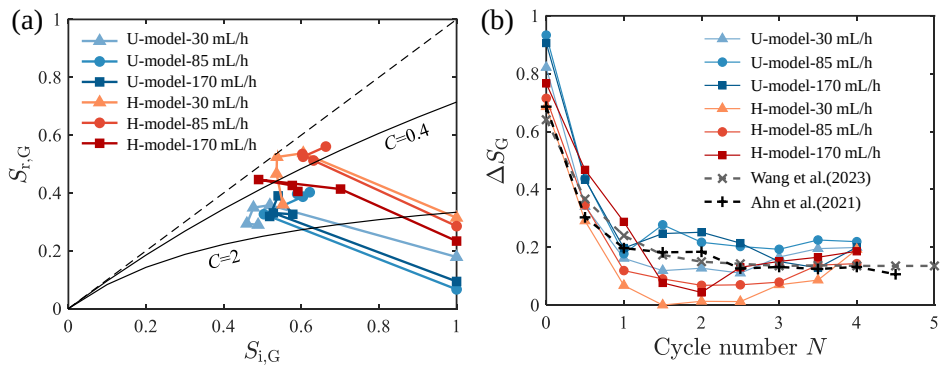

Figure 4-21 Trajectories of initial and residual gas saturation during cyclic injections with varying invasion flow rates in uniform and hierarchical structures; (b) evolution of gas saturation hysteresis ΔS_{G} with cycle number N in uniform and hierarchical structures. (Dash line with marker "+" is from Ahn et al. [119]'s experimental data. Dash line with marker "×" is from Wang et al. [62]'s numerical data.)

To quantify the strength of hysteresis effect, the difference ΔS_{G} between $S_{\mathrm{r,G}}$ and $S_{\mathrm{i,G}}$ was calculated in the neighboring cycles as shown in Figure 4-21 (b). The saturation hysteresis was compared with experimental and simulation data from existing literature. Our ΔS_{G} data initially exhibits an exponential decay with the increase in cycle number N, closely aligning with the trends observed by Wang et al. [62] and Ahn et al. [119]. The curves of ΔS_{G} for the hierarchical structure reach their lowest points in cycle 2, which correspond to points on the trajectories close to the diagonal dashed line in Figure 4-21 (a), representing zero hysteresis. At these points, the change in gas saturation during alternate gas and liquid invasion approaches zero ($S_{\mathrm{r,G}}$ approaches $S_{\mathrm{i,G}}$). As illustrated in Figure 4-11, a significant cluster of trapped gas forms in hierarchical porous media, particularly at lower flow rates, indicating the presence of more connected gas paths leading to rapid breakthrough. The release of pressure difference results in hysteresis effect nearing zero. It is confirmed by the sharp

decrease in the newly invaded area after cycle 1. In comparison, the evolution of ΔS_G for the uniform structure lies above that of the hierarchical structure, which suggests that the hierarchical structure shows a weaker saturation hysteresis effect. This disparity in hysteresis prompts further investigation into the underlying mechanism.

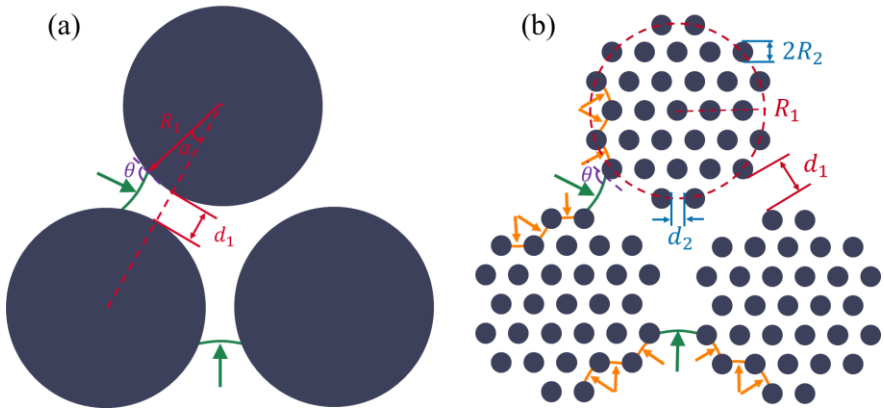

Figure 4-22 Model for calculating the capillary pressure as invading phase invades through the gap between cylinders: (a) uniform arrangement only with 1st-order structure; (b) hierarchical arrangement with 1st-order structure and 2nd-order structure.

Let's first introduce a discrete-domain model from Cueto-Felgueroso and Juanes (2016) [7] that can be described the pore filling event. In this model, porous media is conceptualized as an interconnected multistable capillary tube network. The macroscopic invasion behavior observed in the porous media emerges from the collective microscopic behavior of these capillary tubes. Consequently, the invasion path and menisci movement are influenced by the local energy barrier of the capillary tube, namely the entry capillary pressure. Figure 6 illustrates the meniscus movement of the gas-liquid interface in both uniform and hierarchical porous media, with arrows indicating the direction of progress. Throughout the invasion process, the invading phase must overcome the entry capillary pressure [120], which is calculated as:

$$P_c = \frac{\gamma \cos(180-\theta-\alpha)}{\frac{1}{2}d+R[1-\cos(\alpha)]} \tag{4-19}$$

Here, $\alpha \in [-\pi/2,\ \pi/2\,]$ are the filling angle and θ is contact angle. γ is the surface tension. d is the gap between the cylinders, i.e., d_1 or d_2 for the 1st-order structure and 2nd-order structure. R is the cylinder radius, i.e., R_1 or R_2 for uniform and hierarchical structures. Clearly, the gap d_2 in the 2nd-order structure is narrower than d_1 in the 1st-order structure. This discrepancy implies a higher entry capillary pressure, indicating an augmented energy barrier between different meta-stable states and enhancing the stability of menisci. In simpler terms, the invading phase must overcome a higher entry capillary pressure P_c to invade the 2nd-order structure compared to 1st-order structure. It explains the main findings in section

3.1, regarding the preferential invasion in the 1st-order structure and robust capillary trapping in the 2nd-order structure. Furthermore, the discrete-domain model can also be used to explain the weaker saturation hysteresis effect observed in **H-model**. The restricted motion of menisci in **H-model** suggests a relatively stable gas-liquid distribution during cyclic injection. Consequently, the saturation hysteresis effect is limited in **H-model**.

4.2.4 Local invading dynamics and ganglia mobilization

Local invading dynamics during gas-liquid two-phase displacement

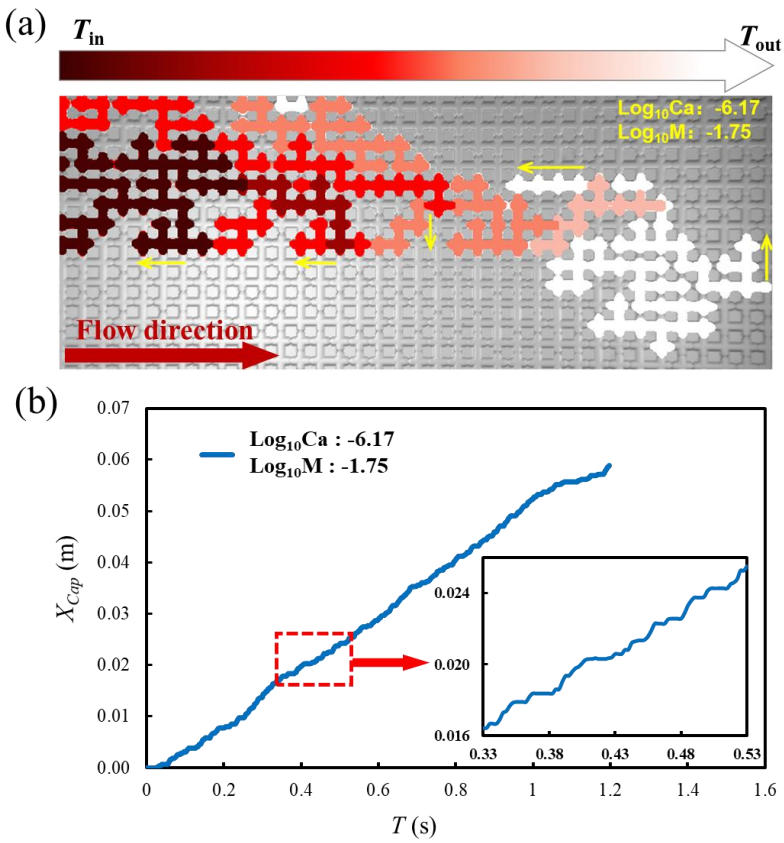

Figure 4-23 (a) local dynamical invasion behavior captured by high-speed camera with macro lens (painted in different colors according to different periods); (b) curve of fingering cap position over time.

To explore the local dynamical invasion behavior, the reduced visualization window was monitored as shown in Figure 4-23 (a). The cap of fingering moves forward with time T. As shown in the yellow arrows of Figure 4-23 (a), the cap stop moves forward and its gas

branches expand in other directions, especially in backward direction. It is because the driving pressure has not yet accumulated large enough to overcome the forward entry pressure. After the accumulated pressure is enough, the cap will continue to invade forward. This process can be verified by the curve of finger cap position over time in Figure 4-23 (b). As shown in Figure 4-23 (b), the gas cap moves in a stepwise way.

Local invading dynamics and ganglia movement during three-phase displacement

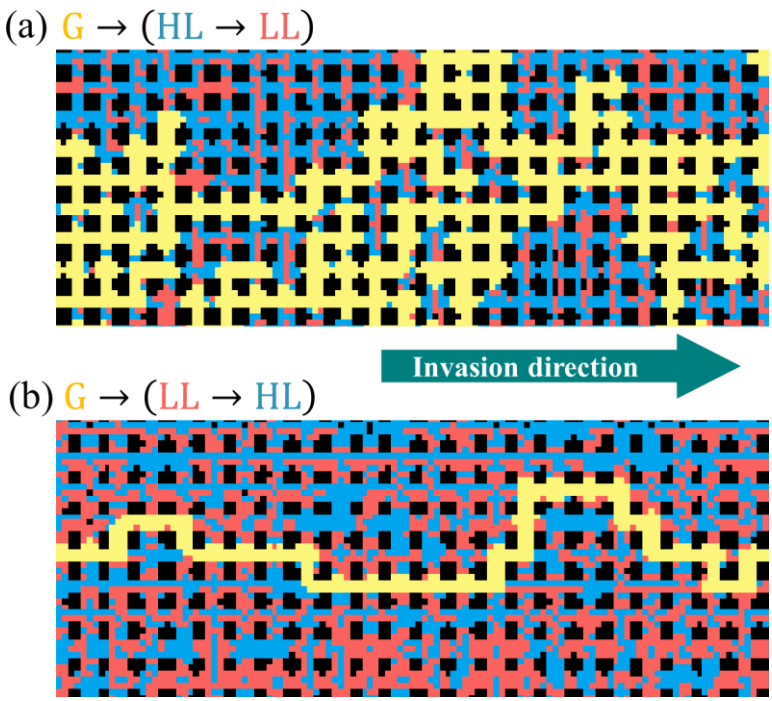

Figure 4-24 Microscopically observation in the cases of (a) G→(HL→LL) and (b) G→(LL→HL) at 20 mL/h flow rate.

To elucidate the underlying mechanisms driving the different observed patterns, a local dynamics analysis was conducted, as depicted in Figure 4-24. Distinct local gas invasion behavior was observed in the G→(HL→LL) and G→(LL→HL) processes. In the G→(LL→HL) scenario (Figure 4-24 (b)), following the LL→HL displacement reaching steady state, the interconnected LL pattern and scattered HL were generated. In a multi-fluid system, gas tends to displace pore spaces occupied by lower-viscosity liquid due to reduced resistance. Therefore, gas primarily invading the LL channel. This behavior is further confirmed by the saturation evolution of the HL and LL phases depicted in Figure 4-20 (d), where LL saturation decreases much faster than that of HL. Notably, in this context, LL (Hexane) serves as the wetting phase and is completely hydrophilic on quartz glass (refer to

Table 1). During the LL→HL process, LL tends to generate as a thin residue layer in the smallest pores and throats (Alhosani et al., 2021a). Meanwhile, the scattered HL further constrains the growth of the gas pathway width. Consequently, the yarn-like fingering pattern rapidly emerges during G→(LL→HL) displacement. In contrast to the G→(LL→HL) process, HL acts as the invading phase during HL→LL displacement of G→(HL→LL) scenario. After reaching steady state, LL becomes scattered while HL interconnects, as depicted in Figure 4-24 (a). During gas invasion, the absence of an interconnected LL channel forces the gas to displace the HL. The high viscosity of the liquid suppresses the gas rapid breakthrough and promotes bypass invasion, resulting in an increase in finger width. Consequently, the yarn-like fingering pattern observed in G→(LL→HL) disappears during G→(HL→LL) displacement.

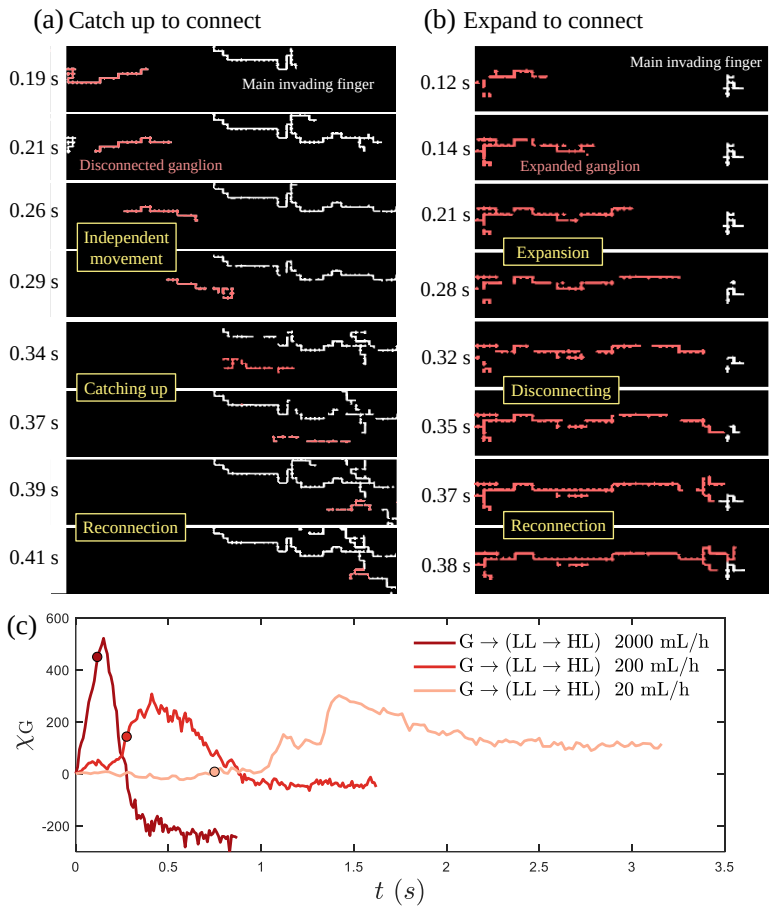

Figure 4-25 Two connection types of ganglia mobilization in G→(LL→HL) with 200 mL/h flow rate: (a) "Catch up to connect" and (b) "Expand to connect" (Number represents

absolute time with unit second). (c) Evolution of Euler connectivity of gas at different flow rates (Circle dots represent breakthrough moment).

Compared with G→(HL→LL), frequent gas ganglia movement is observed during G→(LL→HL). These ganglia can move independently, either slower or faster than the main finger fronts. Their movement significantly impacts the dynamic connectivity and reorganization of the flow path, thereby influencing phase distribution [121]. Therefore, it is imperative to explore local invading dynamics and ganglia mobilization.

By tracking the movement of all gas ganglia prior to breakthrough, I discerned two categories of ganglia movement and connection, named as "catch up to connect" and "expand to connect," as shown in Figure 4-25 (a, b). In the first category, gas ganglion (highlighted in red) moves faster than the advancing finger front. Initially moving alone, the ganglion eventually catches up and actively reconnects with the main invading finger (highlighted in white). The motion is primarily impelled by the liquid from behind. Conversely, in the second scenario, the gas ganglion does not fully detach from the gas behind. Instead, the gas ganglion expands forward with the continuous influx of invading gas, although occasionally remaining disconnected. Upon contact with the main invading finger, reconnection of the ganglia is completed.

From the observation of the invasion process spanning from the breakthrough moment to steady state, it was noted that the majority of ganglia reconnected to the flow path after breakthrough, facilitated by the continuous invasion. As shown in SS4 of Figure 4-10, nearly all gas become interconnected at steady state. To explain the reconnections, the Euler number χ_G of gas phase was quantified. Figure 4-25 (c) shows the temporal evolution of χ_G spanning from initiation to steady state. At higher flow rates of 200 and 2000 mL/h, χ_G exhibits an ascending trend as gas invasion progresses, suggesting the generation of disconnected ganglia and reduced connectivity. This upward trend becomes steeper at higher flow rates. Remarkably, χ_G fluctuates around 0 at a flow rate of 20 mL/h, indicating ganglion disconnection equates to connection. After breakthrough, χ_G continues its ascent, followed by a rapid descent, attributed to the continued expansion of fingers and subsequent ganglia reconnection. Eventually, the declining trend stabilizes, marking the attainment of steady state. At steady state, χ_G registers below 0 at higher flow rates of 200 and 2000 mL/h, indicating that there are more loops than disconnected ganglia. As illustrated in Figure 4-25 (c), connectivity at steady state has a positive relationship with invasion flow rates.

Local invading dynamics during cycle gas-liquid injection in hierarchical structure

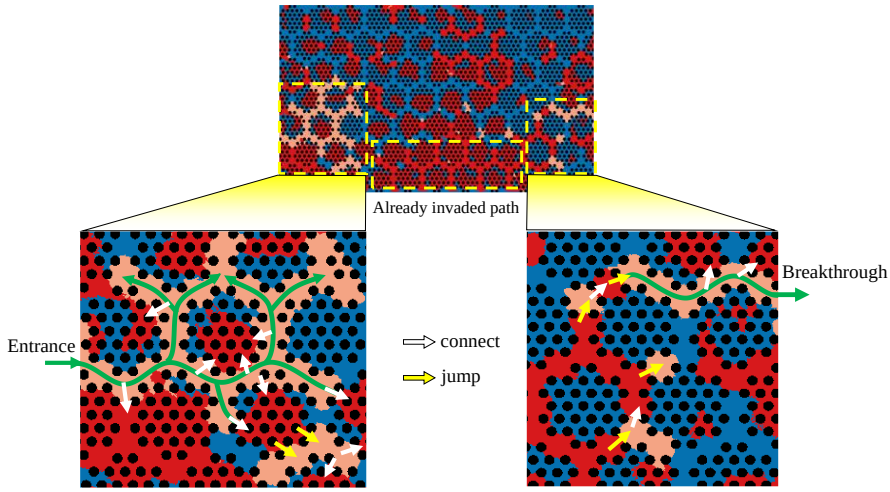

Figure 4-26 Gas connect-jump invasion method in cycle 2 of hierarchical structure.

When the invading phase invades during the invading process, the defending phase also mobilized forward. The newly invaded liquid (light blue) during gas invasion and newly invaded gas (light red) during liquid invasion in Figure 4-11 indicate the mobilization of defending ganglia. Liquid movement during gas invasion is prominent, whereas gas movement during liquid invasion is minimal. Compared to the uniform structure, the mobilization of defending ganglia is rarely observed in the hierarchical structure across all flow rates. To explain this, local invasion behavior of gas invasion in cycle 2 in the hierarchical structure is analyzed as shown in Figure 4-26. Gas enters and primarily invades in the 1st-order structure (green curved arrow). Throughout this process, gas consistently connects with the trapped gas residues in 2nd-order structure (white arrows). Despite the 1st-order path around the 2nd-order structure is invaded by gas, few liquids are still trapped within the 2nd-order structure. When gas connects to the residue gas in a cell ahead, it jumps directly in front of the residue gas to invade (yellow arrows). If the gas paths have already existed ahead, gas invading time is reduced, leading to early breakthrough. This invasion method implies that the newly invaded phase does not establish an entirely new path to achieve breakthrough. this invasion was called as connect-jump method. The mechanism behind the suppression of ganglion mobilization can be explain by the connect-jump invasion method. Owing to lower entry capillary pressure P_c, the invading phase predominantly invades the 1st-order structure, merely going around the 2nd-order cells and connecting with residual phases within 2nd-order structure. Consequently, the pushing force exerted by the invading phase on the defending phase in 2nd-order structure is insufficient to overcome the strong capillary trapping of the 2nd-order structure. Moreover, most defending phases in the 1st-order structure connect to the defending phase in the 2nd-orde structure. Consequently, the movement of defending phase ganglia is limited in the hierarchical structure.

CHAPTER 5

Conclusions and Outlook

5.1 Conclusions

The micro-scale multiphase flows in porous media is essential process in geological storage and extraction applications. The multiphase interaction process is accompanied by the phenomenon of mass transfer or interfacial instability on the gas-liquid interface, which has a significant impact on the economic benefits and storage safety of subsurface applications. In order to reveal the underlying mechanism, a microfluidics platform with a high-speed imaging system was established. First, the research started with a simplified model of a porous media, i.e., single straight microchannels. The gas-liquid flow and mass transfer of deformed bubbles were explored. Then the research was initiated into the pore-scale mechanisms governing multiphase displacement in porous media with microchannel networks, particularly emphasizing fingering evolution after breakthrough and multifluid invasion behavior. Finally, the research was further expanded to the hysteresis effect during the cyclic gas-liquid invasion in hierarchical porous media by 3D printing. The main results are summarized below:

Rectangular and square microchannels:

- Depending on different flow rates, gas-liquid flow patterns in the microchannels include slug flow, bubbly flow, and annular flow. A flow pattern map was proposed and compared with the maps in literature.
- In order to measure the deformed bubble volume in rectangular and square microchannels, the bubble reconstruction methods were developed based on 2D projection and 3D slicing, correspondingly. The important parameters in micro-reactors were quantified. Scaling laws were derived to predict these parameters, which can provide the guidance of microreactor design.
- Based on the rate of change in CO_2 bubble volume, the mass transfer coefficients of bubble were calculated. The new empirical correlations involving dimensionless

numbers were developed to predict the mass transfer coefficients. Further, to have a better universality, a semi-theoretical model, considering the length ratio of liquid and gas phases L_L/L_G in a square microchannel, was developed. Empirical correlations and semi-theoretical model both show a good predictive capability to predict the measured values accurately.

Porous media with microchannel network:

Two-phase displacement:

- Gas-liquid displacement processes before and after breakthrough in a porous media were captured by experimental flow imaging. With a wide range of capillary numbers Ca and viscosity ratios M, the flow region can cover viscous fingering (VF), capillary fingering (CF) and crossover zone (CZ). Visualization of the fingering morphologies illustrates that capillary fingering stops displacement after breakthrough, whereas viscous fingering can continue to expand until almost all the liquid phase is displaced.
- Imperative quantitative studies in terms of invasion velocity, invading area and fingering complexity were conducted based on digital image processing. It is found that displaced areas expand significantly after breakthrough in VF region.
- Fingering dynamical behaviors before and after breakthrough were analyzed. Firstly, compact displacement area is generated near inlet, then it is broken by one or two preferential flow paths. When the fingering approaches the outlet, a sudden rise in fingering branches occurs. After Breakthrough, most displaced area is located near the outlet. The saturation curves keep linear before breakthrough, and begin to fluctuate after breakthrough. Then the curves flatten and a steady state reaches.
- By analyzing time evolution of fingering after breakthrough, a previously unobserved circle was discovered, involving new finger generation, cap invading, breakthrough and finger vanishing. This process repeats until steady state. Analysis of local dynamical invasion behavior exposes a stepwise way of fingering cap movement. The fingering cap will temporarily stop invading forward and its branches will expand in other directions especially backward when accumulated gas pressure is not sufficient to overcome the forward entry pressure.

Three-phase displacement:

- When gas displaces multi-fluids, the gas fingering pattern highly depends on the historical occupation sequences of the liquids. A novel yarn-like gas (G) fingering pattern is observed during the G→(LL→HL) displacement, where high viscosity liquid (HL) precedes low viscosity liquid (LL) prior to gas invasion.
- Residual saturation of the initial phase at a steady state indicates that three-phase displacement has superior displacement efficiency compared to two-phase displacement. Even at a low injection rate of 20 mL/h, the displacement efficiency of three-phase displacement surpasses that of two-phase displacement at a high rate

of 2000 mL/h, indicating innovative strategies for enhancing extraction efficiency while reducing energy consumption.

- Local invading dynamics was studied to expose the formation of yarn-like fingers. In G→(LL→HL) scenario, gas tends to invade interconnected LL channel, while the scattered HL limits the growth of finger width. Conversely, in G→(HL→LL) scenario, HL is interconnected, so the gas must displace HL. High resistance promotes bypass invasion, resulting in the disappearance of yarn-like pattern.
- Through capturing residue ganglia movement, two types of ganglia connection were distinguished in G→ (LL→HL) scenario. They are "catch up to connect" and "expand to connect". Euler number was calculated to evaluate gas finger connectivity. Euler number shows an initial ascending trend as the time, which is caused by the appearance of disconnected gas ganglia. Due to the expansion and reconnection of ganglia, Euler number decreases rapidly after breakthrough. Upon reaching a steady state, the declining trend slows down and flatten.

Cyclic invasion in hierarchical porous media

- The fingering morphology at breakthrough moment shows that the invasion pattern gradually stabilizes into the same path during cycle injection of uniform and hierarchical structures. In the hierarchical structure, invasion predominantly occurs in 1st-order structures and gas is significantly trapped by capillary force in 2nd-order structures. This observation is further supported by the quantification of phase saturation at each level of the hierarchical structure.
- Quantitative study was conducted using relative permeability estimated by Lattice Boltzmann method (LBM). The result shows that relative permeability have a positive relationship with saturation and hierarchical structure has a higher van Genuchten model parameter.
- The evolution of saturation hysteresis during cyclic injection was assessed by Land model. In the hierarchical structure, trajectories of initial and residual gas saturation are close to zero hysteresis. In uniform structures, hysteresis tends to stabilize more rapidly. The hierarchical structure has the lower land coefficient C, indicating a weaker saturation hysteresis effect compared to uniform structures. The saturation hysteresis is compared using experimental and numerical data from the literature.
- The significant mobilization of residue ganglion is observed in the uniform structure. Conversely, ganglion's mobilization is absent in the hierarchical structure, attributed to the connect-jump invasion mechanism observed. Furthermore, the higher local energy barrier in the discrete-domain model, i.e., the entry capillary pressure in 2nd-order structures, is responsible for the suppression of hysteresis effects in the hierarchical structure.

5.2 Outlook

Microchannel:

- Breakup hydrodynamic at the junction is of great significance in two-phase flow in micro-scale. Although extensive work has been devoted to revealing the underlying mechanism, a reliable theoretical model has not been established.
- Current two-dimensional flow imaging system should be improved to capture image from Z-axis to reconstruct three-dimensional bubble shape. CFD simulations can also be used for mutual verification.

Porous media with microchannel network:

- 2D porous media was used in this thesis. However, in reality, porous media structure is three-dimensional. Therefore, the investigation of immiscible displacement in a realistic 3D configuration is more meaningful. However, it is also important to consider that traditional micro-CT methods have no way of capturing transient invasion dynamics due to scan time limitations.
- Capillary pressure, determined by microchannel size, surface tension of fluid and contact angle of fluid on channel wall, is a driving force for wetting fluids through microchannels, while is a resistance for no-wetting fluids. Although simulation has been used to explore the influence of wettability on invading behavior in porous media, experimental validation is still required, particularly for mixed wettability and gradient wettability.
- Lattice Boltzmann simulation (LBM) is a suitable method to study microscale flow, especially in complex microscale structures where LBM has an inherent advantage over traditional numerical method based on N-S equations. I believe LBM will perform well in modeling displacement in hierarchical porous media.

Authors' Contributions to Included Papers

Paper i: Experimental study of gas-Liquid Mass transfer in a rectangular microchannel by digital image analysis method
***Shuo Yang**, Gaopan Kong, Zan Wu**
ASME International Mechanical Engineering Congress and Exposition, 2021, Nov 1 (Vol. 85666, p. V010T10A040).

In this paper, I built up the microfluidic platform together with Gaopan Kong. I carried out the experiments, collected and analyzed the data. The first manuscript was written by me, and revised by Gaopan and Zan Wu. Gaopan and Zan Wu helped with technical suggestions and gave feedback.

Paper ii: Mass transfer and modeling of deformed bubbles in square microchannel
***Shuo Yang**, Gaopan Kong, Zhen Cao, Zan Wu**
Chemical Engineering Journal Advances, 2023, 16: 100518.

In this paper, I built up the microfluidic platform together with Gaopan Kong. I carried out the experiments, collected and analyzed the data. The first manuscript was written by Gaopan Kong and me, and revised by Zhen Cao and Zan Wu. Gaopan Kong, Zhen Cao and Zan Wu helped with technical suggestions and gave feedback.

Paper iii: Hydrodynamics of gas-liquid displacement in porous media: fingering pattern evolution at the breakthrough moment and the steady state
Shuo Yang**, Gaopan Kong, Zhen Cao, Zan Wu*, Hongxia Li
Advances in Water Resources, 2022, 170: 104324.

In this paper, I built up the test rig of porous media, carried out the experiments, collected and analyzed the data. The first manuscript was written by me, and revised by Gaopan Kong, Zhen Cao, Hongxia Li and Zan Wu. They both helped with technical suggestions and gave feedback.

Paper iv: Viscous-dependent fingering dynamics of gas invading into multi-fluids
Shuo Yang**, Hongxia Li*, Si Suo, Zan Wu
Advances in Water Resources, 2024, 191: 104757.

In this paper, I built up the test rig of porous media, carried out the experiments, collected and analyzed the data. The first manuscript was written by me, and revised by Hongxia Li, Si Suo and Zan Wu. They both helped with technical suggestions and gave feedback.

Paper v: Experimental study on hysteresis during cyclic injection in hierarchical porous media

Shuo Yang*, *Si Suo, Yixiang Gan, Lei Wang, Shervin Bagheri, Johan Revstedt*
Water Resources Research, under review.

In this paper, I designed, 3D printed and assembled porous media micromodel together with Si Suo. Shervin Bagheri provided 3D printing resource. I built up the test rig of porous media, carried out the experiments, collected and analyzed the data. The first manuscript was written by me, and revised by Si Suo, Yixiang Gan, Shervin Bagheri, Johan Revstedt. Si Suo, Yixiang Gan, Lei Wang, Shervin Bagheri, Johan Revstedt helped with technical suggestions and gave feedback.

References

[1] H. Hematpur, R. Abdollahi, S. Rostami, M. Haghighi, M. Blunt, Review of underground hydrogen storage: Concepts and challenges, *Advances in Geo-Energy Research*, 7(2) (2023) 111-131.

[2] A. Manz, N. Graber, H.á. Widmer, Miniaturized total chemical analysis systems: a novel concept for chemical sensing, *Sensors actuators B: Chemical*, 1(1-6) (1990) 244-248.

[3] J. McGinty, V. Svoboda, P. Macfhionnghaile, H. Wheatcroft, C.J. Price, J. Sefcik, Continuous crystallisation of organic salt polymorphs, *Frontiers in Chemical Engineering*, 4 (2022).

[4] H.M. Hegab, A. ElMekawy, T. Stakenborg, Review of microfluidic microbioreactor technology for high-throughput submerged microbiological cultivation, *Biomicrofluidics*, 7(2) (2013) 021502.

[5] B.S. Ferguson, S.F. Buchsbaum, T.-T. Wu, K. Hsieh, Y. Xiao, R. Sun, H.T. Soh, Genetic analysis of H1N1 influenza virus from throat swab samples in a microfluidic system for point-of-care diagnostics, *Journal of the American Chemical Society*, 133(23) (2011) 9129-9135.

[6] C.D. Edington, W.L.K. Chen, E. Geishecker, T. Kassis, L.R. Soenksen, B.M. Bhushan, D. Freake, J. Kirschner, C. Maass, N. Tsamandouras, Interconnected microphysiological systems for quantitative biology and pharmacology studies, *Scientific reports*, 8(1) (2018) 1-18.

[7] L. Cueto ‐ Felgueroso, R. Juanes, A discrete ‐ domain description of multiphase flow in porous media: Rugged energy landscapes and the origin of hysteresis, *Geophysical Research Letters*, 43(4) (2016) 1615-1622.

[8] J. Yue, G. Chen, Q. Yuan, L. Luo, Y. Gonthier, Hydrodynamics and mass transfer characteristics in gas-liquid flow through a rectangular microchannel, *Chemical Engineering Science*, 62(7) (2007) 2096-2108.

[9] Z. Wu, B. Sundén, Liquid-liquid two-phase flow patterns in ultra-shallow straight and serpentine microchannels, *Heat and Mass Transfer*, 55(4) (2019) 1095-1108.

[10] M. Sattari-Najafabadi, M. Nasr Esfahany, Z. Wu, B. Sunden, Mass transfer between phases in microchannels: A review, *Chemical Engineering and Processing - Process Intensification*, 127 (2018) 213-237.

[11] O. Baker, Design of pipelines for the simultaneous flow of oil and gas, in: Fall meeting of the petroleum branch of AIME, OnePetro, 1953.

[12] K.A. Triplett, S. Ghiaasiaan, S. Abdel-Khalik, D. Sadowski, Gas–liquid two-phase flow in microchannels Part I: two-phase flow patterns, *International Journal of Multiphase Flow*, 25(3) (1999) 377-394.

[13] M. Akbar, D. Plummer, S.M. Ghiaasiaan, On gas-liquid two-phase flow regimes in microchannels, *International Journal of Multiphase Flow*, 29(5) (2003) 855-865.

[14] H. Niu, L. Pan, H. Su, S. Wang, Flow pattern, pressure drop, and mass transfer in a gas-liquid concurrent two-phase flow microchannel reactor, *Industrial and Engineering Chemistry Research*, 48(3) (2009) 1621-1628.

[15] C. Yao, Y. Zhao, H. Ma, Y. Liu, Q. Zhao, G. Chen, Two-phase flow and mass transfer in microchannels: A review from local mechanism to global models, *Chemical Engineering Science*, 229 (2021) 116017.

[16] R. Lindken, M. Rossi, S. Große, J. Westerweel, Micro-particle image velocimetry (µPIV): recent developments, applications, and guidelines, *Lab on a Chip*, 9(17) (2009) 2551-2567.

[17] Q. Li, P. Angeli, Experimental and numerical hydrodynamic studies of ionic liquid-aqueous plug flow in small channels, *Chemical Engineering Journal*, 328 (2017) 717-736.

[18] W.G. Whitman, The two-film theory of gas absorption, *Chem. Metall. Eng.*, 29 (1923) 146-148.

[19] Y. Zhang, C. Zhu, C. Chu, T. Fu, Y. Ma, Mass transfer and capture of carbon dioxide using amino acids sodium aqueous solution in microchannel, *Chemical Engineering Processing-Process Intensification*, 173 (2022) 108831.

[20] Y. Chen, C. Zhu, T. Fu, Y. Ma, Mass transfer enhancement of CO_2 absorption into [Bmim][BF4] aqueous solution in microchannels by heart-shaped grooves, *Chemical Engineering Processing-Process Intensification*, 167 (2021) 108536.

[21] C. Zhu, C. Li, X. Gao, Y. Ma, D. Liu, Taylor flow and mass transfer of CO_2 chemical absorption into MEA aqueous solutions in a T-junction microchannel, *International Journal of Heat and Mass Transfer*, 73 (2014) 492-499.

[22] C. Yao, Y. Liu, S. Zhao, Z. Dong, G. Chen, Bubble/droplet formation and mass transfer during gas–liquid–liquid segmented flow with soluble gas in a microchannel, *AIChE Journal*, 63(5) (2017) 1727-1739.

[23] C. Yao, Z. Dong, Y. Zhao, G. Chen, An online method to measure mass transfer of slug flow in a microchannel, *Chemical Engineering Science*, 112 (2014) 15-24.

[24] X. Ye, T. Hao, Y. Chen, X. Ma, R. Jiang, Liquid film transport around Taylor bubble in a microchannel with gas cavities, *Chemical Engineering Processing-Process Intensification*, 148 (2020) 107828.

[25] L. Bai, S. Zhao, Y. Fu, Y. Cheng, Experimental study of mass transfer in water/ionic liquid microdroplet systems using micro-LIF technique, *Chemical Engineering Journal*, 298 (2016) 281-290.

[26] R.S. Abiev, C. Butler, E. Cid, B. Lalanne, A.-M. Billet, Mass transfer characteristics and concentration field evolution for gas-liquid Taylor flow in milli channels, *Chemical Engineering Science*, 207 (2019) 1331-1340.

[27] G.M. Homsy, Viscous fingering in porous media, *Annual review of fluid mechanics*, 19(1) (1987) 271-311.

[28] S. Hill, Channeling in packed columns, *Chemical Engineering Science*, 1(6) (1952) 247-253.

[29] P.G. Saffman, G.I. Taylor, The penetration of a fluid into a porous medium or Hele-Shaw cell containing a more viscous liquid, *Proceedings of the Royal Society of London. Series A. Mathematical and Physical Sciences*, 245(1242) (1958) 312-329.

[30] B. Zhao, C.W. MacMinn, R. Juanes, Wettability control on multiphase flow in patterned microfluidics, *Proceedings of the National Academy of Sciences of the United States of America*, 113(37) (2016) 10251-10256.

[31] T.T. Al-Housseiny, P.A. Tsai, H.A. Stone, Control of interfacial instabilities using flow geometry, *Nature Physics*, 8(10) (2012) 747-750.

[32] D. Pihler-Puzović, R. Périllat, M. Russell, A. Juel, M. Heil, Modelling the suppression of viscous fingering in elastic-walled Hele-Shaw cells, *Journal of Fluid Mechanics*, 731 (2013) 162-183.

[33] S.A. Aryana, A.R. Kovscek, Experiments and analysis of drainage displacement processes relevant to carbon dioxide injection, *Physical Review E*, 86(6) (2012) 066310.

[34] F. Furtado, F. Pereira, Crossover from nonlinearity controlled to heterogeneity controlled mixing in two-phase porous media flows, *Computational Geosciences*, 7(2) (2003) 115-135.

[35] D. Silin, T. Patzek, On Barenblatt's model of spontaneous countercurrent imbibition, *Transport in porous media*, 54(3) (2004) 297-322.

[36] J. Sun, Z. Li, F. Furtado, S.A. Aryana, A microfluidic study of transient flow states in permeable media using fluorescent particle image velocimetry, *Capillarity*, 4(4) (2021).

[37] T. Lan, R. Hu, Z. Yang, D.S. Wu, Y.F. Chen, Transitions of fluid invasion patterns in porous media, *Geophysical Research Letters*, 47(20) (2020).

[38] S.C. Cao, S. Dai, J. Jung, Supercritical CO_2 and brine displacement in geological carbon sequestration: Micromodel and pore network simulation

studies, *International Journal of Greenhouse Gas Control*, 44 (2016) 104-114.

[39] R. Lenormand, E. Touboul, C. Zarcone, Numerical models and experiments on immiscible displacements in porous media, *Journal of fluid mechanics*, 189 (1988) 165-187.

[40] C. Zhang, M. Oostrom, T.W. Wietsma, J.W. Grate, M.G. Warner, Influence of viscous and capillary forces on immiscible fluid displacement: Pore-scale experimental study in a water-wet micromodel demonstrating viscous and capillary fingering, *Energy Fuels*, 25(8) (2011) 3493-3505.

[41] F. Guo, S.A. Aryana, An experimental investigation of flow regimes in imbibition and drainage using a microfluidic platform, *Energies*, 12(7) (2019) 1390.

[42] Y.F. Chen, S. Fang, D.S. Wu, R. Hu, Visualizing and quantifying the crossover from capillary fingering to viscous fingering in a rough fracture, *Water Resources Research*, 53(9) (2017) 7756-7772.

[43] I. Salmo, K. Sorbie, A. Skauge, M. Alzaabi, Immiscible Viscous Fingering: Modelling Unstable Water–Oil Displacement Experiments in Porous Media, *Transport in Porous Media*, (2022) 1-32.

[44] L. Mejia, M. Mejia, C. Xie, Y. Du, A. Sultan, K.K. Mohanty, M. Balhoff, Viscous Fingering of Irreducible Water During Favorable Viscosity Two-Phase Displacements, *Advances in Water Resources*, 153 (2021) 103943.

[45] H. Li, Pore-scale study on interfacial force-induced residue mobilization under immiscible ternary fluids flow, *International Journal of Multiphase Flow*, 147 (2022) 103913.

[46] M. Ruith, E. Meiburg, Miscible rectilinear displacements with gravity override. Part 1. Homogeneous porous medium, *Journal of Fluid Mechanics*, 420 (2000) 225-257.

[47] Y. Hu, A. Patmonoaji, C. Zhang, T. Suekane, Experimental study on the displacement patterns and the phase diagram of immiscible fluid displacement

in three-dimensional porous media, *Advances in Water Resources*, 140 (2020) 103584.

[48] S. Yang, G. Kong, Z. Wu, Experimental Study of Gas-Liquid Displacement in a Porous Media Microchip by Digital Image Analysis Method, in: ASME International Mechanical Engineering Congress and Exposition, American Society of Mechanical Engineers, 2021, pp. V010T010A041.

[49] A. Scanziani, Q. Lin, A. Alhosani, M.J. Blunt, B. Bijeljic, Dynamics of fluid displacement in mixed-wet porous media, *Proceedings of the Royal Society A: Mathematical, Physical and Engineering Sciences*, 476(2240) (2020) 20200040.

[50] B. Levaché, D. Bartolo, Revisiting the Saffman-Taylor experiment: imbibition patterns and liquid-entrainment transitions, *Physical review letters*, 113(4) (2014) 044501.

[51] H.S. Rabbani, B. Zhao, R. Juanes, N. Shokri, Pore geometry control of apparent wetting in porous media, *Scientific reports*, 8(1) (2018) 1-8.

[52] F. Guo, S.A. Aryana, Y. Wang, J.F. McLaughlin, K. Coddington, Enhancement of storage capacity of CO_2 in megaporous saline aquifers using nanoparticle-stabilized CO_2 foam, *International Journal of Greenhouse Gas Control*, 87 (2019) 134-141.

[53] Y. Takeuchi, J. Takeuchi, M. Fujihara, Numerical investigation of inertial, viscous, and capillary effects on the drainage process in porous media, *Computers Fluids*, 237 (2022) 105324.

[54] Z. Wang, J.-M. Pereira, E. Sauret, S.A. Aryana, Z. Shi, Y. Gan, A pore-resolved interface tracking algorithm for simulating multiphase flow in arbitrarily structured porous media, *Advances in Water Resources*, 162 (2022) 104152.

[55] B.K. Primkulov, A.A. Pahlavan, X. Fu, B. Zhao, C.W. MacMinn, R. Juanes, Signatures of fluid–fluid displacement in porous media: wettability, patterns and pressures, *Journal of Fluid Mechanics*, 875 (2019).

[56] S.M. Hassanizadeh, W.G. Gray, Toward an improved description of the physics of two-phase flow, *Advances in Water Resources*, 16(1) (1993) 53-67.

[57] G. Barenblatt, T. Patzek, D. Silin, The mathematical model of non-equilibrium effects in water-oil displacement, in: Spe/doe improved oil recovery symposium, OnePetro, 2002.

[58] S.A. Aryana, A.R. Kovscek, Nonequilibrium effects and multiphase flow in porous media, *Transport in porous media*, 97(3) (2013) 373-394.

[59] Y. Wang, S.A. Aryana, F. Furtado, V. Ginting, Analysis of nonequilibrium effects and flow instability in immiscible two-phase flow in porous media, *Advances in Water Resources*, 122 (2018) 291-303.

[60] Y. Wang, S.A. Aryana, M.B. Allen, An extension of Darcy's law incorporating dynamic length scales, *Advances in Water Resources*, 129 (2019) 70-79.

[61] Z. Qin, M. Arshadi, M. Piri, Micro-scale experimental investigations of multiphase flow in oil-wet carbonates. II. Tertiary gas injection and WAG, *Fuel*, 257 (2019) 116012.

[62] Z. Wang, J.-M. Pereira, E. Sauret, Y. Gan, Wettability impacts residual trapping of immiscible fluids during cyclic injection, *Journal of Fluid Mechanics*, 961 (2023) A19.

[63] K. Osei-Bonsu, P. Grassia, N. Shokri, Effects of pore geometry on flowing foam dynamics in 3D-printed porous media, *Transport in Porous Media*, 124(3) (2018) 903-917.

[64] K. Osei-Bonsu, S. Khorsandi, M. Piri, Quantitative analysis of phase topology evolution during three-phase displacements in porous media, *Lab on a Chip*, 20(14) (2020) 2495-2509.

[65] A. Alhosani, A. Selem, S. Foroughi, B. Bijeljic, M.J. Blunt, Steady-State Three-Phase Flow in a Mixed-Wet Porous Medium: A Pore-Scale X-ray Microtomography Study, *Advances in Water Resources*, (2023) 104382.

[66] A. Alhosani, A.M. Selem, Q. Lin, B. Bijeljic, M.J. Blunt, Disconnected Gas Transport in Steady - State Three - Phase Flow, *Water Resources Research*, 57(12) (2021) e2021WR031147.

[67] A. Alhosani, A. Scanziani, Q. Lin, A. Selem, Z. Pan, M.J. Blunt, B. Bijeljic, Three-phase flow displacement dynamics and Haines jumps in a hydrophobic porous medium, *Proceedings of the Royal Society A*, 476(2244) (2020) 20200671.

[68] H. Liu, Q. Kang, C.R. Leonardi, S. Schmieschek, A. Narváez, B.D. Jones, J.R. Williams, A.J. Valocchi, J. Harting, Multiphase lattice Boltzmann simulations for porous media applications, *Computational Geosciences*, 20(4) (2016) 777-805.

[69] S. Li, F. Jiang, B. Wei, J. Hou, H. Liu, Prediction of three-phase relative permeabilities of Berea sandstone using lattice Boltzmann method, *Physics of Fluids*, 33(6) (2021) 063302.

[70] S. Li, Y. Lu, F. Jiang, H. Liu, Lattice Boltzmann simulation of three-phase flows with moving contact lines on curved surfaces, *Physical Review E*, 104(1) (2021) 015310.

[71] M. Oak, Two-and three-phase relative permeability of water-wet Berea sandstone—Appendix to report 89312ART0196, *Rep. F89-P-74, 210-10-13, 89312ART*, (1989).

[72] M. Oak, L. Baker, D. Thomas, Three-phase relative permeability of Berea sandstone, *Journal of Petroleum Technology*, 42(08) (1990) 1054-1061.

[73] D.A. DiCarlo, A. Sahni, M.J. Blunt, Three-phase relative permeability of water-wet, oil-wet, and mixed-wet sandpacks, *Spe Journal*, 5(01) (2000) 82-91.

[74] M.-H. Hui, M.J. Blunt, Effects of wettability on three-phase flow in porous media, *The Journal of Physical Chemistry B*, 104(16) (2000) 3833-3845.

[75] M.J. Blunt, A. Alhosani, Q. Lin, A. Scanziani, B. Bijeljic, Determination of contact angles for three-phase flow in porous media using an energy balance, *Journal of Colloid Interface Science*, 582 (2021) 283-290.

[76] D.H. Fenwick, M.J. Blunt, Three-dimensional modeling of three phase imbibition and drainage, *Advances in water resources*, 21(2) (1998) 121-143.

[77] A. Sahni, J. Burger, M. Blunt, Measurement of three phase relative permeability during gravity drainage using CT, in: SPE/DOE Improved Oil Recovery Symposium, OnePetro, 1998.

[78] K. Singh, M. Jung, M. Brinkmann, R. Seemann, Capillary-dominated fluid displacement in porous media, *Annual Review of Fluid Mechanics*, 51 (2019) 429-449.

[79] A. Alhosani, B. Bijeljic, M.J. Blunt, Pore-scale imaging and analysis of wettability order, trapping and displacement in three-phase flow in porous media with various wettabilities, *Transport in Porous Media*, 140(1) (2021) 59-84.

[80] D. Zivar, S. Kumar, J. Foroozesh, Underground hydrogen storage: A comprehensive review, *International journal of hydrogen energy*, 46(45) (2021) 23436-23462.

[81] M. Lysyy, N. Liu, C.M. Solstad, M.A. Fernø, G. Ersland, Microfluidic hydrogen storage capacity and residual trapping during cyclic injections: Implications for underground storage, *International Journal of Hydrogen Energy*, (2023).

[82] M. Lysyy, T. Føyen, E.B. Johannesen, M. Fernø, G. Ersland, Hydrogen relative permeability hysteresis in underground storage, *Geophysical Research Letters*, 49(17) (2022) e2022GL100364.

[83] C.S. Land, Calculation of imbibition relative permeability for two-and three-phase flow from rock properties, *Society of Petroleum Engineers Journal*, 8(02) (1968) 149-156.

[84] F.M. Carlson, Simulation of relative permeability hysteresis to the nonwetting phase, in: SPE Annual Technical Conference and Exhibition?, SPE, 1981, pp. SPE-10157-MS.

[85] G. Jerauld, General three-phase relative permeability model for Prudhoe Bay, *SPE reservoir Engineering*, 12(04) (1997) 255-263.

[86] Z. Wang, K. Chauhan, J.-M. Pereira, Y. Gan, Disorder characterization of porous media and its effect on fluid displacement, *Physical Review Fluids*, 4(3) (2019) 034305.

[87] R. Hu, T. Lan, G.-J. Wei, Y.-F. Chen, Phase diagram of quasi-static immiscible displacement in disordered porous media, *Journal of Fluid Mechanics*, 875 (2019) 448-475.

[88] H.S. Rabbani, D. Or, Y. Liu, C.-Y. Lai, N.B. Lu, S.S. Datta, H.A. Stone, N. Shokri, Suppressing viscous fingering in structured porous media, *Proceedings of the National Academy of Sciences of the United States of America*, 115(19) (2018) 4833-4838.

[89] N.B. Lu, C.A. Browne, D.B. Amchin, J.K. Nunes, S.S. Datta, Controlling capillary fingering using pore size gradients in disordered media, *Physical Review Fluids*, 4(8) (2019) 084303.

[90] A.L. Herring, E.J. Harper, L. Andersson, A. Sheppard, B.K. Bay, D. Wildenschild, Effect of fluid topology on residual nonwetting phase trapping: Implications for geologic CO2 sequestration, *Advances in Water Resources*, 62 (2013) 47-58.

[91] C. Zhang, M. Oostrom, J.W. Grate, T.W. Wietsma, M.G. Warner, Liquid CO2 displacement of water in a dual-permeability pore network micromodel, *Environmental science technology*, 45(17) (2011) 7581-7588.

[92] S. Suo, Y. Gan, Tuning capillary flow in porous media with hierarchical structures, *Physics of Fluids*, 33(3) (2021) 034107.

[93] J.S. Nijjer, D.R. Hewitt, J.A. Neufeld, Stable and unstable miscible displacements in layered porous media, *Journal of Fluid Mechanics*, 869 (2019) 468-499.

[94] S.S. Datta, D.A. Weitz, Drainage in a model stratified porous medium, *Europhysics Letters*, 101(1) (2013) 14002.

[95] H. Liu, A.J. Valocchi, C. Werth, Q. Kang, M. Oostrom, Pore-scale simulation of liquid CO2 displacement of water using a two-phase lattice Boltzmann model, *Advances in water resources*, 73 (2014) 144-158.

[96] F.G. Wolf, D.N. Siebert, M.N. Carreño, A.T. Lopes, A.M. Zabot, R. Surmas, Dual-porosity micromodels for studying multiphase fluid flow in carbonate rocks, *Lab on a Chip*, (2022).

[97] S. Suo, M. Liu, Y. Gan, Fingering patterns in hierarchical porous media, *Physical Review Fluids*, 5(3) (2020).

[98] M. Musterd, V. Van Steijn, C.R. Kleijn, M.T. Kreutzer, Calculating the volume of elongated bubbles and droplets in microchannels from a top view image, *RSC Advances*, 5(21) (2015) 16042-16049.

[99] G. Kong, H. Mirsandi, K.A. Buist, E. Peters, M.W. Baltussen, J. Kuipers, Oscillation dynamics of a bubble rising in viscous liquid, *Experiments in Fluids*, 60(8) (2019) 1-13.

[100] R. Azadi, J. Wong, D.S. Nobes, Experimental and analytical investigation of meso-scale slug bubble dynamics in a square capillary channel, *Physics of Fluids*, 32(8) (2020) 083304.

[101] H. Wong, C. Radke, S. Morris, The motion of long bubbles in polygonal capillaries. Part 1. Thin films, *Journal of Fluid Mechanics*, 292 (1995) 71-94.

[102] R. Sander, Compilation of Henry's law constants (version 4.0) for water as solvent, *Atmospheric Chemistry and Physics*, 15(8) (2015) 4399-4981.

[103] L.S. Liebovitch, T. Toth, A fast algorithm to determine fractal dimensions by box counting, *physics Letters A*, 141(8-9) (1989) 386-390.

[104] D. Wildenschild, A.P. Sheppard, X-ray imaging and analysis techniques for quantifying pore-scale structure and processes in subsurface porous medium systems, *Advances in Water resources*, 51 (2013) 217-246.

[105] S.J.T.i.p.m. Whitaker, Flow in porous media I: A theoretical derivation of Darcy's law, 1 (1986) 3-25.

[106] J. Yue, L. Luo, Y. Gonthier, G. Chen, Q. Yuan, An experimental study of air–water Taylor flow and mass transfer inside square microchannels, *Chemical Engineering Science*, 64(16) (2009) 3697-3708.

[107] J. Yue, G. Chen, Q. Yuan, L.a. Luo, H. Le Gall, Mass transfer in gas-liquid flow in microchannels, *Journal of Chemical Industry Engineering-China*, 57(6) (2006) 1296.

[108] C. Li, C. Zhu, Y. Ma, D. Liu, X. Gao, Experimental study on volumetric mass transfer coefficient of CO2 absorption into MEA aqueous solution in a rectangular microchannel reactor, *International Journal of Heat and Mass Transfer*, 78 (2014) 1055-1059.

[109] H. Niu, L. Pan, H. Su, S. Wang, Effects of design and operating parameters on CO2 absorption in microchannel contactors, *Industrial & Engineering Chemistry Research*, 48(18) (2009) 8629-8634.

[110] G. Bercic, A. Pintar, The role of gas bubbles and liquid slug lengths on mass transport in the Taylor flow through capillaries, *Chemical Engineering Science*, 52(21-22) (1997) 3709-3719.

[111] C. Yao, Z. Dong, Y. Zhao, G. Chen, Gas-liquid flow and mass transfer in a microchannel under elevated pressures, *Chemical Engineering Science*, 123 (2015) 137-145.

[112] J. Van Baten, R. Krishna, CFD simulations of mass transfer from Taylor bubbles rising in circular capillaries, *Chemical Engineering Science*, 59(12) (2004) 2535-2545.

[113] T. Sherwood, R. Pigford, C. Wilke, Mass Transfer McGraw-Hill, *New York*, (1975).

[114] X. Zhu, L. Chen, S. Wang, Q. Feng, W. Tao, Pore-scale study of three-phase displacement in porous media, *Physics of Fluids*, (2022).

[115] M.T. Van Genuchten, A closed ‐ form equation for predicting the hydraulic conductivity of unsaturated soils, *Soil science society of America journal*, 44(5) (1980) 892-898.

[116] Y. Mualem, A new model for predicting the hydraulic conductivity of unsaturated porous media, *Water resources research*, 12(3) (1976) 513-522.

[117] H. Li, T. Zhang, Imaging and characterizing fluid invasion in micro-3D printed porous devices with variable surface wettability, *Soft Matter*, 15(35) (2019) 6978-6987.

[118] E.J. Spiteri, R. Juanes, M.J. Blunt, F.M. Orr, A new model of trapping and relative permeability hysteresis for all wettability characteristics, *Spe Journal*, 13(03) (2008) 277-288.

[119] H. Ahn, S.-O. Kim, M. Lee, S. Wang, Migration and residual trapping of immiscible fluids during cyclic injection: pore-scale observation and quantitative analysis, *Geofluids*, 2020(1) (2020) 4569208.

[120] G. Mason, N.R. Morrow, Effect of contact angle on capillary displacement curvatures in pore throats formed by spheres, *Journal of colloid interface science*, 168(1) (1994) 130-141.

[121] C.A. Reynolds, H. Menke, M. Andrew, M.J. Blunt, S. Krevor, Dynamic fluid connectivity during steady-state multiphase flow in a sandstone, *Proceedings of the National Academy of Sciences of the United States of America*, 114(31) (2017) 8187-8192.

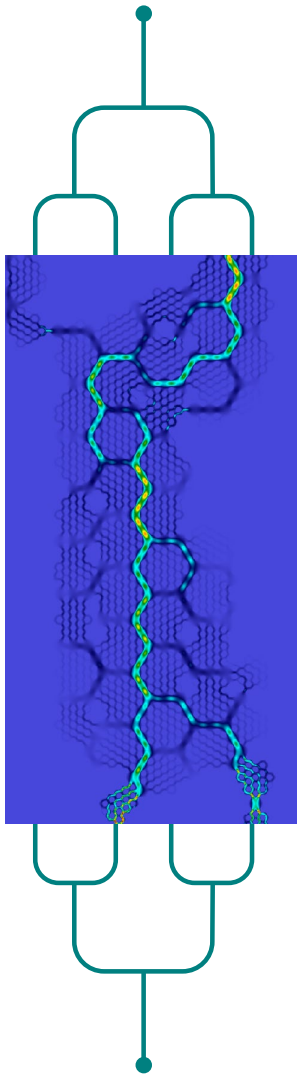

Printed by Media-Tryck, Lund 2024 NORDIC SWAN ECOLABEL 3041 0903

Division of Heat Transfer
Department of Energy Sciences
Faculty of Engineering
Lund University
ISBN 978-91-8104-096-8
ISSN 0282-1990
ISRN LUTMDN/TMHP-24/1176